Micropropulsion Systems for Precision Controlled Space Flight

Larsen, Jack

Publication date:
2013

Document Version
Publisher's PDF, also known as Version of record

DTU Space
National Space Institute

Technical University
of Denmark

Micropropulsion Systems for Precision Controlled Space Flight

by

Jack Larsen

A thesis submitted in partial fulfillment for the degree of Philosophical Doctor

at

DTU Space
National Space Institute

May 31st 2013

"Keep things as simple as possible, but no simpler"

Albert Einstein

TECHNICAL UNIVERSITY OF DENMARK

Abstract

DTU Space
National Space Institute

Philosophical Doctor

by Jack Larsen

Space science is subject to a constantly increasing demand for larger coherence lengths or apertures of the space observation systems, which in turn translates into a demand for increased dimensions and subsequently cost and complexity of the systems. When this increasing demand reaches the pratical limitations of increasing the physical dimensions of the spacecrafts, the observation platforms will have to be distributed on more spacecrafts flying in very accurate formations. Consequently, the observation platform becomes much more sensitive to disturbances from the space environment. This project is thus concentrating on developing a method by which an entire, efficient, control system compensating for the disturbances from the space environment and thereby enabling precision formation flight can be realized.

The space environment is initially studied and the knowledge gained is used to deduce the requirements for a propulsion system consituting the actuator part of a control system eliminating the disturbances from the space environment. Due to the minute magnitudes of the forces to be delivered, this type of propulsion has been denoted *Micropropulsion*. Initially a theoretical study of the disturbance forces and their influence on a precision controlled spacecraft, is used to deduce the requirements for a micropropulsion system compensating for these. Following this an LTCC based resistojet microthruster is developed and fabricated, utilizing water as fuel. Towards the end of the project, a proof of concept has been conducted, by proving the principle is working in atmospheric conditions. The solution to evolve the concept into being applicable for space applications is then given.

DANMARK TEKNISKE UNIVERSITET

Resume

DTU Space
Institut for Rumforskning og -teknologi

Ph.D. Afhandling

af Jack Larsen

Rumforskningens betydning som forskningsområde og i stigende grad som en kilde til uundværlig information i hverdagen, eksempelvis vejrinformation og navigation er iøjnefaldende. Rumteknologi og metoder kan dog som ethvert andet teknologisk område stadig udvikles og forbedres til gavn for samfundet. Præcis formationsflyvning med rumfartøjer vil i den nærmeste fremtid få stor betydning for rumbaseret forskning, hvilket nødvendiggør udvikling af måle og styresystemer med hidtil uset nøjagtighed. Dette begrundes med at når rumfartøjer skal arbejde sammen om at undersøge det samme fænomen, bliver de mere følsomme overfor forstyrrelser fra miljøet i rummet. Disse forstyrrelser har deres oprindelse både fra solen, jordens atmosfære og den forskel i tyngdekraft der virker på de forskellige rumfartøjer i formationen.

I dette projekt er derfor udviklet en ny metode til fremstilling af styreraketter, som baserer sig på keramikteknologi og mikromekanik. Grundet de meget små kræfter der skal kompenseres for, er formålet med projektet at minimere reaktionskraften fra styreraketterne så rumfartøjerne kan styres så præcist som muligt. Systemet der er udviklet hører derfor ind under en kategori af fremdriftssystemer kaldet *Micropropulsion*. Projektet har resulteret i fremstillingen flere prototyper, og karakteriseringen af disse har vist at det implementerede princip opfylder kravende og tilbyder en simpel pålidelig metode til fremstilling af præcise styreraketter til satellitter.

Acknowledgements

Many committed people have contributed to the accomplishments of this project. Besides my supervisor John Leif Jørgensen I would like to thank the following people for this commitment and for helping me carrying out this thesis:

Henrik Bruss from DTU Nanotech for the constructive brainstorming on implementing capillary pumping

Thomas Jensen from DTU Electrical Engineering for the close collaboration on the introduction of LTCC

Maciej Skolimowski from DTU Nanotech for the assistance on micro milling

Jan Patrick Scholer from DTU Chemistry for preparing the glass wire for our test setup, and most of the glass frit parts used for the prototyping

Claus Kjærgaard for letting us use the thickfilm lab at DTU Electro, and for the assistance on designing thickfilm circuits

Eric Jensen for the assistance on SEM imaging

Michael Lotz from Heraeus Precious Metals GmbH & Co. KG, Thick Film Materials Division, for providing us with free samples of LTCC sheets

Fellow Students from the PhD office for keeping a great atmosphere in the working environment

My Wife for supporting me thoughout this PhD

Contents

List of Figures

List of Tables

Abbreviations

MEMS	**M**icro **E**lectro **M**echanical **S**ystem
MICROSCOPE	**M**icro-**S**atellite à traînée **C**ompensée pour l'**O**servation du **P**rinpe d'**E**quivalence
CNES	**C**entre **N**ational d'**E**tudes **S**patiales
AACS	**A**ttitude and **A**cceleration **C**ontrol **S**ubsystem
Micro **ASC**	Micro **A**dvanced **S**tellar **C**ompass
MCA	**A**ccelerations **C**ontrol **M**ode
DCM	**D**irection **C**osine **M**atrix
AD	**A**tmospheric **D**rag
SRP	**S**olar **R**adiation **P**ressure
FEEP	**F**ield **E**mission **E**lectric **P**ropulsion
LMIS	**L**iquid **M**etal **I**on **S**ource
PCB	**P**rinted **C**ircuit **B**oard
LTCC	**L**ow **T**emperature **C**o-fired **C**eramic
HTCC	**H**igh **T**emperature **C**o-fired **C**eramic
LEO	**L**ow **E**arth **O**rbit
MEO	**M**edium height **E**arth **O**rbit
HEO	**H**ighly **E**lliptical **O**rbit
GEO	**G**eostationary **E**arth **O**rbit
SEM	**S**canning **E**lectron **M**icroscopy
CNC	**C**omputer **N**umerically **C**ontrolled
CAD	**C**omputer **A**ided **D**rawing
CAM	**C**omputer **A**ided **M**achining
MCM	**M**ulti **C**hip **M**odule
MMIC	**M**onolithic **M**icrowave **I**ntegrated **C**ircuit
SMD	**S**urface **M**ount **D**evice
CCD	**C**harge **C**oupled **D**evice
PMMA	**P**oly**M**ethyl**M**eth**A**crylate

Chapter 1

Introduction

1.1 Propulsion

Traveling the world has been desired by man as long as we can look back in time. And never have we been satisfied with the speed at which we can travel from one place to another unaided. Consequently, we have always strived to develop improved methods for traveling, such as riding, sailing, driving and flying. Common for all these sorts of transportation is the need of propulsion, which is the term we use to denote the discipline of actively driving something forward. The term propulsion is derived from the two Latin words: *pro* and *pellere*, meaning forward and drive respectively.

As the Earth is becoming more and more thoroughly explored by man, it cannot fulfill our curiosity any more, and consequently we have started to look into outer space. This has only put even more extreme demands on our technical capabilities regarding propulsion - so extensive that the term "Rocket Science" has become synonymous with something very difficult. The massive attention on the space race in the final part of the 20'th century, where the two superpowers of the world kept failing over and over again, made people aware of the great challenges space propulsion is facing. In this respect, perhaps the most crucial fact to be aware of, is, that in space there is nothing to stick to. That means, unlike on Earth where the tires of a vehicle can stick on the ground and the airplanes can stick on the air in order to pull them self forward, a spacecraft has to bring fuel, both to produce the kinetic energy, but also to have a medium to push on.

The research on propulsion is often focused on increasing the thrust and the fuel efficiency, in order to be able to bring larger and larger vehicles into space

and to reach more and more distant destinations. However, the research in this project, is focused on minimizing the thrust, in order to increase the precision with which the orientation, position and acceleration can be controlled. Consequently, we use the term *Micropropulsion* to denote the branch of propulsion we are dealing with in this project.

1.2 Motivation - Drag Free Flight - Formation Flight

The field of *Micropropulsion* is presently being assigned more and more attention in the space industry around the world. This is due to the ever increasing demand for larger coherence lengths or apertures of the space observation systems, which in turn translates into a demand for increased dimensions and subsequently cost and complexity of the systems. When this increasing demand reaches the practical limitations of increasing the physical dimensions of the spacecrafts, the observation platforms will have to be distributed on more spacecrafts flying in very accurate formations. Consequently, the observation platform becomes much more sensitive to disturbances from the space environment, due to the lack of the mechanical stiffness which is present when all parts are included on one spacecraft. For a low earth orbit the primary disturbance will be due to the atmospheric drag, but also the solar radiation pressure is a significant factor when disturbances in the micro-newton regime are to be considered.

1.2.1 Swarm

To give an impression of the possibilities and the great long term perspective precision controlled space flight offers, we will look at a number of space missions utilizing formation flight and/or drag free flight. Since the launch of the danish satellite Ørsted, Denmark has been leading in the field of magnetometry. Besides the Ørsted mission the DTU magnetometer has flown both on a Swedish mission called Astrid-2 and on the german CHAMP mission. The magnetometer measures both the scalar field and its direction and is the most accurate and reliable in the world today. Now as a follow up on the CHAMP mission, ESA has scheduled the Swarm satellites to be launched in 2013. The objective of the Swarm mission is to provide the best ever survey of the geomagnetic field and its temporal evolution. It consists of 3 satellites, where 2 will fly in formation side by side at a relatively

low altitude of 450 km and the third will fly higher at 530 km. Thus, Swarm in one of the future missions which will benefit from having satellites flying formation.

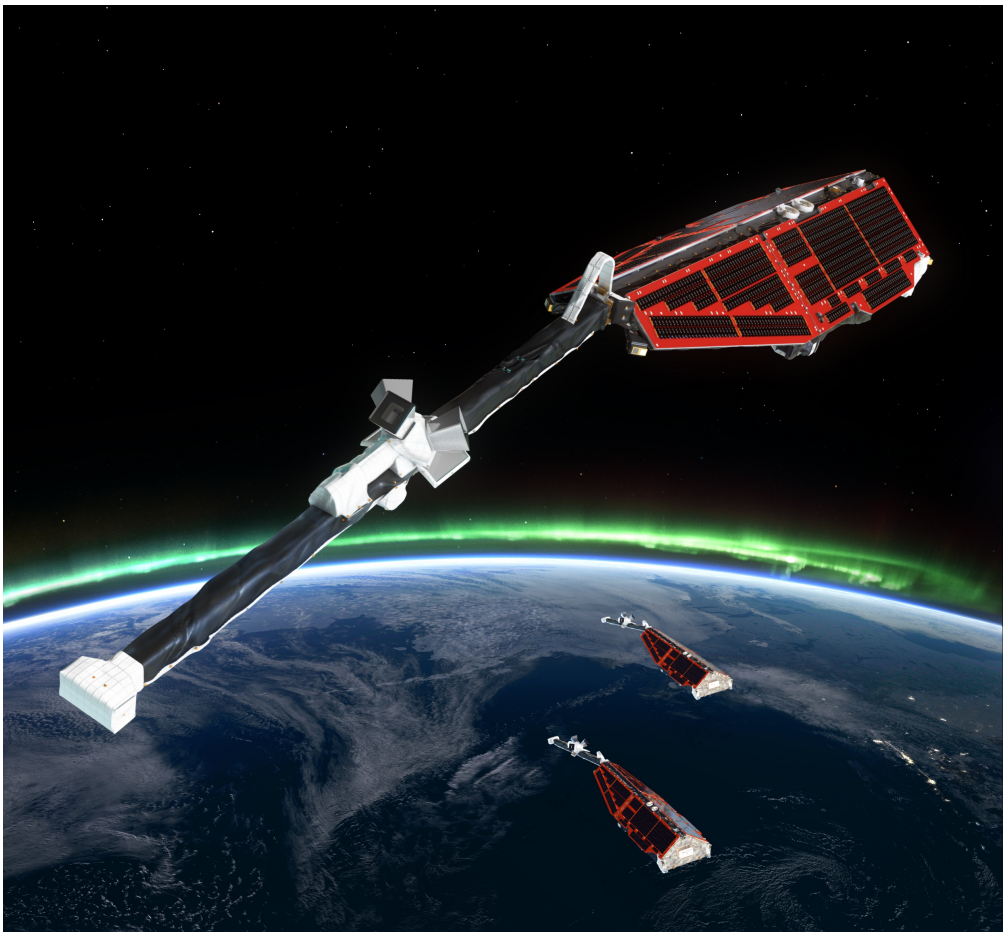

Figure 1.1: The Swarm constellation consists of 3 satellites with long booms for bringing the magnetometers on a fair distance to the disturbing spacecrafts. In the middle of the boom is placed the optical bench with star trackers and a vector magnetometer. And on the tip of the booms are the scalar magnetometers placed. Picture is from [3].

The Swarm mission is designed to measure the magnetic signals that stem from Earth's core, mantle, crust, oceans, ionosphere and magnetosphere. This will lead to better understanding of the processes that drive Earth's dynamo, which currently appears to be weakening. By studying the complexities of Earth's protective shield, Swarm will provide a clear insight into processes occurring inside the planet. Along with measurements of conditions in the upper atmosphere, a better knowledge of the near-Earth environment and the Sun's influence on the planet can be realized [1].

The Swarm mission was proposed to ESA by DTU Space. Hence, DTU Space is highly involved in the mission, as the department is delivering both the vector magnetometers and the stellar compasses for the mission. DTU is also leading

the data processing, preparing magnetic field models, models of the electrical conductivity and products related to space weather [2].

1.2.2 GRACE - Gravity Recovery and Climate Experiment

The two satellites constituting the formation flying of the NASA GRACE mission, conducts ultra precise measurements of the gravity field of the Earth. The GRACE satellites always know where they are with respect to each other. And that makes them capable of measuring the gravity field of Earth. The inter-satellite distance is determined by radar, where it is possible to detect changes in the distance of 1 micrometer, partly because of the high accuray of the pointing of the radar, made possible by the star trackers delivered by DTU Space. The satellites are flying with a distance of 200 km, and when the satellite in front goes "down hill", the chasing satellite will fall behind a little bit. The chasing satellite then catches up shortly after, and thereby the radar system can detect small anomalies in the gravity field with an accuracy 100 times greater than hitherto. These measurements can tell what natural phenomena like the El Nino means to the big water flows, and scientists are striving to be capable of predicting earthquakes by looking at sudden changes in the gravity field of Earth [4].

However, the GRACE mission suffers from a drawback, due to its lack of a micropropulsion system. This drawback comes from the fact that when the spacecrafts are spending their fuel unevenly, due to the differential disturbance forcing on the two, their ballistic coefficients (the measure of a body's ability to overcome air drag) becomes different and consequently one of them will loose altitude faster than the other if nothing is done to prevent it. On GRACE this is prevented by wasting some of the fuel on the spacecraft which is spending its fuel more slowly. This of course shortens the lifetime of the mission, which it very unfortunate.

1.2.3 Prisma, PROBA 3 and the Visual Based System

The Visual Based Sensor (VBS) is an instrument developed by DTU Space on the basis of the stellar compass also developed at DTU Space. The purpose of the VBS is to visually determine the relative position and attitude between spacecrafts flying in close formation or vehicles performing rendezvous and docking. The VBS is currently flying on the Swedish technology demonstration mission Prisma,

which consists of two spacecrafts - a target satellite without control system and a main satellite with full control on all six degrees of freedom. On this mission the VBS has shown an extremely high position accuracy: at a 5 meter distance - 0.1 mm laterally and 0.5 mm on the distance. Hence, the VBS together with a micropropulsion system can comprise a supreme control system for close formation flight.

The working principle of the VBS is somewhat similar to that of a star tracker. A CHU (Camera Head Unit) is acquiring images of the target satellite, which is equipped with a number of LED's for which the placement is calibrated with the VBS. On the basis of the constellation of the LED's in the acquired image, the attitude and distance to the target is then computed in a DPU (Data Processing Unit), similar to the DPU of a stellar compass. In case that the target is so distant that the VBS is unable to distinguish the LED's or the target is simply a lighting dot, it can also go into a far range mode where the target is tracked as it was a single star. At present, non-cooperative target tracking is also being investigated in our department, where the target could be any space vehicle only illuminated by the sun or planetary albedo.

The next mission for demonstrating formation flying - where the VBS is to be utilized - is the third mission in the PROBA (Project for On-Board Autonomy) series. As part of the formation flying demonstration on the PROBA 3 mission, the objective is to observe the corona of the Sun. Consequently, the formation will consist of 2 small spacecrafts. One spacecraft carrying the main optical bench and associated detectors, electronics, etc., and another spacecraft carrying an occulter. The intention is thus to place the spacecrafts in a formation where they - together with the Sun - are aligned along a target line within 1 millimeter, when flying 150 meters apart. Accordingly the occulter spacecraft should fly in front of the Sun, blocking most of the sunlight, making only the corona visible to the spacecraft carrying the coronagraph. Thus flying the PROBA 3 mission, besides validating the technology for formation flying, questions like:

- What is the fine scale nature of the solar corona?
- What processes contribute to the heating of the corona and what is the role of waves?
- How and where does the solar wind originate?
- What processes contribute to the acceleration of the slow and fast solar winds?

- What is the nature of the structures that form the coronal mass ejections (CMEs)?
- What is the connection between CMEs and dynamic processes on the solar surface?
- How do CMEs erupt and accelerate in the low corona?
- Where and how can a CME drive a shock in the low corona?

are to be answered [5].

1.2.4 MICROSCOPE - Micro Satellite à traînée Compensée pour l'Oservation du Prinpe d'Equivalence

Precision controlled space flight is primarily relevant for formation flying missions operating with two or more spacecrafts. However, some scientific space borne experiments do require drag free flight, despite they are being performed on a single spacecraft. With drag free flight is understood a flight mode where all disturbances - meaning all forces except for the gravitational - are balanced out with very high precision by the propulsion system.

One of these space borne experiments, is the one to be performed on the fourth microsatellite based on the MYRIADE product line utilized by CNES, namely the MICROSCOPE mission, which has the objective of verifying the equivalence principle. Myriade is a new concept of modular microsatellites having a mass less than 200 kg and thereby is offering quick, low-cost access to space. While such satellites serve chiefly for scientific missions, they can also be used for technology demonstrations and future services. CNES decided to start development of Myriade in 1998, to complement its Proteus line of minisatellites. Technological advances, especially miniaturization of electronics, make it possible to pack a lot of performance into a small satellite, and Myriade makes extensive use of commercial-off-the-shelf components [6].

More specifically the objective of the MICROSCOPE mission is to verify the equivalence principle with an accuracy of 10^{-15} - two orders of magnitude better than present measurements has confirmed. The equivalence principle has been verified using numerous methods (torsion balances, laser ranging etc.), but the noise and vibrations inherent in any Earth-bound test environment limit the accuracy to less than 10^{-13}. New physics theories such as string theory or super

gravity propose a possible EP violation under 10^{-13}, which shows the significance of the mission. By exploiting Earth as the gravitational source, the in orbit motion of two masses falling in Earth's gravitational field - and composed of two different materials - is controlled identically. Hence, the experiment takes advantage of the soft environment on a drag free satellite, where non gravitational forces are compensated, less fluctuations of the gravity gradient are present and no human activity can cause any perturbations. Furthermore very long periods of observation of the free fall mass motions in very steady conditions leads to integration of the measurements being collected over days to the benefit of the rejection of stochastic disturbances.

The MICROSCOPE mission will also have spinning flight modes, where the rotation of the observational frame with respect to gravitational field helps in the discrimination of the eventual EP violation signal. In this respect several rotation frequencies and phases are to be considered. The primary payload on the spacecraft is two quasi identical differential accelerometers. Each accelerometer includes two cylindrical and concentric test masses. The masses are made of the same material for the first one, which is dedicated to assess the accuracy of the EP experimentation.

The attitude as well as the atmospheric and the thermal drag of the satellite are actively controlled in such a way that the satellite follows the two test masses in their gravitational motion, thanks to the specific drag compensation and attitude control system.

1.2.5 LISA - Laser Interferometer Space Antenna

The LISA mission is a proposed space mission flying 3 spacecrafts with a distance of 5 million km, with the purpose of detecting and accurately measure gravitational waves from astronomical sources. LISA detects gravitational-wave induced strains in space-time by measuring changes of the separation between fiducial masses in three spacecrafts 5 million kilometers apart. Without micropropulsion a mission like this is not realizable. The mission started out as a joint effort between NASA and ESA due to the huge cost of the mission, but NASA has announced that it would most likely not be able to participate due to lack of funding.

For LISA to become realizable many new technologies must be developed and consequently a technology demonstration mission called LISA Pathfinder is scheduled for launch in 2014. The LISA Pathfinder will demonstrate the near-perfect free-fall of a test mass located inside the body of the spacecraft by limiting the

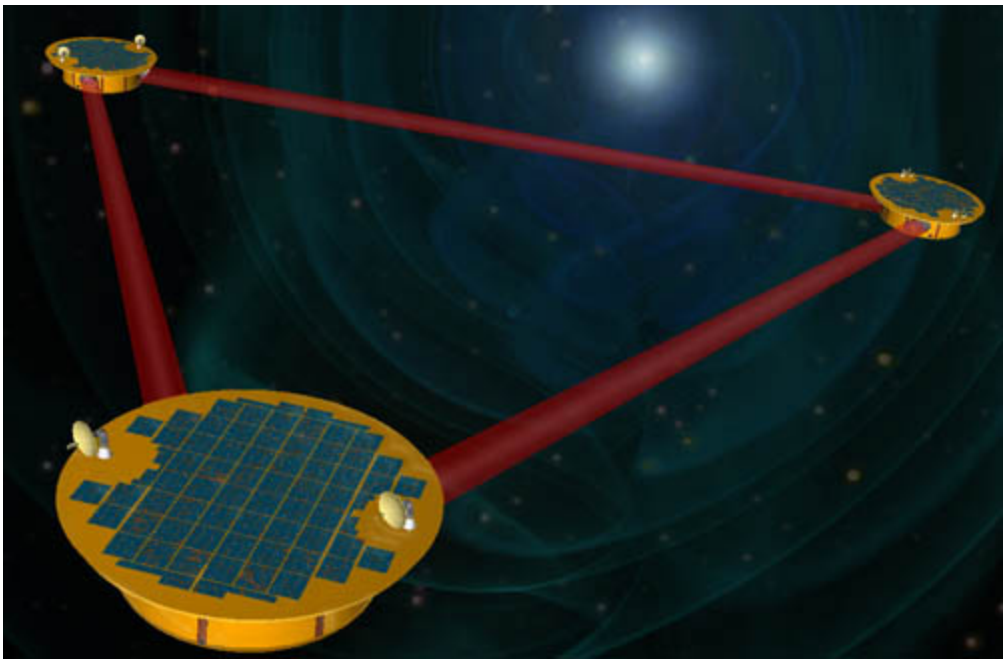

Figure 1.2: The LISA mission is a proposed space mission flying 3 spacecrafts with a distance of 5 million km, placed in stable Lagrange points in the solar system. LISA shall investigate scientific phenomena like the formation and growth of massive black holes and their co-evolving host galaxies.

spectral density of accelerations of the test mass, similarly to the MICROSCOPE mission. The basic idea is that of squeezing one LISA arm from 5 million km to a few centimeters and in placing it on a single spacecraft. Hence, the key elements are two nominally free flying test masses and a laser interferometer with the purpose of reading the distance between them. The two test masses are surrounded by their position sensing electrodes. This position sensing provides the information to the drag-free control loop. The primary goal of the LISA Pathfinder test is to verify that a test-mass can be put in pure gravitational free-fall within one order of magnitude from the requirement for LISA [7].

As part of the technology demonstration, LISA Pathfinder is thus flying different micropropulsion systems, including a FEEP (Field Emission Electric Propulsion) based system accelerating ions to produce thrust and a resistojet system combining a cold gas system with microvalves with a heater system to increase thruster performance. These principles are discussed in greater detail in Chapter 4.

Gravitational wave observations will enable studies of: the formation and growth of massive black holes and their co-evolving host galaxies; structure formation; stellar populations and dynamics in galactic nuclei; compact stars; the structure of our Galaxy; General Relativity in extreme conditions; cosmology;

and searches for new physics. Information from LISA sources will provide unique insight into extraordinary astrophysical objects. Combined with electromagnetic observations, these insights will advance the broader scientific understanding [8].

1.3 Space Environment

1.3.1 Differential Gravity

Obviously the predominant force to consider within space flight is the gravitational attraction from Earth. First of all it is the force that keeps a satellites in a nearly perfect keplerian (elliptical) orbit with Earth in one of the foci, which is why formation flying satellites could not fly side by side without active control, since their orbit planes would otherwise cross each other and provide a risk of collission. On a mission like the MICROSCOPE, the differential gravity / gravity gradient also plays a role, since the satellite flies 2 high precision accelerometers, with test masses distant from the center of mass. Secondly the gravitational force is the cause of orbital disturbances, primarily due to the equatorial bulge of the Earth causing its field to differ from that of a perfect sphere. This constantly alters the argument of periapsis of the orbit - known as apsidal precession - and is the cause of the regression of the lines nodes, described in Chapter 3.

1.3.2 Atmospheric Drag

By definition, space is reached above an altitude of 100 km. When talking about the environment in space, people tend to think that its all emptiness and consequently they are often surprised to hear that there are disturbances to worry about. But especially for spacecrafts put into orbits close to the earth, the drag due to the atmosphere of the earth can no more be neglected and becomes the predominant disturbance below 600 km of altitude.

The atmospheric drag changes with the density of the atmosphere, but is also dependent on the size and shape of the spacecraft. An aerodynamic shape can actually reduce atmospheric drag by a factor of 20, compared to a cubic shape, and consequently very low Earth orbiting satellites can gain a significant benefit by optimizing the aerodynamics. A satellite like this is the GOCE satellite, which is mapping the gravity field of Earth, from an altitude of only 260 km. This octagonal, 1100-kg satellite with a cross-sectional area of only 1 m^2 is configured to keep

Figure 1.3: The GOCE satellite is an example of a mission where it is crucial that the atmospheric drag is accounted for. This is done by providing the spacecraft with an aerodynamic shape, including wings for stabilization, and a xenon ion engine for compensation of the atmospheric drag [11].

aerodynamic drag and torque to an absolute minimum. GOCE is symmetrical about its flight direction and two winglets provide additional aerodynamic stability. While the sleek aerodynamic design helps GOCE cut through what remains of the atmosphere at its exceptionally low altitude, an electric ion thruster at the back continuously generates a small thrust to compensate for any drag the satellite experiences [10]. Finally the atmospheric drag depends overwhelmingly on the speed of the spacecraft, as it increases with the square of the speed. The speed is determined from its orbital elements and current position within the orbit and the magnitude of the atmospheric drag is thus very dependent on the actual altitude of the spacecraft, not only because of the varying density of the atmosphere.

1.3.3 Solar Radiation Pressure and Solar Wind

In addition to the atmospheric drag, the Sun is also causing a disturbance on space vehicles. This disturbance is simply due to the radiation of the Sun causing a pressure called the SRP (Solar Radiation Pressure), which is present since the photons irradiated from the sun have momentum although they have no mass. For orbits around 600 - 700 km the SRP is normally in the same order of magnitude as the atmospheric drag. The SRP on the exposed surfaces of the spacecraft is

dependent on the incident angle of the radiation, the reflective characteristics determining the fraction of absorbed and reflected radiation and the distance to the Sun. In parallel to the solar radiation the sun emits solar wind which mainly consists of ionized nuclei and electrons radiated from the sun [14]. The magnitudes of the pressure produced by the solar radiation and the solar wind are proportional to momentum flux of the radiation. According to [16], the solar radiation momentum flux is about a factor of 100 to 1000 times greater than that of the solar wind. Consequently, the solar wind is neglected in this thesis.

1.3.4 Environmental Impact on Instrumentation

Outside the protecting atmosphere of the earth the environment differs significantly from that within. This difference includes atmospheric pressure, temperature, radiation and gravity. Gravity is not important for the majority of instruments, but influences the time rate and must be accounted for in GPS satellites. For solar cells and electronic equipment the radiation becomes critical when the spacecraft is located in the radiation belts for a longer period. The ionizing radiation present in orbits around the earth is mainly due to trapped electrons and protons within the Van Allen belts. But significant fluxes of heavy ions such as helium, nitrogen and oxygen may also be present. Fluxes of electrons and protons are degrading electronic equipment and solar cells. Although their masses are very small, especially for electrons, they make displacements in the crystal lattice of the silicon due to their high energy [26]. Shielding of components vulnerable to radiation is therefore necessary in some cases.

In LEO (Low Earth Orbit applications, below 800 km), components are tested in the temperature range from -40°C to +85°C. But traveling to deep space (moon and beyond) the temperature can become significantly higher or lower. In an orbit the temperature furthermore varies significantly as the satellites from time to time gets into eclipse of the planet. Consequently, where different materials with different thermal expansion coefficients are bonded together on a device, large stresses are present in the bonding interface, with the danger of these bondings being broken.

The lack of atmospheric pressure is a problem to materials with a high vapor pressure. In space these materials will slowly sublimate or outgas. In fact all materials outgasses although most are doing it very slowly. The low pressure in space also demands that no air bobbles are encapsulated while packaging a device. This rules out many kinds of glues and epoxies since air bobbles often

Mission	Trajectory type
Communications	Geostationary for low latitudes, Molniya and Tundra for high latitudes (mainly Russian), Constellation of polar LEO satellites for global coverage
Earth resources	Polar LEO for global coverage
Weather	Polar LEO or geostationary
Navigation	Inclined MEO for global coverage
Astronomy	LEO, HEO, GEO and 'orbits' around Lagrange points
Space environment	Various, including sounding rockets HEO
Military	Polar LEO for global coverage, but various
Technology demonstration	Various

Table 1.1: Payload/mission types. GEO: Geostationary Earth Orbit; HEO: Highly Elliptical Orbit; LEO: Low Earth Orbit; MEO: Medium height Earth Orbit [26].

are accumulated during the curing process. Hermetic encapsulations are avoided if possible, since a high pressure difference between the inside and outside of the package, can cause the bonding to break when the air is trying to escape.

The conditions in space varies significantly depending on the type of orbit, and the type of orbit is dependent on the payload or mission type. In Table 1.1 the orbit types used for different types of missions are seen. LEO's are dominated by proton radiation whereas high altitude orbits, including GEO's, are dominated by electron radiation. At the altitude of a GEO (circular equatorial orbit at 35786 km) the annual electron dose is approx. 2×10^4 rads [26], i.e. for a mission with duration of one year in GEO the components should not fail before reaching 20 krads, assuming no form of radiation shielding is present. For an orbit with a high inclination (the angle to the equatorial plane) at the same altitude, the dose will be lower due to the shape of the radiation belts.

Chapter 2

Problem Formulation and Outline

2.1 Problem Statement

Common for the present formation flying systems are, that the satellite formation knowledge is used, but only to a very limited extent, is the actual formation flight controlled. This is due to the fact that although space is being dominated by gravitational forces, the disturbance forces discussed in Chapter 1, affects the formation, in an often chaotic manner. These other forces disturb any attempt on precision formation flight, unless both controlled attitude behavior and actuation delivering reaction forces, are canceling out the disturbances at a detailed level.

Due to the nature of these disturbances, their impact is poorly understood, especially because observation of the often minute disturbances is difficult. Hence, no efficient precision controlled reaction force actuation systems exist, and consequently, high accuracy formation flying is presently only under study worldwide. These studies are carried out because of the vast potential, high accuracy formation flight systems offer, in terms of increased aperture and correlation lengths, enabling entire new scientific observations as well as increased science return from existing observation technologies.

The proposed study will consequently start out by seeking to understand the nature of the disturbance forces, and their influence on a precision formation flight, focusing on Earth orbiting systems. By proper modeling, the target is to establish an operational model for the disturbance forcing of a precision formation flying system, through which the requirements for sensor and reaction systems may be derived.

Once the nature of disturbances on the formation flying system is understood, applicable sensor techniques capable of measuring either the primary or secondary effects on the spacecraft system will be studied, such as to be able to design an optimal controller of the actuation system.

The main focus, when knowing the disturbances and how to measure these, will be appointed the efficiency of actuation systems canceling out or limiting the differential force on the formation flying system. Because of the general minute size of the disturbance forces, the actuator thrust levels are in the micro-N regime, which has given rise to the name for this kind of propulsion: *Micropropulsion*. At present several physical principles is suggested for micropropulsion, ranging from chemical, over thermo dynamical to electro dynamic. The study will aim at ranking these technologies, and to implement a model system, based on a promising candidate.

Hence, the goal of the study is, to develop a method by which an entire, efficient, control system enabling precision formation flight can be realized.

A highly relevant and present mission to perform precision controlled space flight is the French CNES mission MICROSCOPE, which is described earlier in Chapter 1. This mission will to a large extent be used as a mission template for the study, partly because of the realism thus provided to the study, partly because results from the study through DTU's engagement in this mission will be directly used for a real spacecraft mission.

Working with experimental projects a weighting of the different sub assignments is required. This weighting must balance the importance of the educational content to the practicable outcome of the project. Recalling the primary purpose of this project: to find a method and realize a system facilitating precision controlled flight, the study is divided into the following sub assignments:

1. Preliminary investigation on the requirements to and the purpose of the device
2. Focusing on the MICROSCOPE mission, investigating the nature of the disturbances the device should be capable of eliminating
3. Investigation of sensor techniques, propulsion principles and fabrication technologies to be implemented
4. Theoretical considerations and calculations on dimensioning etc.
5. Design and integration of the chosen principle with the chosen technologies

6. Design and implementation of an applicable test setup

7. Verification of the performance of the fabricated devices

2.2 Report Overview

An overview of the following thesis is given in this section. The path from initial considerations on requirements and purpose of the device to the characterization of the final prototype, is divided into the following 6 chapters:

Chapter 3 Disturbance Forces: The physics and the mathematical tools to be utilized for modeling disturbance forces on an Earth orbiting spacecraft is developed and presented. These include orbital elements, coordinate transformation and orbit perturbations. Atmospheric drag and solar radiation pressure is studied in detail, and deduced for the MICROSCOPE mission.

Chapter 4 Sensor Techniques and Propulsion Principles: Different proposed principles of sensor techniques and propulsion are presented here, and their advantages and drawbacks are discussed with relation to their capability of being implemented with a micropropulsion control system. These sensor techniques include visual based systems, gps, accelerometers and radio frequency sensors. The principles of propulsion include chemical propulsion, gold gas propulsion, resistojets and field emission electric propulsion.

Chapter 5 LTCC Based Resistojet: In this chapter the designs developed and fabricated for testing are presented, and the results of the prototyping conducted using LTCC technology are documented. Initially the necessary theory for dimensioning the thrusters is presented. The primary fabrication technique utilized extensively in this project, is the micromilling technique presented in this chapter. In addition the realization of different types of heating elements is included, where thickfilm technology is implemented.

Chapter 6 Characterization: In order to finalize the experimental work performed, an applicable test setup is build and the performance of the prototypes in atmospheric conditions is characterized and compared to the theoretical performance

Chapter 7 Outlook: This chapter gives an outlook of work which can be performed in order to bring the system closer to being approved for spaceflight. Some of the issues discussed here are meant as improvements to the system,

and others are stated since they are required to be solved to finalize the system.

Chapter 8 Conclusion: Finally the thesis concludes on the experimental work, regarding both the introduction of LTCC, the fabrication and the characterization.

Appendix A Theoretical Plots: Theoretical plots of mass flow and chamber pressure

Appendix B Pictures From Prototyping/Fabrication: Images acquired of the LTCC structures manufactured through out this project

Appendix C SEM Images Porous Materials: Images acquired using Scanning Electron Microscopy of different meterials, to investigate their porosity

Appendix D Dimensional Drawings: Engineering drawings of the mechanical parts manufactured for the tools aiding the thruster fabrication, as well as the parts for the test setup

Chapter 3

Disturbance Forces

Studying the disturbance forces acting on a spacecraft in a near Earth orbit, has three purposes in this thesis. First to understand the problem that substantiates the necessity of including a micropropulsion system on a drag free and/or formation flying mission. Second to develop a model from which the disturbance forces on a spacecraft can be deduced and third to use that model to deduce the requirements that a micropropulsion system has to fulfill in order to compensate for the disturbances. The latter will be approached using a highly relevant satellite mission - utilizing the so-called drag free flight - as a template. With drag free flight is understood a flight mode, for which all non-gravitational accelerations are compensated for by an actuation system. The satellite mission to be used as a template is the MICROSCOPE drag free mission presented in Chapter 1 Section 1.2.4. Although the MICROSCOPE mission is being used as a template for the following analysis, focus will be on making it generally adaptable to almost any drag free or formation flying mission. Hence the analysis will start out by presenting some of the necessary tools to be used in the modeling.

3.1 Frame Definitions

For determining the position and attitude of a spacecraft and for finding the direction of the individual disturbance forces treated in this project, we will in the following define the necessary coordinate frames. Three coordinate frames are used throughout this chapter, including:

1. A geocentric frame G defined by the unit vectors: $\hat{\boldsymbol{x}}_G$, $\hat{\boldsymbol{y}}_G$ and $\hat{\boldsymbol{z}}_G$, as seen in Figure 3.1. $\hat{\boldsymbol{x}}_G$ is pointing towards the Sun at the vernal equinox, $\hat{\boldsymbol{y}}_G$ is

lying in the equatorial plane perpendicular to $\hat{\boldsymbol{x}}_G$ and $\hat{\boldsymbol{z}}_G$ is pointing towards north along the rotational axis of Earth.

2. A frame L called LVLH defining the Local Vertical and Local Horizontal of the spacecraft by: $\hat{\boldsymbol{e}}_N$, $\hat{\boldsymbol{e}}_T$ and $\hat{\boldsymbol{e}}_R$, as seen in Figure 3.2. Here $\hat{\boldsymbol{e}}_N$ is normal to the orbit plane pointing along the angular momentum vector, $\hat{\boldsymbol{e}}_T$ is coincident with both the local horizontal plane and the orbit plane and $\hat{\boldsymbol{e}}_R$ is collinear with the position vector of the spacecraft in the geocentric frame (positive outwards).

3. The body frame of the spacecraft of interest $\hat{\boldsymbol{x}}_{sat}, \hat{\boldsymbol{y}}_{sat}, \hat{\boldsymbol{z}}_{sat}$. Defined according to what ever is convenient for the spacecraft on interest. For the definition of the spacecraft frame of the MICROSCOPE satellite, please refer to Section 3.10.1 in this chapter.

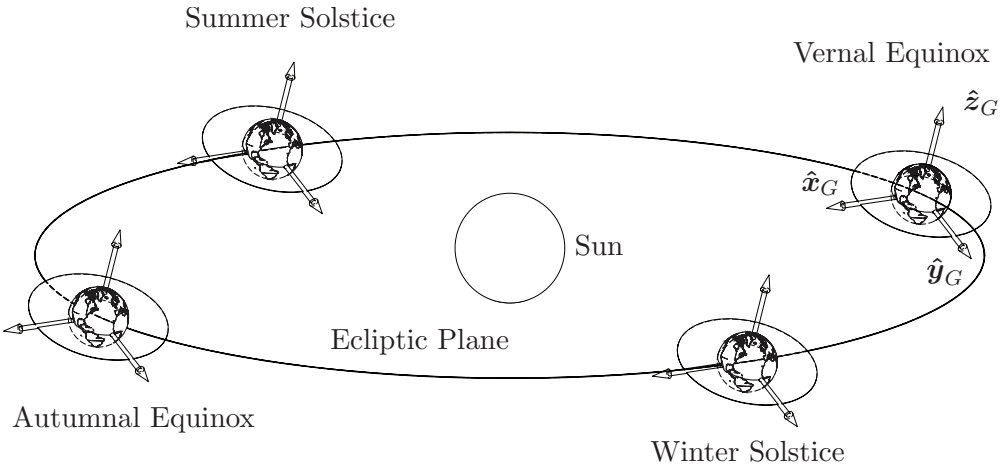

Figure 3.1: Definition of the geocentric frame. This frame is defined in relation to the equatorial plane, the north pole and the direction towards the Sun at the Vernal Equinox.

The attitude of the spacecraft with respect to the $\hat{\boldsymbol{e}}_N$, $\hat{\boldsymbol{e}}_T$ and $\hat{\boldsymbol{e}}_R$ axes of the LVLH frame respectively, is defined by the three Euler angles called pitch, roll and yaw, which we for MICROSCOPE define as the rotations about the $\hat{\boldsymbol{x}}_{sat}$, $\hat{\boldsymbol{y}}_{sat}$ and $\hat{\boldsymbol{z}}_{sat}$ respectively.

3.2 Orbital Elements

Modeling the disturbance forces, the classical method for defining the position of a secondary body orbiting a primary, will be used. Hence, this section will present how the classical six Keplerian elements should be interpreted, and how

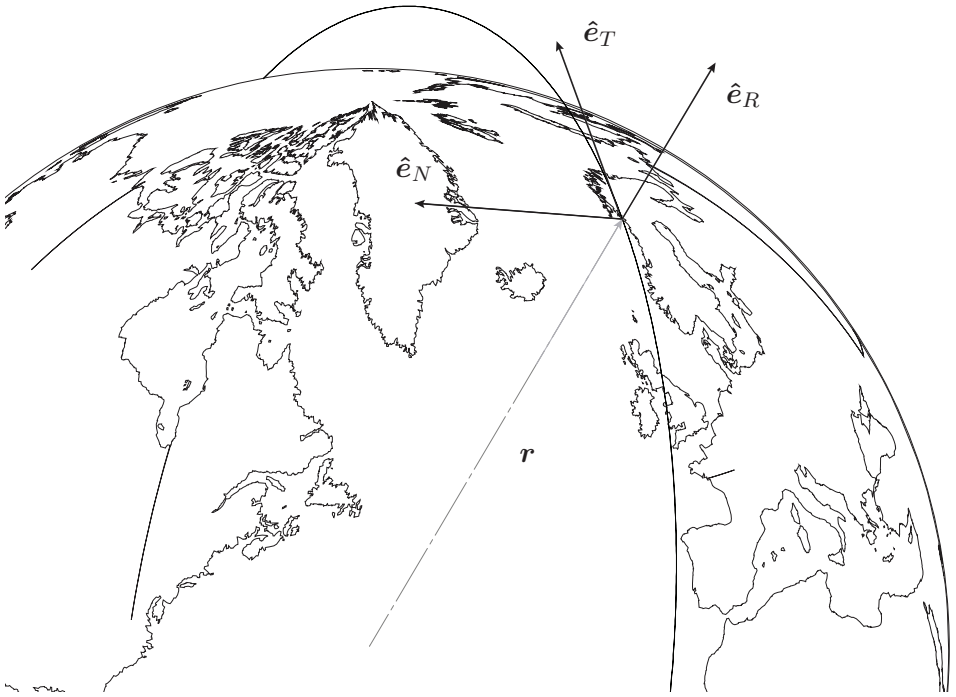

Figure 3.2: Definition of the Local Vertical Local Horizontal (LVLH) Frame. This frame is defined in relation to the orbital plane of the spacecraft of interest, its position vector and its angular momentum vector.

they relate to the Cartesian geocentric reference frame defined earlier. Depending on the initial speed of a body in space, when approaching the vicinity of another celestial body, it can either go into an elliptic orbit around that other body or escape through a hyperbolic trajectory. However, in the case that it has very specific speeds, it can also go into a circular orbit (special case of elliptic orbit with an eccentricity equal to zero) or escape through a parabolic trajectory (special case with eccentricity equal to one). Together with the *semimajor axis* a, the *eccentricity* e determines the shape of an orbit, being two of the six Keplerian elements. The orientation of that orbit can then be described by the remaining four of the six Keplerian Elements, reading:

- *Inclination* i The angle by which the orbital plane is tilted with respect to the plane of reference, measured at the ascending node.
- *Right ascension of the ascending node* Ω The angle between the chosen reference direction - lying in the reference plane - and the line going to the ascending node of the orbit (intersection line between the plane of reference and the orbital plane).

- *Argument of periapsis* ω The angle from the intersection line - between the plane of reference and the orbital plane - to the direction in which the distance between the two bodies is shortest, thereby determining the orientation of the elliptic orbit in the orbit plane.
- *Mean anomaly* M A mathematically convenient "angle" defining the position at a given time of the orbiting body along the defined ellipse. Can be converted into the *True anomaly* ν.

The *mean anomaly* varies linearly with time and does not correspond to a real geometric angle, but determines how large a fraction of a full orbit the satellite has passed, contrary to the *True anomaly* which varies non-linearly with time due to the periodic increase and decrease of the speed in an elliptic orbit. Hence, the true anomaly represents the real geometric angle in the plane of the ellipse, between periapsis (position at closest approach to the central body) and the position of the orbiting object at any given time, as seen on Figure 3.3.

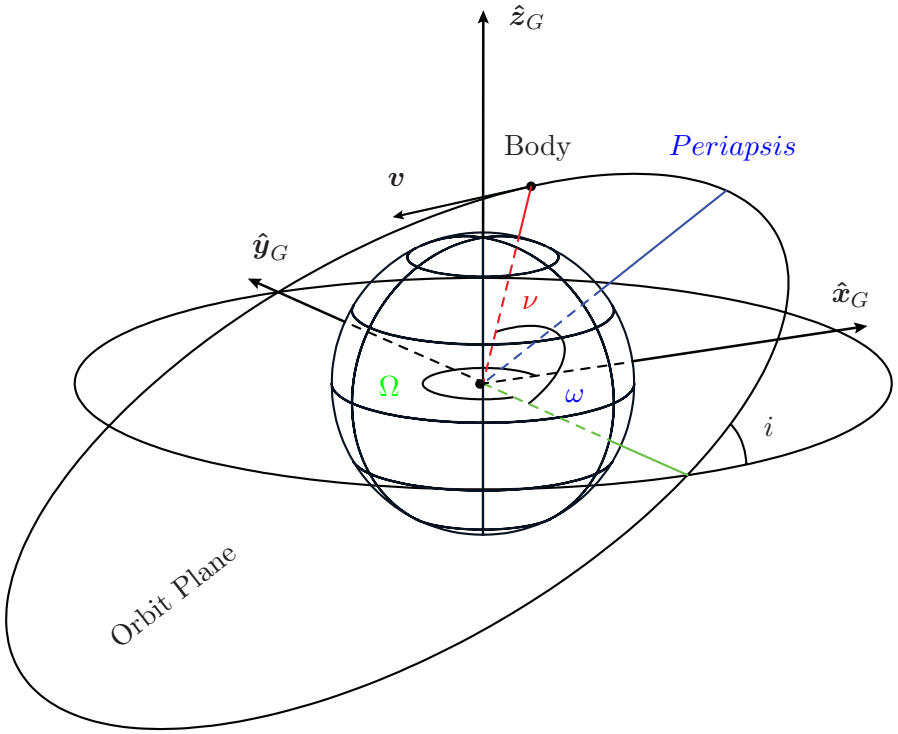

Figure 3.3: Illustration of the determination of the position of a spacecraft in an elliptic orbit by the six Keplerian elements and their relation to the Cartesian geocentric reference frame.

Consequently, by determining the orbital period T of a satellite, the rate of change of the mean anomaly can be determined and from the duration of the flight the position of the satellite is then known by the mean anomaly.

$$T = 2\pi\sqrt{\frac{a^3}{\mu}} \tag{3.1}$$

where μ is the gravitational parameter for Earth: $\mu = m_E G$, where m_E is the mass of the Earth and G is the universal gravitational constant.

Subsequently, the true anomaly can be determined from the mean anomaly via the eccentric anomaly by [26]:

$$E = e\sin(E) + M \tag{3.2}$$

$$\nu = 2\arctan\left(\sqrt{\frac{1+e}{1-e}}\tan(E/2)\right) \tag{3.3}$$

$$r = \frac{a(1-e^2)}{1+e\cos(\nu)} \tag{3.4}$$

where the eccentric anomaly E is defined as the angle indicating the swept area of the auxiliary circle, being the circle with the smallest possible radius which is still able to enclose the entire elliptic orbit, as seen on Figure 3.4.

Having the true anomaly, the Cartesian coordinates of the secondary body with respect to the primary is simply found by trigonometry:

$$x = r(\cos(\Omega)\cos(\omega+\nu) - \sin(\Omega)\sin(\omega+\nu)\cos(i)) \tag{3.5}$$

$$y = r(\sin(\Omega)\cos(\omega+\nu) + \cos(\Omega)\sin(\omega+\nu)\cos(i)) \tag{3.6}$$

$$z = r\sin(i)\sin(\omega+\nu) \tag{3.7}$$

Here x and y is lying in the plane of reference - normally the equatorial plane of the primary - with x pointing along the chosen reference direction - normally the direction towards the Sun at the vernal equinox. And finally z is oriented according to the right hand rule, perpendicularly to the plane of reference.

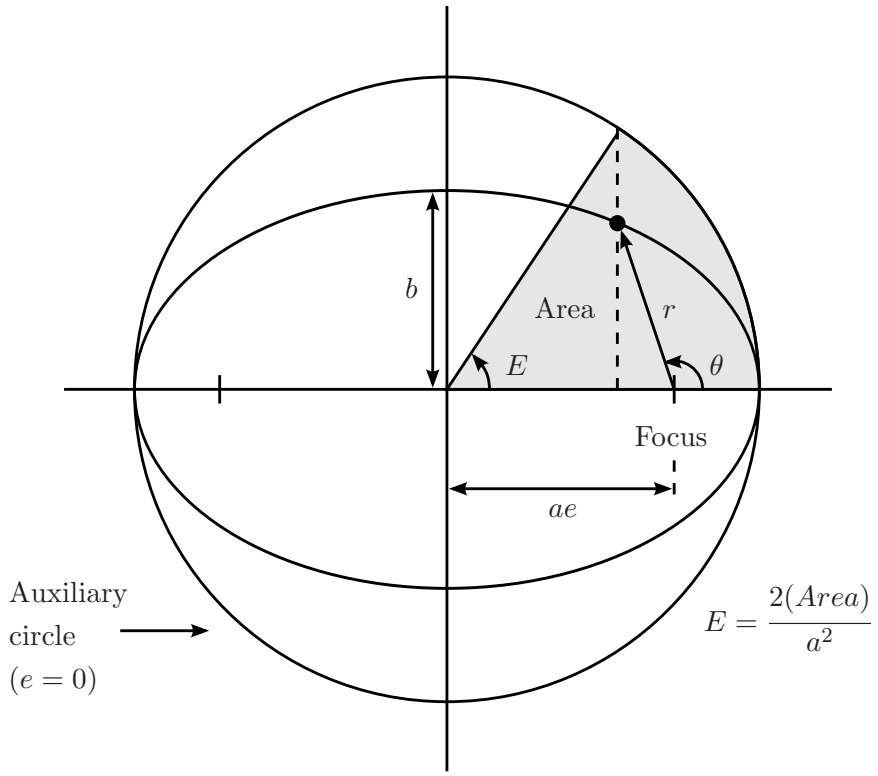

Figure 3.4: Definition of the eccentric anomaly. The eccentric anomaly is the angle indicating the swept area of the auxiliary circle, which is the circle with the smallest possible radius - yet enclosing the entire elliptic orbit [26].

3.3 Differential Orbital Elements

When flying formation with two or more spacecrafts, the relative position between the spacecrafts is described by differential orbital elements. These are useful for finding safe flight modes where collision is avoided and in order to reduce the necessary maneuver corrections. Unless the spacecrafts are flying perfectly on track in a common orbital plane their trajectories might cross and provide a risk of collision. Therefore it is necessary to constantly compensate for the gravitational differential forcing on the spacecrafts in a formation. To get an understanding of this problem, we include here the the equations of motion of a Deputy satellite with respect to a Chief, from the development of the Prisma control design, prepared in [12].

In a formation, typically one satellite is chosen as Chief, from which the relative motion of the other satellites (the Deputies) in the formation is described. The relative position and velocity between a Chief satellite and a Deputy satellite is in the LVLH frame of the Chief described by:

$$\Delta \boldsymbol{r} = \boldsymbol{r}_D - \boldsymbol{r} = \Delta r_R \hat{\boldsymbol{e}}_R + \Delta r_T \hat{\boldsymbol{e}}_T + \Delta r_N \hat{\boldsymbol{e}}_N \tag{3.8}$$

$$\Delta \boldsymbol{v} = \boldsymbol{v}_D - \boldsymbol{v} = \Delta v_R \hat{\boldsymbol{e}}_R + \Delta v_T \hat{\boldsymbol{e}}_T + \Delta v_N \hat{\boldsymbol{e}}_N \tag{3.9}$$

where $\boldsymbol{r}_D$ and $\boldsymbol{v}_D$ are the inertial position and velocity of the deputy satellite. Similarly to this representation, a description in terms of differential orbital elements / relative orbital elements can be implemented to get immediate insight into the constellation of the satellite formation. These are based on the relative semimajor axis Δa, the relative mean argument of latitude Δu ($u = \omega + M$), the relative eccentricity vector $\Delta \boldsymbol{e} = (\Delta e_x, \Delta e_y)^T$ and the relative inclination vector $\Delta \boldsymbol{i} = (\Delta i_x, \Delta i_y)^T$. The six parameters are defined as the difference of the orbital elements of Chief and Deputy:

$$\Delta a = a_D - a, \quad \Delta e_x = e_D \cos(\omega_D) - e\cos(\omega), \quad \Delta i_x = i_D - i \tag{3.10}$$

$$\Delta u = u_D - u, \quad \Delta e_y = e_D \sin(\omega_D) - e\sin(\omega), \quad \Delta i_y = (\Omega_D - \Omega)\sin(i) \tag{3.11}$$

Looking at the Chief satellite perpendicularly to its orbit plane, the relative eccentricity vector characterizes the observed motion of the Deputy satellite relative to the Chief (also known as the in-plane relative motion), by combining the orbit eccentricity e and the argument of perigee ω. Looking along the track of the Chief spacecraft, the relative inclination vector characterizes the motion (known as the out-of-plane relative motion), by combining the orbit inclination and right ascension of the ascending node Ω.

Recalling the Keplerian elements described earlier, the *mean argument of latitude* we use here, is the sum of the mean anomaly and the argument of periapsis ($u = \omega + M$). Using a Cartesian representation of the relative eccentricity and inclination vectors, the notation applied reads:

$$\Delta \boldsymbol{e} = \delta e \cdot (\cos\phi, \sin\phi) \tag{3.12}$$

$$\Delta \boldsymbol{i} = \delta i \cdot (\sin\theta, \cos\theta) \tag{3.13}$$

Hence, the amplitudes of the vectors read δe and δi respectively, and the phases are denoted the relative perigee ϕ and the relative latitude θ. Writing

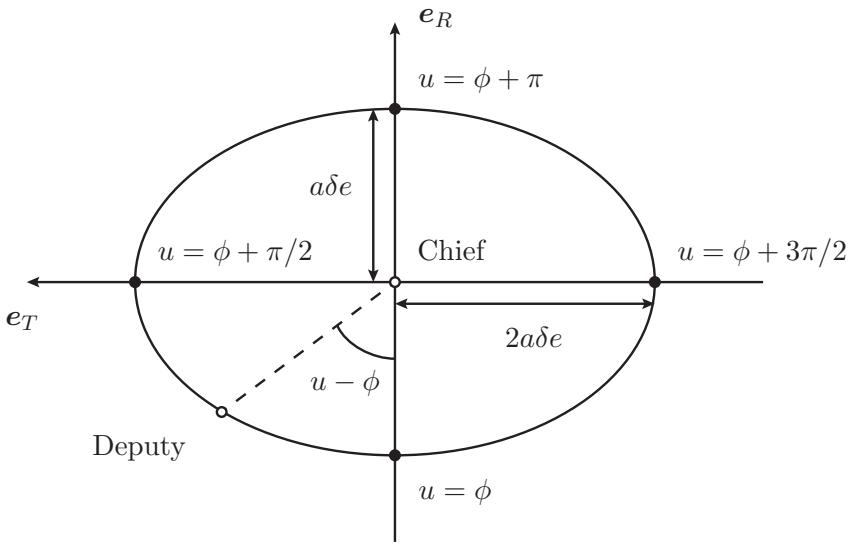

Figure 3.5: In-plane relative motion of the Deputy satellite with recpect to Chief.

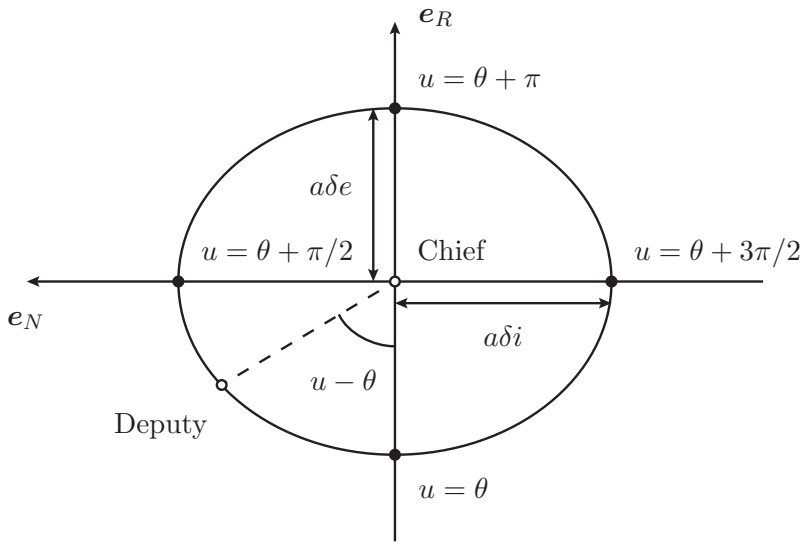

Figure 3.6: Out-of-plane relative motion of the Deputy satellite with respect to Chief.

the equations of motion in terms of the Cartesian position vector $\Delta \boldsymbol{r}$ defined in Equation 3.8, we have from [12]:

$$\Delta r_R/a = \Delta a/a - \Delta e_x \cos(u) - \cdot \Delta e_y \sin(u) \tag{3.14}$$

$$\Delta r_T/a = \Delta l - \frac{3}{2}\frac{\Delta a}{a}(u - u_0) + 2\Delta e_x \sin(u) - 2\Delta e_y \cos(u) \tag{3.15}$$

$$\Delta r_N/a = \Delta i_x \sin(u) - \Delta i_y \cos(u) \tag{3.16}$$

The $u_0 = u(t_0)$ is the initial mean argument of latitude and $\Delta l = \Delta u + \Delta\Omega\cos(i)$ is the relative mean orbital longitudes of both spacecrafts. Alternatively the polar notation from Equation 3.12 and 3.13 can be applied, giving:

$$\Delta r_R/a = \Delta a/a - \delta e\cos(u-\phi) \tag{3.17}$$

$$\Delta r_T/a = \Delta l - \frac{3}{2}\frac{\Delta a}{a}(u-u_0) + 2\delta e\sin(u-\phi) \tag{3.18}$$

$$\Delta r_N/a = \delta i\sin(u-\theta) \tag{3.19}$$

For close relative orbits of the Deputy spacecraft centered on the Chief, we have $\Delta a \approx 0$ and $\Delta u = -\Delta\Omega\cos(i)$, providing two of the six relative orbital elements. Consequently, the relative motion is dependent solely on the phase and amplitude of the relative eccentricity and inclination vectors, as illustrated in Figure 3.5 and 3.6. As a result, collision is prevented between the spacecrafts as long as the relative eccentricity and inclination vectors are non-parallel (giving $\phi = \theta$). In this situation the minimum distance between the spacecrafts will be $\min(a\delta e, a\delta i)$.

Looking at the Chief satellite perpendicularly to its orbit plane, the relative trajectory of the spacecrafts is an ellipse with semi-major axis $2a\delta e$ along track, and semi-minor axis $a\delta e$ radially, as seen on Figure 3.5. Looking along the track of the Chief spacecraft, the relative trajectory of the spacecrafts is an ellipse with semi-major axis $\min(a\delta e, a\delta i$ along track, and semi-minor axis $\min(a\delta e, a\delta i$ radially, as seen on Figure 3.6. A collision free configuration is achieved, providing a minimum separation between the spacecrafts, as opposed to having parallel relative eccentricity and inclination vectors, which certainly gives problems when having large uncertainties in along-track separation.

3.4 Coordinate Transformation

The purpose of the following Section is to become familiar with some of the most important mathematical tools to be used in the description of the rotational kinematics of a body in space. Describing the orientation / attitude of a body, one would initially define a fixed reference frame in relation to some of the geometry of that body. Normally one would choose a right hand frame with three orthogonal axes, for instance called $B = \{\hat{\boldsymbol{b}}_1, \hat{\boldsymbol{b}}_2, \hat{\boldsymbol{b}}_3\}$. Having this defined, the orientation of the body can be described with respect to any inertial reference frame

$A = \{\hat{\boldsymbol{a}}_1, \hat{\boldsymbol{a}}_2, \hat{\boldsymbol{a}}_3\}$ by matrix multiplication of the rotation matrix also called the Direction Cosine Matrix (DCM):

$$\begin{bmatrix} \hat{\boldsymbol{b}}_1 \\ \hat{\boldsymbol{b}}_2 \\ \hat{\boldsymbol{b}}_3 \end{bmatrix} = \begin{bmatrix} C_{11} & C_{12} & C_{13} \\ C_{21} & C_{22} & C_{23} \\ C_{31} & C_{32} & C_{33} \end{bmatrix} \begin{bmatrix} \hat{\boldsymbol{a}}_1 \\ \hat{\boldsymbol{a}}_2 \\ \hat{\boldsymbol{a}}_3 \end{bmatrix} \tag{3.20}$$

The individual elements $[C_{ij}]$ of the cosine matrix $\boldsymbol{C}^{B/A}$ is simply the scalar product between $\hat{\boldsymbol{b}}_i$ and $\hat{\boldsymbol{a}}_j$ and since $\hat{\boldsymbol{b}}_1 \cdot \hat{\boldsymbol{a}}_1 = |\hat{\boldsymbol{b}}_1||\hat{\boldsymbol{a}}_1| \cos(\theta_2)\cos(\theta_3) = \cos(\theta_2)\cos(\theta_3)$ it is called the direction cosine matrix. Hence, we have:

$$\boldsymbol{C}^{B/A} = \begin{bmatrix} \hat{\boldsymbol{b}}_1 \cdot \hat{\boldsymbol{a}}_1 & \hat{\boldsymbol{b}}_1 \cdot \hat{\boldsymbol{a}}_2 & \hat{\boldsymbol{b}}_1 \cdot \hat{\boldsymbol{a}}_3 \\ \hat{\boldsymbol{b}}_2 \cdot \hat{\boldsymbol{a}}_1 & \hat{\boldsymbol{b}}_2 \cdot \hat{\boldsymbol{a}}_2 & \hat{\boldsymbol{b}}_2 \cdot \hat{\boldsymbol{a}}_3 \\ \hat{\boldsymbol{b}}_3 \cdot \hat{\boldsymbol{a}}_1 & \hat{\boldsymbol{b}}_3 \cdot \hat{\boldsymbol{a}}_2 & \hat{\boldsymbol{b}}_3 \cdot \hat{\boldsymbol{a}}_3 \end{bmatrix} = \begin{bmatrix} \hat{\boldsymbol{b}}_1 \\ \hat{\boldsymbol{b}}_2 \\ \hat{\boldsymbol{b}}_3 \end{bmatrix} \cdot \begin{bmatrix} \hat{\boldsymbol{a}}_1 & \hat{\boldsymbol{a}}_2 & \hat{\boldsymbol{a}}_3 \end{bmatrix} \tag{3.21}$$

Showing that the rotation matrix or coordinate transformation matrix to B from A, is actually the product between the two basis vectors of those frames.

Having any arbitrary vector $\boldsymbol{H}$ with the coordinates $\boldsymbol{H} = H_1\hat{\boldsymbol{a}}_1 + H_2\hat{\boldsymbol{a}}_2 + H_3\hat{\boldsymbol{a}}_3$ and $\boldsymbol{H} = H_1'\hat{\boldsymbol{b}}_1 + H_2'\hat{\boldsymbol{b}}_2 + H_3'\hat{\boldsymbol{b}}_3$ in the reference frame A and B respectively, we can write [15]:

$$\begin{aligned} H_1' &\equiv \hat{\boldsymbol{b}}_1 \cdot \boldsymbol{H} = \hat{\boldsymbol{b}}_1 \cdot (H_1\hat{\boldsymbol{a}}_1 + H_2\hat{\boldsymbol{a}}_2 + H_3\hat{\boldsymbol{a}}_3) \\ H_2' &\equiv \hat{\boldsymbol{b}}_2 \cdot \boldsymbol{H} = \hat{\boldsymbol{b}}_2 \cdot (H_1\hat{\boldsymbol{a}}_2 + H_2\hat{\boldsymbol{a}}_2 + H_3\hat{\boldsymbol{a}}_3) \\ H_3' &\equiv \hat{\boldsymbol{b}}_3 \cdot \boldsymbol{H} = \hat{\boldsymbol{b}}_3 \cdot (H_1\hat{\boldsymbol{a}}_1 + H_2\hat{\boldsymbol{a}}_2 + H_3\hat{\boldsymbol{a}}_3) \end{aligned}$$

Which is written in matrix form as:

$$\begin{bmatrix} H_1' \\ H_2' \\ H_3' \end{bmatrix} = \begin{bmatrix} \hat{\boldsymbol{b}}_1 \cdot \hat{\boldsymbol{a}}_1 & \hat{\boldsymbol{b}}_1 \cdot \hat{\boldsymbol{a}}_2 & \hat{\boldsymbol{b}}_1 \cdot \hat{\boldsymbol{a}}_3 \\ \hat{\boldsymbol{b}}_2 \cdot \hat{\boldsymbol{a}}_1 & \hat{\boldsymbol{b}}_2 \cdot \hat{\boldsymbol{a}}_2 & \hat{\boldsymbol{b}}_2 \cdot \hat{\boldsymbol{a}}_3 \\ \hat{\boldsymbol{b}}_3 \cdot \hat{\boldsymbol{a}}_1 & \hat{\boldsymbol{b}}_3 \cdot \hat{\boldsymbol{a}}_2 & \hat{\boldsymbol{b}}_3 \cdot \hat{\boldsymbol{a}}_3 \end{bmatrix} \begin{bmatrix} H_1 \\ H_2 \\ H_3 \end{bmatrix} = \boldsymbol{C}^{B/A} \begin{bmatrix} H_1 \\ H_2 \\ H_3 \end{bmatrix} \tag{3.22}$$

Hence, any arbitrary vector is transferred to B from A by applying the same cosine matrix $\boldsymbol{C}^{B/A}$, as the one defined for the transformation of orthogonal basis vectors [15].

3.4.1 Euler Angles

When altering the attitude of a body from one orientation to another, this can be done in a sequence of rotations about each of the axes in the utilized body reference frame. The corresponding angles of these rotations are called Euler angles, from the leading mathematician and theoretical physicist of the 18'th century, Leonard Euler. To reach any arbitrary orientation from any given attitude, a sequence of 3 rotations is needed in general. This sequence can be chosen in 12 different ways, of which 6 of them utilizes all three axes and the remaining 6 only utilizes 2 axes by reusing the first one chosen. Hence, all the possible sequences reads:

3 axis sequences:	$\theta_1 \leftarrow \theta_2 \leftarrow \theta_3$	$\theta_1 \leftarrow \theta_3 \leftarrow \theta_2$	$\theta_2 \leftarrow \theta_1 \leftarrow \theta_3$
	$\theta_3 \leftarrow \theta_1 \leftarrow \theta_2$	$\theta_2 \leftarrow \theta_3 \leftarrow \theta_1$	$\theta_3 \leftarrow \theta_2 \leftarrow \theta_1$
2 axis sequences:	$\theta_3 \leftarrow \theta_1 \leftarrow \theta_3$	$\theta_2 \leftarrow \theta_1 \leftarrow \theta_2$	$\theta_1 \leftarrow \theta_3 \leftarrow \theta_1$
	$\theta_2 \leftarrow \theta_3 \leftarrow \theta_2$	$\theta_3 \leftarrow \theta_2 \leftarrow \theta_3$	$\theta_1 \leftarrow \theta_2 \leftarrow \theta_1$

The arrows turning left, is just for the sequences to be consistent with the order of which the rotation matrices should be multiplied, in order to reach the right rotation matrix. Hence, for the sequence $\theta_1 \leftarrow \theta_2 \leftarrow \theta_3$ - which is equal to $\theta_3 \rightarrow \theta_2 \rightarrow \theta_1$ - the matrix multiplication reads:

$$\boldsymbol{C}^{B/A} = \boldsymbol{C}_1(\theta_1)\boldsymbol{C}_2(\theta_2)\boldsymbol{C}_3(\theta_3)$$

Where we can deduce from the definition of the cosine matrix, that:

$$\boldsymbol{C}_1(\theta_1) = \begin{bmatrix} 1 & 0 & 0 \\ 0 & \cos(\theta_1) & \sin(\theta_1) \\ 0 & -\sin(\theta_1) & \cos(\theta_1) \end{bmatrix} \tag{3.23}$$

$$\boldsymbol{C}_2(\theta_2) = \begin{bmatrix} \cos(\theta_2) & 0 & -\sin(\theta_2) \\ 0 & 1 & 0 \\ \sin(\theta_2) & 0 & \cos(\theta_2) \end{bmatrix} \tag{3.24}$$

$$\boldsymbol{C}_3(\theta_3) = \begin{bmatrix} \cos(\theta_3) & \sin(\theta_3) & 0 \\ -\sin(\theta_3) & \cos(\theta_3) & 0 \\ 0 & 0 & 1 \end{bmatrix} \tag{3.25}$$

The rotation matrix to B from A, or the direction cosine matrix of B relative to A, is then defined as:

$$\boldsymbol{C}^{B/A} = \boldsymbol{C}_1(\theta_1)\boldsymbol{C}_2(\theta_2)\boldsymbol{C}_3(\theta_3) = \begin{bmatrix} \mathrm{c}_2\mathrm{c}_3 & \mathrm{c}_2\mathrm{s}_3 & -\mathrm{s}_2 \\ \mathrm{s}_1\mathrm{s}_2\mathrm{c}_3 - \mathrm{c}_1\mathrm{s}_3 & \mathrm{s}_1\mathrm{s}_2\mathrm{s}_3 + \mathrm{c}_1\mathrm{c}_3 & \mathrm{s}_1\mathrm{c}_2 \\ \mathrm{c}_1\mathrm{s}_2\mathrm{c}_3 + \mathrm{s}_1\mathrm{s}_3 & \mathrm{c}_1\mathrm{s}_2\mathrm{s}_3 - \mathrm{s}_1\mathrm{c}_3 & \mathrm{c}_1\mathrm{c}_2 \end{bmatrix}$$

where $\mathrm{c}_i \equiv \cos(\theta_i)$ and $\mathrm{s}_i \equiv \sin(\theta_i)$. In general there are 12 sets of Euler angles, each resulting in a different form for the rotation matrix $\boldsymbol{C}^{B/A}$.

3.4.2 Quaternions

When rotating about the three orthogonal body axes for altering the orientation of a body from one attitude to another, three consecutive rotations are needed in general. However, having stated any arbitrarily chosen rotation from one attitude to another, there always exists an axis, for which only one rotation is needed to bring the body into the new orientation. Such an axis is unique for that rotation and is accordingly called an eigenaxis. Consequently, four dimensional hypercomplex numbers can be used to define rotations from one orientation to another, since we now only have four unknown parameters for a rotation: the three elements of the eigenaxis vector to rotate about, and the angle of the rotation. These four dimensional hypercomplex numbers are called Euler parameters or Quaternions, and are defined as [15]:

$$q_1 = e_1 \sin(\theta/2) \tag{3.26}$$
$$q_2 = e_2 \sin(\theta/2) \tag{3.27}$$
$$q_3 = e_3 \sin(\theta/2) \tag{3.28}$$
$$q_4 = \cos(\theta/2) \tag{3.29}$$

Consider the body-fixed rotational sequence to B from A defined by the three Euler angles θ_1, θ_2 and θ_3: $\boldsymbol{C}_1(\theta_1) \leftarrow \boldsymbol{C}_2(\theta_2) \leftarrow \boldsymbol{C}_3(\theta_3)$. The three Euler angles of this rotational sequence are related to quaternions, as follows.

The transformation to B from A is initially divided into the three separate rotations $\boldsymbol{C}_1(\theta_1) \leftarrow \boldsymbol{C}_2(\theta_2) \leftarrow \boldsymbol{C}_3(\theta_3)$. For each of these rotations it is straight

forward to determine the quaternions from the definition stated in Equation 3.26 to 3.29. Here we have for the $\boldsymbol{C}_1(\theta_1)$ rotation, that $e_1 = 1$, $e_2 = 0$ and $e_3 = 0$ since rotation is done solely about the first axis. Hence, the quaternions for each of the three rotations read:

$$\boldsymbol{C}_1(\theta_1) \leftarrow \boldsymbol{C}_2(\theta_2) \leftarrow \boldsymbol{C}_3(\theta_3) \Rightarrow \begin{bmatrix} \sin(\theta_1/2) \\ 0 \\ 0 \\ \cos(\theta_1/2) \end{bmatrix} \leftarrow \begin{bmatrix} 0 \\ \sin(\theta_2/2) \\ 0 \\ \cos(\theta_2/2) \end{bmatrix} \leftarrow \begin{bmatrix} 0 \\ 0 \\ \sin(\theta_3/2) \\ \cos(\theta_3/2) \end{bmatrix}$$

Having the quaternions from two separate rotations, the quaternion corresponding to the collective transformation can be found using this relation from [15]:

$$\begin{bmatrix} q_1 \\ q_2 \\ q_3 \\ q_4 \end{bmatrix} = \begin{bmatrix} q''_4 & q''_3 & -q''_2 & q''_1 \\ -q''_3 & q''_4 & q''_1 & q''_2 \\ q''_2 & -q''_1 & q''_4 & q''_3 \\ -q''_1 & -q''_2 & -q''_3 & q''_4 \end{bmatrix} \begin{bmatrix} q'_1 \\ q'_2 \\ q'_3 \\ q'_4 \end{bmatrix}$$

Hence, for the collective transformation $\boldsymbol{C}_2(\theta_2) \leftarrow \boldsymbol{C}_3(\theta_3)$ we have:

$$\begin{bmatrix} \cos\left(\frac{\theta_2}{2}\right) & 0 & -\sin\left(\frac{\theta_2}{2}\right) & 0 \\ 0 & \cos\left(\frac{\theta_2}{2}\right) & 0 & \sin\left(\frac{\theta_2}{2}\right) \\ \sin\left(\frac{\theta_2}{2}\right) & 0 & \cos\left(\frac{\theta_2}{2}\right) & 0 \\ 0 & -\sin\left(\frac{\theta_2}{2}\right) & 0 & \cos\left(\frac{\theta_2}{2}\right) \end{bmatrix} \begin{bmatrix} 0 \\ 0 \\ \sin\left(\frac{\theta_3}{2}\right) \\ \cos\left(\frac{\theta_3}{2}\right) \end{bmatrix} =$$

$$\begin{bmatrix} -\sin\left(\frac{\theta_2}{2}\right)\sin\left(\frac{\theta_3}{2}\right) \\ \sin\left(\frac{\theta_2}{2}\right)\cos\left(\frac{\theta_3}{2}\right) \\ \cos\left(\frac{\theta_2}{2}\right)\sin\left(\frac{\theta_3}{2}\right) \\ \cos\left(\frac{\theta_2}{2}\right)\cos\left(\frac{\theta_3}{2}\right) \end{bmatrix}$$

And for the collective transformation $\boldsymbol{C}_1(\theta_1) \leftarrow \boldsymbol{C}_2(\theta_2) \leftarrow \boldsymbol{C}_3(\theta_3)$ we then have:

$$\begin{bmatrix} \cos\left(\frac{\theta_1}{2}\right) & 0 & 0 & \sin\left(\frac{\theta_1}{2}\right) \\ 0 & \cos\left(\frac{\theta_1}{2}\right) & \sin\left(\frac{\theta_1}{2}\right) & 0 \\ 0 & -\sin\left(\frac{\theta_1}{2}\right) & \cos\left(\frac{\theta_1}{2}\right) & 0 \\ -\sin\left(\frac{\theta_1}{2}\right) & 0 & 0 & \cos\left(\frac{\theta_1}{2}\right) \end{bmatrix} \begin{bmatrix} -\sin\left(\frac{\theta_2}{2}\right)\sin\left(\frac{\theta_3}{2}\right) \\ \sin\left(\frac{\theta_2}{2}\right)\cos\left(\frac{\theta_3}{2}\right) \\ \cos\left(\frac{\theta_2}{2}\right)\sin\left(\frac{\theta_3}{2}\right) \\ \cos\left(\frac{\theta_2}{2}\right)\cos\left(\frac{\theta_3}{2}\right) \end{bmatrix} =$$

$$\begin{bmatrix} \sin\left(\frac{\theta_1}{2}\right)\cos\left(\frac{\theta_2}{2}\right)\cos\left(\frac{\theta_3}{2}\right) - \cos\left(\frac{\theta_1}{2}\right)\sin\left(\frac{\theta_2}{2}\right)\sin\left(\frac{\theta_3}{2}\right) \\ \cos\left(\frac{\theta_1}{2}\right)\sin\left(\frac{\theta_2}{2}\right)\cos\left(\frac{\theta_3}{2}\right) + \sin\left(\frac{\theta_1}{2}\right)\cos\left(\frac{\theta_2}{2}\right)\sin\left(\frac{\theta_3}{2}\right) \\ \cos\left(\frac{\theta_1}{2}\right)\cos\left(\frac{\theta_2}{2}\right)\sin\left(\frac{\theta_3}{2}\right) - \sin\left(\frac{\theta_1}{2}\right)\sin\left(\frac{\theta_2}{2}\right)\cos\left(\frac{\theta_3}{2}\right) \\ \cos\left(\frac{\theta_1}{2}\right)\cos\left(\frac{\theta_2}{2}\right)\cos\left(\frac{\theta_3}{2}\right) + \sin\left(\frac{\theta_1}{2}\right)\sin\left(\frac{\theta_2}{2}\right)\sin\left(\frac{\theta_3}{2}\right) \end{bmatrix} = \begin{bmatrix} q_1 \\ q_2 \\ q_3 \\ q_4 \end{bmatrix} \tag{3.30}$$

where (q_1, q_2, q_3, q_4) is the quaternion associated with the coordinate transformation $B \leftarrow A$. Having the quaternion, the coordinate transformation of a vector $\boldsymbol{v}$ from A to B is defined as:

$$\boldsymbol{v}_B = \boldsymbol{q}_{B\leftarrow A} \otimes \begin{bmatrix} \boldsymbol{v}_A \\ 0 \end{bmatrix} \otimes \boldsymbol{q}_{B\leftarrow A}^{-1}\boldsymbol{q} \tag{3.31}$$

where $\otimes$ is the operator of a quaternion multiplication defined by [13]:

$$\boldsymbol{r} \otimes \boldsymbol{p} = \boldsymbol{q} = \begin{bmatrix} q_1 \\ q_2 \\ q_3 \\ q_4 \end{bmatrix} = \begin{bmatrix} \boldsymbol{v}_q \\ s_q \end{bmatrix} = \begin{bmatrix} s_r\boldsymbol{v}_p + s_p\boldsymbol{v}_r + \boldsymbol{v}_r \times \boldsymbol{v}_p \\ s_r s_p - \boldsymbol{v}_r \cdot \boldsymbol{v}_p \end{bmatrix} \tag{3.32}$$

The quaternion method for coordinate transformation has no singularities and the computation is not as heavy as the DCM, with only three elements to compute. This makes the quaternion method more suitable for space applications where computational power is limited.

3.5 Nodal Regression

Nodal regression is one of the disturbances present due to the differing of the gravitational field of the Earth from that of a perfect sphere. The nodal regression

is due to the torque produced by the equatorial bulge of the Earth (or flattening), caused by Earth's own rotation. The consequence of this torque is a precession of the angular momentum vector of the orbit, causing an additional movement of the line of nodes to that being determined by the rotation of the Earth beneath the orbit. The total increase in longitude for the ascending crossing of the equator is illustrated in Figure 3.7, and is then given by:

$$\Delta\phi = \Delta\phi_1 + \Delta\phi_2 \tag{3.33}$$

where $\Delta\phi_1$ is the angle due to the rotation of the Earth and $\Delta\phi_2$ is the angle due to nodal regression. If the nodal period / orbital period of the satellite is τ, then the contribution to $\Delta\phi$ caused by Earth's rotation is given by:

$$\Delta\phi_1 = -2\pi\frac{\tau}{\tau_E} \text{ rad/orbit} \tag{3.34}$$

where τ_E is the time for one revolution of the Earth with respect to the stars, which is 23 hours and 56 minutes [26]. The 24 hours we define as one day, is obviously with respect to the sun. Neglecting all harmonic coefficients other than J_2 the rate of nodal regression may be written:

$$\Delta\phi_2 = -\frac{3\pi J_2 R_E^2 \cos(i)}{a^2(1-e^2)^2} \text{ rad/orbit} \tag{3.35}$$

where J_2 is one of the zonal harmonic coefficients reflecting the mass distribution of the Earth independently of longitude, when describing Earth's gravitational field outside its surface by a spherical harmonic expansion [26]. R_E is the radius of the Earth, i is the inclination of the orbit, a is the semi major axis and e is the eccentricity. Table 3.1 gives the magnitude of some of the lower order coefficients taken from a geoid model [26]. From this it is apparent that the value of the J_2 term - which represents the polar flattening of the Earth - is about three orders of magnitude larger than the others, and is therefore dominating the gravitational perturbative influences of the Earth.

J_2	1082.6×10^{-6}	C_{21}	0	S_{21}	0
J_3	-2.53×10^{-6}	C_{22}	1.57×10^{-6}	S_{22}	-0.904×10^{-6}
J_4	-1.62×10^{-6}	C_{31}	2.19×10^{-6}	S_{31}	0.27×10^{-6}
J_5	-0.23×10^{-6}	C_{32}	0.31×10^{-6}	S_{32}	-0.21×10^{-6}
J_6	0.54×10^{-6}	C_{33}	0.10×10^{-6}	S_{33}	0.197×10^{-6}

Table 3.1: Magnitude of some of the lower order coefficients: J, C and S taken from a current geoid model [26].

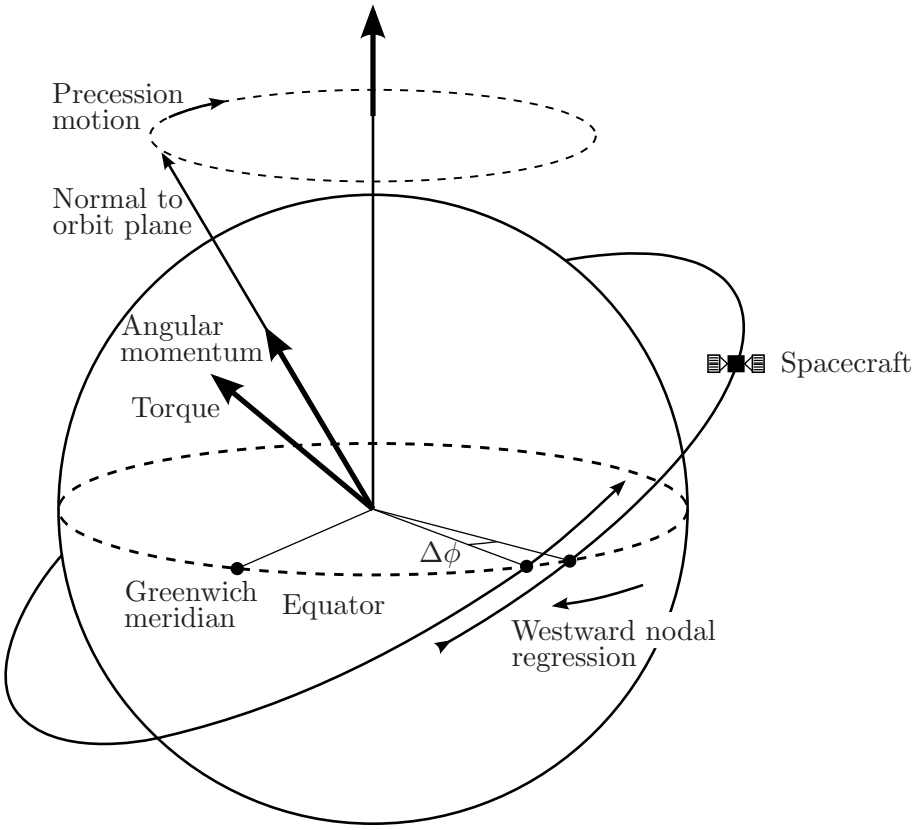

Figure 3.7: Illustration of the regression of the line of nodes, known as *Nodal Regression*, due to the contribution to the gravitational field from the equatorial bulge of the Earth.

3.6 Apsidal Precession

The equatorial bulge is also the cause of another perturbation from a keplerian orbit, called apsidal precession. When the spacecraft is crossing the equator, gravity increases compared to the mean due to the flattening of Earth. Consequently the orbit tends to curve more rapidly. However, since the gravitational field of the Earth is conservative, this leads to an overall rotation of the orbit within the orbit plane, as illustrated on Figure 3.8, the point at which the spacecraft is nearest Earth will move, meaning the argument of periapsis is altered with a rate given by [26]:

$$\Delta\omega = 3\pi \frac{J_2 R_E^2}{a^2(1-e^2)^2}\left(2 - \frac{5}{2}\sin^2(i)\right) \text{ rad/orbit} \tag{3.36}$$

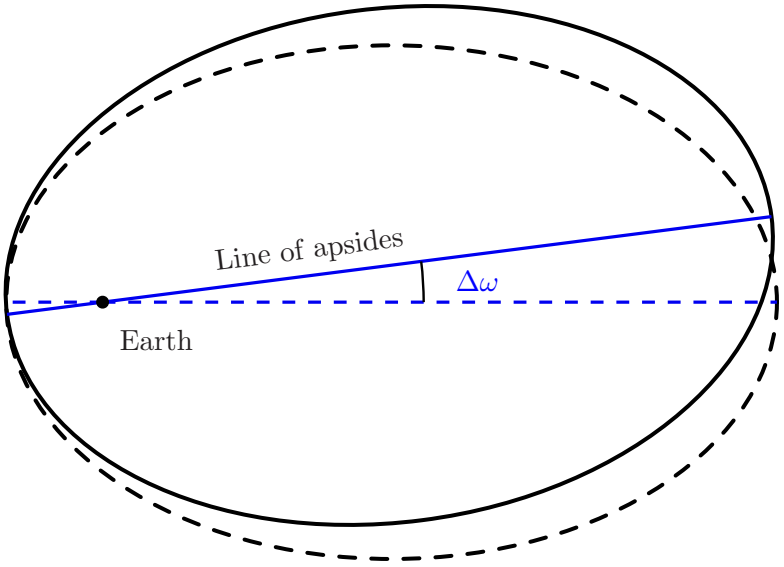

Figure 3.8: Illustration of the *Apsidal Precession*, due to the contribution to the gravitational field from the equatorial bulge of the Earth.

3.7 Atmospheric Drag

Atmospheric drag naturally varies in magnitude with altitude, but also with the solar activity. This is due to the fact that the EUV radiation from the sun is absorbed in the thermosphere, thereby heating it up and consequently expanding it. The sun also heats the atmosphere more indirectly by the solar wind through its effect on geomagnetic activity and particle precipitation, as the geomagnetic activity is a contributory cause of Joule dissipation. Of these contributions, the largest is in general the solar EUV radiation, however during periods of high magnetic activity, such as strong geomagnetic storms, the Joule heating can be excessive [25]. On Figure 3.9 the atmospheric density (which translates into atmospheric drag) is seen for different magnitudes of solar activity.

Solar forcing includes solar radiation and solar wind. Transient and dramatic changes in solar forcing occur during solar flares and magnetic storms. The thermosphere, with its large mass and high heat capacity, is generally thought to be sluggish in responding to these transient events. However, in the upper thermosphere where the air density is relatively low, early disturbances can be detected by instruments with high sensitivity. This has been demonstrated by several studies using the CHAMP high-resolution measurements [17]. These studies showed that

the thermosphere density increases several folds during magnetic storms within a few tens of minutes. Hence, the high density occurring at high solar activity should certainly be taken into account when dimensioning a micropropulsion system for LEO.

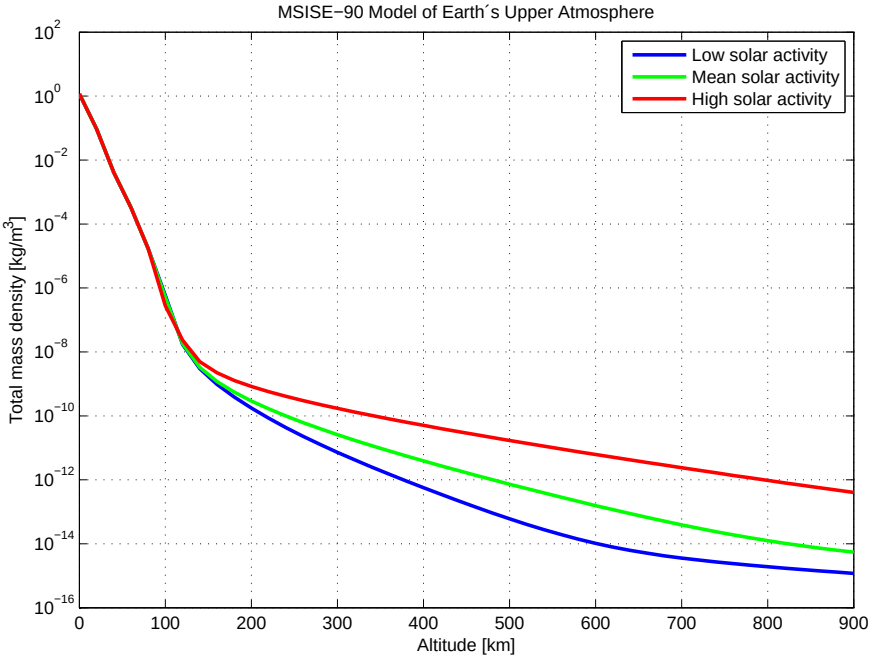

Figure 3.9: Atmospheric density and its dependency on altitude as well as solar activity. The data are from NASA's MSIS-E-90 Atmospheric Model.

Besides the changes in mass density denoted ρ, the atmospheric drag is also dependent on the size and form - which translate into the cross sectional area A and the drag coefficient C_D - of the spacecraft. Using these parameters, the atmospheric drag on a surface element of area $A(i)$ can be expressed by:

$$\boldsymbol{F}_{AD}(i) = -\frac{1}{2}\rho C_D v^2 \left(\hat{\boldsymbol{n}} \cdot \hat{\boldsymbol{v}}\right) \hat{\boldsymbol{v}} A(i) \tag{3.37}$$

where v and $\hat{\boldsymbol{v}}$ is the magnitude and direction of the spacecraft velocity respectively, which is determined from its orbital elements and current position within the orbit, and $\hat{\boldsymbol{n}}$ is the outward normal vector to the surface element. Using the area A_{sat} of a 2D projection of the spacecraft onto a plane perpendicular to the velocity vector, the two vectors $\hat{\boldsymbol{v}}$ and $\hat{\boldsymbol{n}}$ becomes parallel, and Equation 3.37 is simplified to:

$$\boldsymbol{F}_{AD} = -\frac{1}{2}\rho C_D v^2 \hat{\boldsymbol{v}} A_{sat} \tag{3.38}$$

The projected area is - depending on the shape of the spacecraft - changing with the attitude with respect to the current velocity as well as the drag coefficient. The drag coefficient is dependent on the aerodynamic shape, which for a few simple shapes is presented in Figure 3.10.

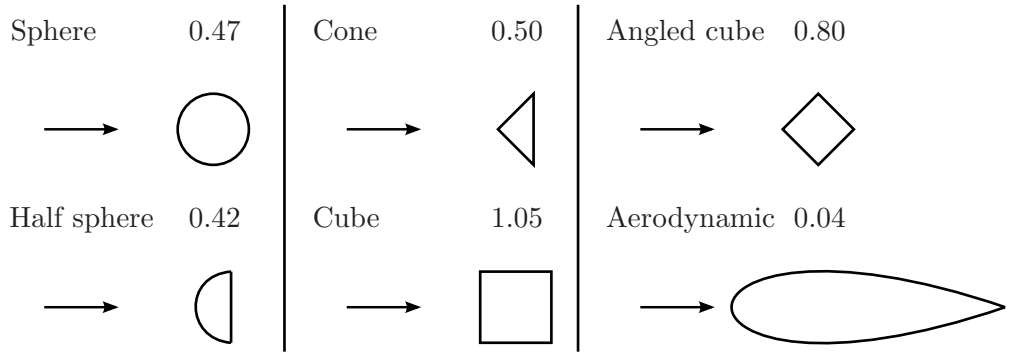

Figure 3.10: Approximate drag coefficients for different aerodynamic shapes. As the drag coefficient can vary more than one order of magnitude from the best aerodynamic shape to the worst, it is an important factor in the expression for the atmospheric drag [18].

The atmospheric drag is incident in a direction opposite the velocity vector of the spacecraft. Accordingly, the direction of the atmospheric drag can be found by taking the time derivative of the spacecraft position:

$$\hat{\boldsymbol{F}}_{AD,G} = -\hat{\boldsymbol{v}} = -\frac{d\boldsymbol{r}}{dt}\frac{1}{v} \tag{3.39}$$

where $\boldsymbol{v}$ is the velocity. According to the Equations 3.5 to 3.7, the position vector of the spacecraft $\boldsymbol{r}$ is determined form its orbital elements by:

$$\begin{aligned} \boldsymbol{r} &= r(\cos(\Omega)\cos(\omega+\nu) - \sin(\Omega)\sin(\omega+\nu)\cos(i))\hat{\boldsymbol{x}}_G \\ &+ r(\sin(\Omega)\cos(\omega+\nu) + \cos(\Omega)\sin(\omega+\nu)\cos(i))\hat{\boldsymbol{y}}_G \\ &+ r\sin(i)\sin(\omega+\nu)\hat{\boldsymbol{z}}_G \end{aligned} \tag{3.40}$$

Two successive coordinate transformations are then applied. First the AD is transferred to the LVLH frame ($\hat{\boldsymbol{e}}_N$, $\hat{\boldsymbol{e}}_T$, $\hat{\boldsymbol{e}}_R$), either by applying the rotation matrix from G to L:

$$\hat{\boldsymbol{F}}_{AD,L} = \boldsymbol{C}^{L/G}\hat{\boldsymbol{F}}_{AD,G} \tag{3.41}$$

or by using the quaternion method:

$$\hat{\boldsymbol{F}}_{AD,L} = \boldsymbol{q}_{L\leftarrow G} \otimes \begin{bmatrix} \hat{\boldsymbol{F}}_{AD,G} \\ 0 \end{bmatrix} \otimes \boldsymbol{q}_{L\leftarrow G}^{-1} \boldsymbol{q} \tag{3.42}$$

Finally the AD in the satellite frame is found by applying the rotation matrix from L to S:

$$\hat{\boldsymbol{F}}_{AD,S} = \boldsymbol{C}^{S/L} \hat{\boldsymbol{F}}_{AD,L} \tag{3.43}$$

or quaternion:

$$\hat{\boldsymbol{F}}_{AD,S} = \boldsymbol{q}_{S\leftarrow L} \otimes \begin{bmatrix} \hat{\boldsymbol{F}}_{AD,L} \\ 0 \end{bmatrix} \otimes \boldsymbol{q}_{S\leftarrow L}^{-1} \boldsymbol{q} \tag{3.44}$$

The torque produced by the atmospheric drag can be calculated by the cross product between the vector from the Center Of Mass (COM) to the Center Of Pressure (COP) and the net force produced by the atmospheric drag:

$$\boldsymbol{M}_{AD} = \boldsymbol{r}_{COP} \times \boldsymbol{F}_{AD} \tag{3.45}$$

3.8 Solar Radiation Pressure

Different from the influence the Sun has on the atmospheric drag mentioned in Section 3.7, the solar radiation itself also produces a small pressure, due to the momentum of the photons irradiation from the Sun. The magnitude of this momentum can be derived through Einstein's famous formula:

$$E = mc^2 \quad p = mv \quad \Rightarrow \quad p = \frac{E}{c} \tag{3.46}$$

Consequently the radiation exerts a small pressure, but still significant for precision controlled space flight. Its magnitude reads:

$$P = \frac{S}{c} \tag{3.47}$$

where S is solar energy flux at the spacecraft, and c is the speed of light. The SRP is naturally dependent on the distance to the sun. For a spacecraft in near-Earth orbit, where $S_E \approx 1367 W/m^2$, the resulting mean SRP reads approximately 4.56μPa [24]. However, the SRP on a surface element of area of a spacecraft is dependent on the reflective properties of that surface element. Hence, without specific knowledge on the surface characteristics, an approximation is necessary. One approach is to model the SRP by assuming the radiation is either absorbed, reflected by specular reflection or diffusive reflection or a combination of these. Consequently we look at these three separately. For the absorbed radiation force on a surface element of area $A(i)$ we have:

$$\boldsymbol{F}_{abs}(i) = PC_a \cos(\theta) \hat{\boldsymbol{F}}_{SRP,G} A(i) \tag{3.48}$$

where C_a is the absorption coefficient, θ is the angle between the normal vector of the surface element and the direction of the SRP denoted $\hat{\boldsymbol{F}}_{SRP,G}$.

For the specular reflection we have:

$$\boldsymbol{F}_{spec}(i) = 2PC_s \cos^2(\theta) \hat{\boldsymbol{n}} A(i) \tag{3.49}$$

where C_s is the specular reflection coefficient and $\hat{\boldsymbol{n}}$ is the normal vector of the surface element.

Finally for the diffusive reflection we have:

$$\boldsymbol{F}_{diff}(i) = PC_d \left(\frac{2}{3} \hat{\boldsymbol{n}} + \hat{\boldsymbol{F}}_{SRP,G} \right) \cos(\theta) A(i) \tag{3.50}$$

where C_d is the diffuse reflection coefficient. $\boldsymbol{F}_{abs}(i)$, $\boldsymbol{F}_{spec}(i)$ and $\boldsymbol{F}_{diff}(i)$ denotes the share of the radiation which is absorbed, reflected by specular reflection and reflected by diffuse reflection respectively. Hence, the three coefficients $C_a + C_s + C_d = 1$ [14].

The solar radiation pressure is present due to the light radiating outwards from the sun equally in all directions. Hence, the direction of the SRP towards the spacecraft can be found from subtracting the position vector of the sun $\boldsymbol{r_{sun}}$ from the position vector of the spacecraft $\boldsymbol{r}$, defined in the geocentric reference frame, as seen in Figure 3.11. However, what is interesting, is the direction of the SRP in the body frame of the spacecraft, in order for a control system to compensate for the

disturbance. Consequently, the direction of the SRP is ultimately transformed into the spacecraft frame. This is done by two successive coordinate transformations, as for the atmospheric drag.

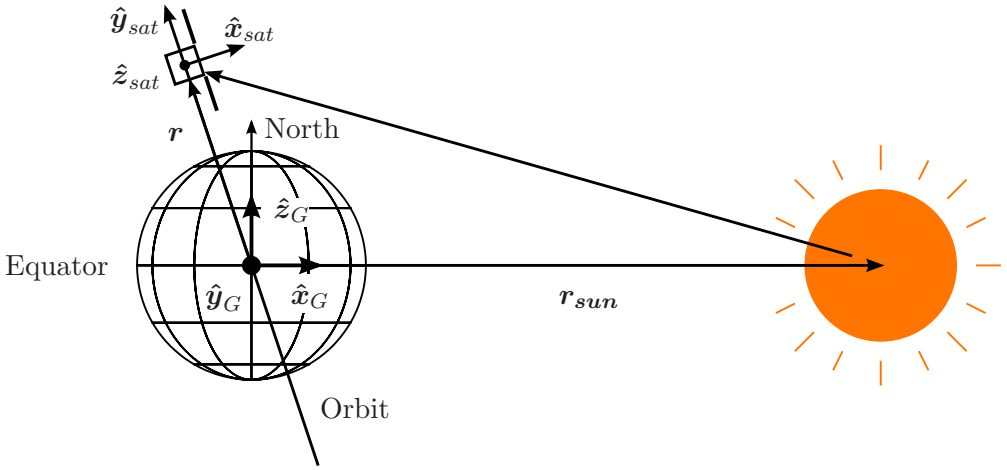

Figure 3.11: Incident direction of the SRP on a spacecraft in an orbit about the Earth is found as the difference between the position of the spacecraft and the position vector of the Sun.

With the definition of the geocentric frame stated earlier, the position vector of the sun in the geocentric frame is found by:

$$\begin{aligned} \boldsymbol{r_{sun}} &= r_{sun}\cos(\nu_E)\hat{\boldsymbol{x}}_G \\ &+ r_{sun}\sin(\nu_E)\cos(\epsilon)\hat{\boldsymbol{y}}_G \\ &+ r_{sun}\sin(\epsilon)\sin(\nu_E)\hat{\boldsymbol{z}}_G \end{aligned} \tag{3.51}$$

where ϵ is the tilt of the rotational axis of the Earth and ν_E is the true anomaly of the Earth. Here we have assumed that Earth has a perfect circular orbit, which is reasonable considering the large distance to the Sun compared to the distance to the satellite. Consequently, the direction of the SRP towards the spacecraft, is found by subtracting the position vector of the sun $\boldsymbol{r_{sun}}$ from the position vector of the spacecraft $\boldsymbol{r_M}$ and dividing the resultant vector by its modulus:

$$\hat{\boldsymbol{F}}_{SRP,G} = \frac{\boldsymbol{r}_M - \boldsymbol{r}_{sun}}{|\boldsymbol{r}_M - \boldsymbol{r}_{sun}|} \tag{3.52}$$

where $\boldsymbol{r_M}$ is calculated from the Kepler elements as in Equations 3.5 to 3.7. As for the atmospheric drag, two successive coordinate transformations are then applied.

First the SRP is transferred to the LVLH frame ($\hat{\boldsymbol{e}}_N$, $\hat{\boldsymbol{e}}_T$, $\hat{\boldsymbol{e}}_R$), by applying the rotation matrix from G to L:

$$\hat{\boldsymbol{F}}_{SRP,L} = \boldsymbol{C}^{L/G}\hat{\boldsymbol{F}}_{SRP,G} \tag{3.53}$$

And finally the SRP in the satellite frame is found by applying the rotation matrix from L to S:

$$\hat{\boldsymbol{F}}_{SRP,S} = \boldsymbol{C}^{S/L}\hat{\boldsymbol{F}}_{SRP,L} \tag{3.54}$$

3.9 Residual Magnetic Torque

Another disturbance is the residual magnetic torque, which is the torque produced by the interaction of the Earth's magnetic field and the satellite's residual magnetic field. Several factors will generate a residual magnetic field in the satellite, whether it is electrical currents in the wires or it is conducting material such as screws or the satellite frame etc. Any conducting material exposed to a changing magnetic field (e.g. a satellite orbiting the Earth) will create a current and therefore create a magnetic field. These currents are referred to as eddy currents. Even though it is almost impossible to remove all conducting material in a satellite, using material that is less conductive will significantly reduce the magnetic moment generated. For satellite construction any conductive or magnetized material where it is possible should be replaced with less conductive equivalents in order to reduce the torque generated.

3.10 The MICROSCOPE Mission

In the preceding sections we have seen which disturbances that are relevant to account for, when performing drag free flight and formation flying. We have discussed their sources and their magnitudes, but how they influence the dynamics of a spacecraft will be treated now for the MICROSCOPE mission specifically. Consequently, a model is derived, which shows how the direction and magnitude of the different disturbance forces evolves over time, for the MICROSCOPE spacecraft used as template.

The MICROSCOPE space mission is the first mission aiming at testing the equivalence principle to an accuracy of at least 10^{-15}. Hence, three-axis electrostatic accelerometers exhibiting ultra high sensitivities compatible with femto-g resolution are to be used as part of an AACS (Attitude and Acceleration Control Subsystem). Together with the other parts of this system, including a Micro ASC (Advanced Stellar Compass) - developed in our department - and a micropropulsion system, a highly accurate control system is realized - facilitating drag free flight. Hence, in the drag free flight mode called MCA (Accelerations Control Mode), the disturbance forces acting on the spacecraft are compensated by the micropropulsion system. Initially the micropropulsion system on the MICROSCOPE satellite was intended to be based of FEEP thrusters (Field Emission Electric Propulsion), but due to severe difficulties in implementing this technology, the team behind the mission has decided to use cold gas propulsion instead. This has increased the mass of the satellite with about 40 kg, which shows the relevance of this study and the continuing research within micropropulsion in general.

3.10.1 Frame Definition and Flight Modes of the MICROSCOPE

To derive the disturbances on the MICROSCOPE mission analytically, the orientation of the body frame of the spacecraft has to be known, as well as the flight modes of the satellite, defining the attitude and spin rates during the mission. The body frame is defined according to the geometry of the satellite as seen on Figure 3.12, where the spin direction also appears.

The LVLH frame L is rotated with respect to the geocentric frame G by the true anomaly, the inclination and the nodal regression angles: $\theta_x = \omega_M - \nu_M$, $\theta_y = \frac{\pi}{2} - i_M$, $\theta_z = \phi_M$. Hence, the rotation matrix from the geocentric frame to the LVLH frame reads:

$$\boldsymbol{C}^{L/G} = \begin{bmatrix} \mathrm{c}(\theta_y)\mathrm{c}(\theta_z) & \mathrm{c}(\theta_y)\mathrm{s}(\theta_z) & -\mathrm{s}(\theta_y) \\ \mathrm{s}(\theta_x)\mathrm{s}(\theta_y)\mathrm{c}(\theta_z) - \mathrm{c}(\theta_x)\mathrm{s}(\theta_z) & \mathrm{s}(\theta_x)\mathrm{s}(\theta_y)\mathrm{s}(\theta_z) + \mathrm{c}(\theta_x)\mathrm{c}(\theta_z) & \mathrm{s}(\theta_x)\mathrm{c}(\theta_y) \\ \mathrm{c}(\theta_x)\mathrm{s}(\theta_y)\mathrm{c}(\theta_z) + \mathrm{s}(\theta_x)\mathrm{s}(\theta_z) & \mathrm{c}(\theta_x)\mathrm{s}(\theta_y)\mathrm{s}(\theta_z) - \mathrm{s}(\theta_x)\mathrm{c}(\theta_z) & \mathrm{c}(\theta_x)\mathrm{c}(\theta_y) \end{bmatrix}$$

where $\mathrm{c}(\theta) = \cos(\theta)$. The rotation matrix from the LVLH frame to the satellite frame $\hat{\boldsymbol{x}}_{sat}$, $\hat{\boldsymbol{y}}_{sat}$, $\hat{\boldsymbol{z}}_{sat}$ is defined by the pitch, roll and yaw of the satellite, which

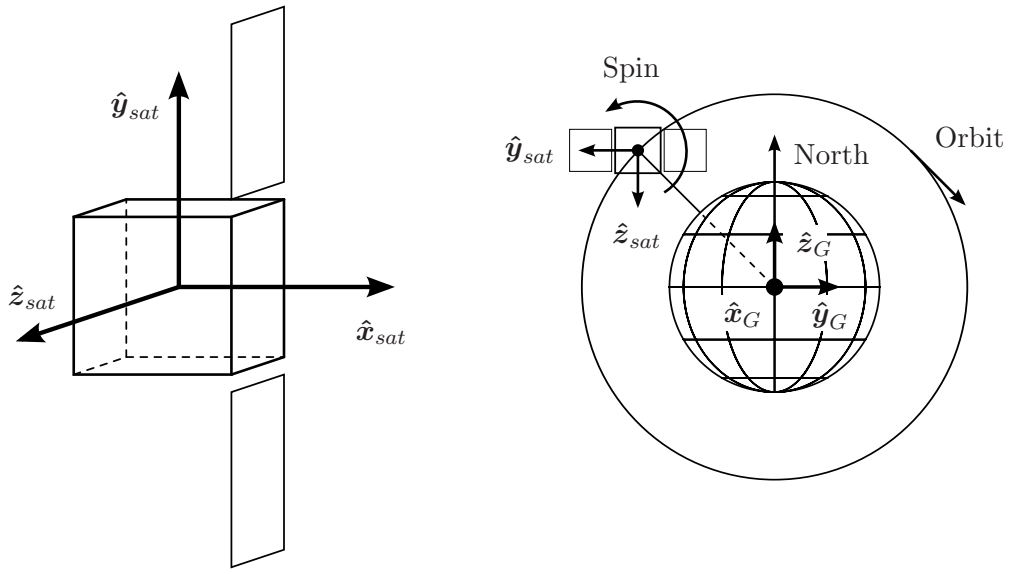

Figure 3.12: Definition of the body frame of MICROSCOPE. The satellite has a retrograde spin with its spin axis - the $\hat{\boldsymbol{x}}_{sat}$ axis - perpendicular to the orbit plane.

for MICROSCOPE are the rotations about the x-axis ψ_x, the y-axis ψ_y and the z-axis ψ_z respectively:

$$\boldsymbol{C}^{S/L} = \begin{bmatrix} \mathrm{c}(\psi_y)\mathrm{c}(\psi_z) & \mathrm{c}(\psi_y)\mathrm{s}(\psi_z) & -\mathrm{s}(\psi_y) \\ \mathrm{s}(\psi_x)\mathrm{s}(\psi_y)\mathrm{c}(\psi_z) - \mathrm{c}(\psi_x)\mathrm{s}(\psi_z) & \mathrm{s}(\psi_x)\mathrm{s}(\psi_y)\mathrm{s}(\psi_z) + \mathrm{c}(\psi_x)\mathrm{c}(\psi_z) & \mathrm{s}(\psi_x)\mathrm{c}(\psi_y) \\ \mathrm{c}(\psi_x)\mathrm{s}(\psi_y)\mathrm{c}(\psi_z) + \mathrm{s}(\psi_x)\mathrm{s}(\psi_z) & \mathrm{c}(\psi_x)\mathrm{s}(\psi_y)\mathrm{s}(\psi_z) - \mathrm{s}(\psi_x)\mathrm{c}(\psi_z) & \mathrm{c}(\psi_x)\mathrm{c}(\psi_y) \end{bmatrix}$$

Accelerations Control Mode (MCA) is the normal science mode of MICROSCOPE. The spacecraft slowly rotates about its x-axis, at a spin rate of the order of a few times the orbit rate. The spin is normal to the orbit plane, and provides the modulation of the EP signal which occurs at $\omega_{EP} = \omega_{spin} + \omega_{orb}$. Different spin rates will be used during the mission to repeat the experiment at different frequencies. Due to the retro-rotation w.r.t. the orbital motion, this spin increases the EP frequency ($\omega_{EP} = \omega_{spin} + \omega_{orb}$). Two main spin rates are foreseen:

1. $\omega_{spin} = 0$ in the inertial mode MCAi ($\omega_{EP} = \omega_{orb} \ \rightarrow \ f_{EP} = 1.7e-4$ Hz)
2. ω_{spin} is chosen close to $5\omega_{orb}$ in rotating mode MCAs ($\omega_{EP} = 6\omega_{orb} \ \rightarrow \ f_{EP} = 1e-3$ Hz)

Hence, in quasi-inertial mode MCAi, the spacecraft only follows the precession of the orbital plane. In rotating mode, the spacecraft rotates about 5 times per orbit about the x-axis (0.30 deg/s) in addition to the slow precession (lateral drift).

3.10.2 Sun Synchronous Dawn/Dusk Orbit

In order to obtain a nearly constant impact on the MICROSCOPE satellite from the solar radiation pressure and to maximize the power obtained from the solar panels, the intention is to put the satellite into a so called Sun Synchronous Dawn/Dusk orbit. Consequently the orbital plane has an inclination, which is chosen such that the nodal regression is kept at a rate of 360° per year (Sun Synchronous orbit). Furthermore the right ascension of the ascending node Ω, is chosen such that the line of nodes is perpendicular to the sun vector, i.e. the local mean solar time of passage for equatorial longitudes is around sunrise or sunset (Dawn/Dusk orbit). Consequently, from Equation 3.35 the inclination giving a Sun Synchronous orbit can be found:

$$\Delta\phi_2 = -\frac{3\pi J_2 R_E^2 \cos(i)}{a^2(1-e^2)^2} \text{ rad/orbit} \tag{3.55}$$

where $a = r$ and $e = 0$, since MICROSCOPE is to be put into a circular orbit. First we have to determine how many orbits MICROSCOPE will have in one year, since 3.55 is given in radians per orbit. This is done by determining the ratio between Earth's orbital period orbiting the sun and the orbital period of the MICROSCOPE satellite orbiting the Earth:

$$\begin{aligned} t_{Earth} &= 365.2422 \text{ days} \cdot 24 \text{ hours/day} \cdot 3600 \text{ sec/hour} \\ t_{Sat} &= 2\pi\sqrt{\frac{a^3}{\mu}} \\ n &= \frac{t_{Earth}}{t_{Sat}} \end{aligned}$$

where μ is the geocentric gravitational parameter. Since the number of orbits per year n, times the nodal regressing per orbit $\Delta\phi_2$ should be equal to 2π or 360° to obtain a Sun Synchronous orbit, we have:

$$\Delta\phi_2 = \frac{2\pi}{n} = 2\pi\frac{t_{Sat}}{t_{Earth}} = \frac{4\pi^2}{t_{Earth}}\sqrt{\frac{a^3}{\mu}} \tag{3.56}$$

Hence, by putting this into Equation 3.35 and then solve for the inclination i, we get:

$$\begin{aligned} \frac{4\pi^2}{t_{Earth}}\sqrt{\frac{a^3}{\mu}} &= -\frac{3\pi J_2 R_E^2 \cos(i)}{a^2(1-e^2)^2} \quad \Leftrightarrow \\ i &= \cos^{-1}\left(-\frac{4}{3}\sqrt{\frac{a^7}{\mu}}\frac{\pi(1-e^2)^2}{t_E J_2 R_E^2}\right) = 1.7142 \text{ rad} = 98.2165^\circ \end{aligned}$$

Which is exactly the inclination chosen for MICROSCOPE. Consequently, when we have vernal and autumnal equinox around the 20'th of march and the 22'nd of September, the angle between the $\hat{\boldsymbol{x}}_{sat}$ - which is the spin axis of MICROSCOPE - and the sun vector will be roughly $98.22^\circ - 90^\circ = 8.22^\circ$, and the satellite will never go into eclipse. When we have summer solstice around the 21'st of June, the angle will be $98.22^\circ - 90^\circ - 23.5^\circ = -15.28^\circ$ and the satellite will only with a small margin avoid eclipse. The only season where eclipse is unavoidable is the winter solstice around the 21'st of December. At this point the angle will be $98.22^\circ - 90^\circ + 23.5^\circ = 31.72^\circ$.

3.10.3 Atmospheric Drag on MICROSCOPE

For MICROSCOPE we will denote its parameters by subscript M. Hence, the position vector of MICROSCOPE is denoted $\boldsymbol{r}_M$. As stated in Equation 3.39, the direction of the atmospheric drag can be found from the time derivative of the position vector of the spacecraft. When the position is known for a certain number of timestamps, this translates into:

$$\hat{\boldsymbol{F}}_{AD,G} = -\hat{\boldsymbol{v}}_M = -\frac{d\boldsymbol{r}_M}{dt}\frac{1}{v_M} \approx -\frac{\boldsymbol{r}_M(i+1) - \boldsymbol{r}_M(i)}{t(i+1) - t(i)}\frac{1}{v_M} \tag{3.57}$$

where $\boldsymbol{r}_M$ is given by Equations 3.5, 3.6 and 3.7:

$$x_M = r_M(\cos(\Omega_M)\cos(\omega_M+\nu_M) - \sin(\Omega_M)\sin(\omega_M+\nu_M)\cos(i_M)) \quad (3.58)$$
$$y_M = r_M(\sin(\Omega_M)\cos(\omega_M+\nu_M) + \cos(\Omega_M)\sin(\omega_M+\nu_M)\cos(i_M)) \quad (3.59)$$
$$z_m = r_M \sin(i_M)\sin(\omega_M+\nu_M) \quad (3.60)$$

The distance r_M to the spacecraft we determine from:

$$r_M = \frac{a_M(1-e_M^2)}{1+e_M cos(\nu_M)} \quad (3.61)$$

where e_M and a_M are the eccentricity and the semimajor axis respectively, of the orbit of the MICROSCOPE satellite. As discussed earlier, the true anomaly ν_M can be determined from the mean anomaly M_M, which we will calculate from the orbital period T_M and the duration t of the flight:

$$T_M = 2\pi\sqrt{\frac{a_M^3}{\mu}} \quad \rightarrow \quad M_M = \frac{2\pi}{T_M}\cdot t \quad (3.62)$$

where μ is the gravitational parameter for Earth. For a perfect circular orbit, the mean anomaly and the true anomaly becomes equal, and consequently for the MICROSCOPE satellite it is not necessary to calculate the true anomaly. However we do it anyway to get a more generally applicable model, by solving Equation 3.2 numerically.

In order to calculate the magnitude of the atmospheric drag, initially we look up the density ρ of the atmosphere in the table provided by the MSISE-90 Model of Earth's Upper Atmosphere. The table contains the density vs. altitude for high, mean and low solar activity. Here we use the high solar activity to get a worst case, and calculate the altitude in kilometers by:

$$alt_M = \frac{r_M - R_E}{1000} \quad (3.63)$$

where R_E is the mean radius of the Earth. Since the body of the MICROSCOPE spacecraft is almost a cube (neglecting the solar panels) and two faces of this cube is always parallel to the drag vector while the spacecraft is spinning, the drag coefficient C_D will vary between $C_\square = 1.05$ and $C_\diamond = 0.80$ for a cube and an angled cube respectively, as seen on Figure 3.10. Consequently, when the pitch

of the satellite is $\psi_x = n\frac{\pi}{2}$ $(n = 1, 2, 3...)$ the drag coefficient is 1.05 and when $\psi_x = n\frac{\pi}{2} + \frac{\pi}{4}$ it is 0.80. Accordingly a good approximation to the drag coefficient as function of the pitch, is constructed by:

$$C_D(\psi_x) = \frac{C_\square - C_\diamond}{2}\cos(4\psi_x) + \frac{C_\square + C_\diamond}{2} \tag{3.64}$$

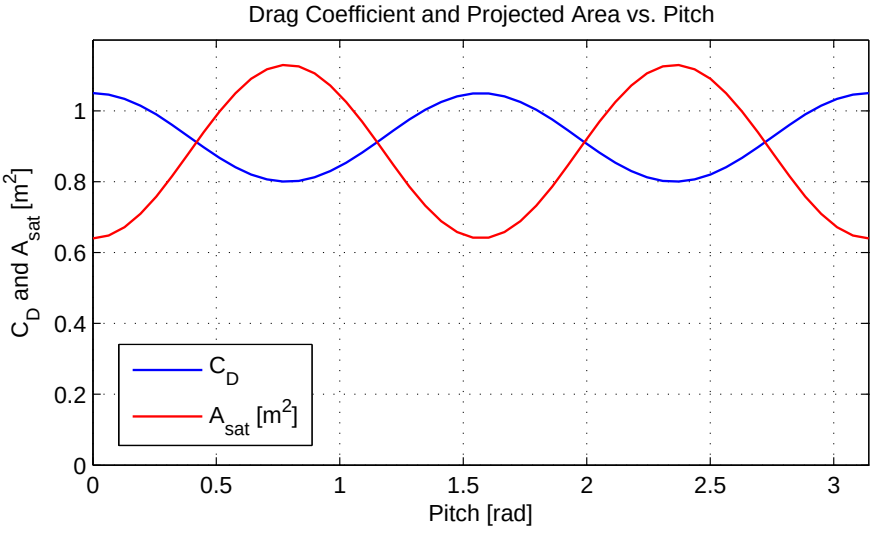

Figure 3.13: Drag coefficient and projected area - MICROSCOPE. As the projected area reaches its maximum, the drag coefficient reaches its minimum, thus reducing the influence of the two.

For simplification we refrain from determining the atmospheric drag on every surface element of the spacecraft separately. Instead we use the projected area. As mentioned in Section 3.7, the projected area also changes as the spacecraft is spinning and in a similar manner to the drag coefficient, we can make an approximation to the changing projected area. The dimensions of the body of MICROSCOPE is roughly $x \times y \times z = 0.8\text{m} \times 0.8\text{m} \times 0.8\text{m}$. Hence, when $\psi_x = n\frac{\pi}{2}$ the projected area reads $A_{sat} = x \times z = 0.64\text{m}^2$ and for $\psi_x = n\frac{\pi}{2} + \frac{\pi}{4}$ its is $A_{sat} = x \times \sqrt{y^2 + z^2} = 1.13\text{m}^2$. As for the drag coefficient we then have:

$$A_{sat}(\psi_x) = \frac{A_\square - A_\diamond}{2}\cos(4\psi_x) + \frac{A_\square + A_\diamond}{2} \tag{3.65}$$

On Figure 3.13 the variation of the drag coefficient and projected area vs. the pitch angle is seen. The two are out of phase, which reduces their impact on the net drag force. Recalling Equation 3.38 the AD is found by:

$$\boldsymbol{F}_{AD} = -\frac{1}{2}\rho C_D v_M^2 \hat{\boldsymbol{v}}_M A_{sat} \tag{3.66}$$

when the projected area is utilized. For the speed v_M of the satellite, one can either use:

$$v_M = \sqrt{\frac{2\mu}{r_M} - \frac{\mu}{a_M}} \quad \text{or} \quad v_M = \left| \frac{\boldsymbol{r}_M(i+1) - \boldsymbol{r}_M(i)}{t(i+1) - t(i)} \right| \tag{3.67}$$

For the coordinate transformations we use the faster quaternion method. First to L (LVLH frame) from G (geocentric frame):

$$\hat{\boldsymbol{F}}_{AD,L} = \boldsymbol{q}_{L\leftarrow G} \otimes \begin{bmatrix} \hat{\boldsymbol{F}}_{AD,G} \\ 0 \end{bmatrix} \otimes \boldsymbol{q}_{L\leftarrow G}^{-1} \boldsymbol{q} \tag{3.68}$$

then to S (MICROSCOPE body frame) from L:

$$\hat{\boldsymbol{F}}_{AD,S} = \boldsymbol{q}_{S\leftarrow L} \otimes \begin{bmatrix} \hat{\boldsymbol{F}}_{AD,L} \\ 0 \end{bmatrix} \otimes \boldsymbol{q}_{S\leftarrow L}^{-1} \boldsymbol{q} \tag{3.69}$$

The most critical flight mode of MICROSCOPE, regarding the impact of the AD, is the MCAs, where the satellite spins at a rate of 6 times the orbit frequency about the x_{sat} axis, which is perpendicular to the AD vector. For this flight mode the AD on the MICROSCOPE satellite is plotted for low, mean and high solar activity for a duration of one half orbit (2900 s) in the Figures 3.14, 3.15 and 3.16 respectively. On Figure 3.16, which represents the worst case, it is readable from the graphs that the small variations in the AD due to the changes in drag coefficient and projected area, give a rate of change of $\approx 10\mu$N/min for the y_{sat} and z_{sat} directions. The largest rate occurs as the thrusters need to shut off due to the spin of the satellite. Here the AD changes with a rate of $\approx 40\mu$N/min.

The modelling is done in Matlab, following the sequence:

1. Loading physical constants and the MSISE-90 Model of the atmospheric density
2. Collecting the orbital elements of the spacecraft and spin rates about the three axes roll, yaw and pitch
3. Calculation of velocity and altitude from the orbital elements
4. Attitude determination from duration of the flight and spin rates

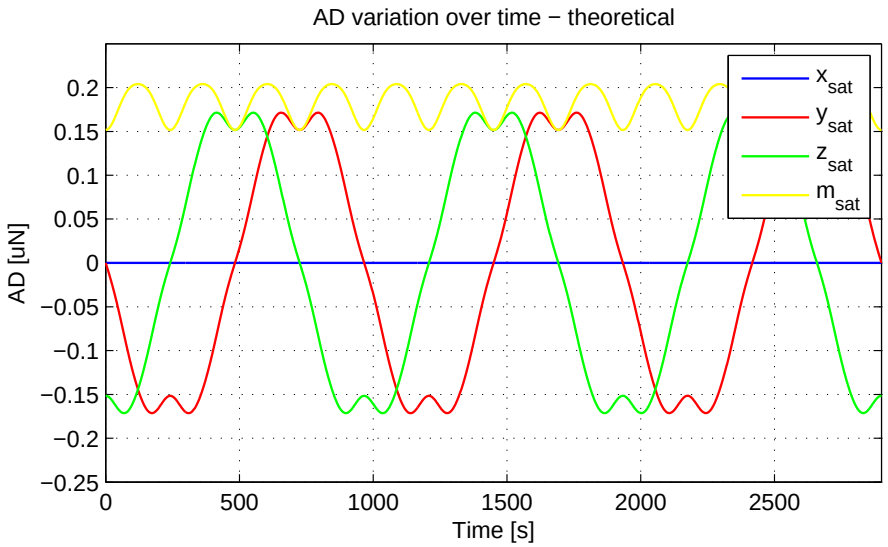

Figure 3.14: The three components of the Atmospheric drag on MICROSCOPE at low solar activity, including the magnitude m_{sat}

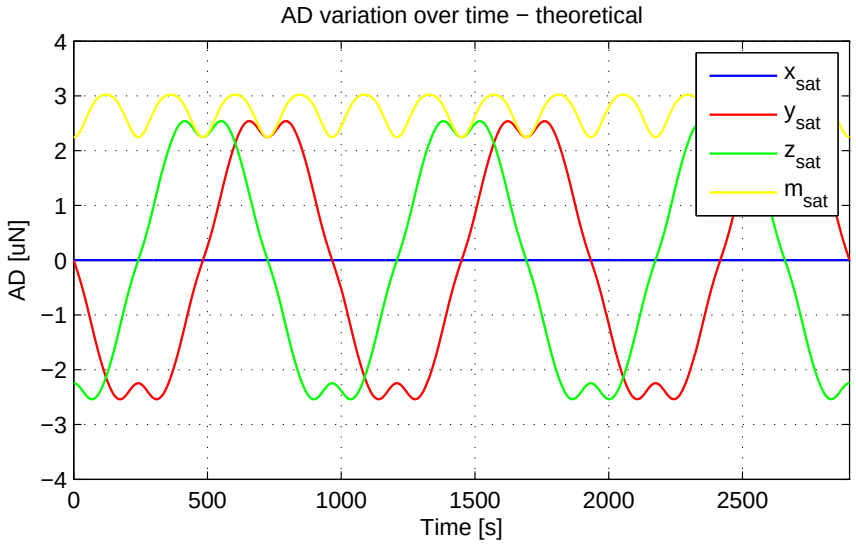

Figure 3.15: The three components of the Atmospheric drag on MICROSCOPE at mean solar activity, including the magnitude m_{sat}

5. Collecting the present atmospheric density from the MSISE-90 Model using the calculated altitude

6. Determining the incident direction of the atmospheric drag from the velocity

7. Calculation of the drag coefficient and projected area on the basis of the attitude

8. Calculation of the magnitude of the atmopheric drag

9. Coordinate tranformation to the spacecraft frame

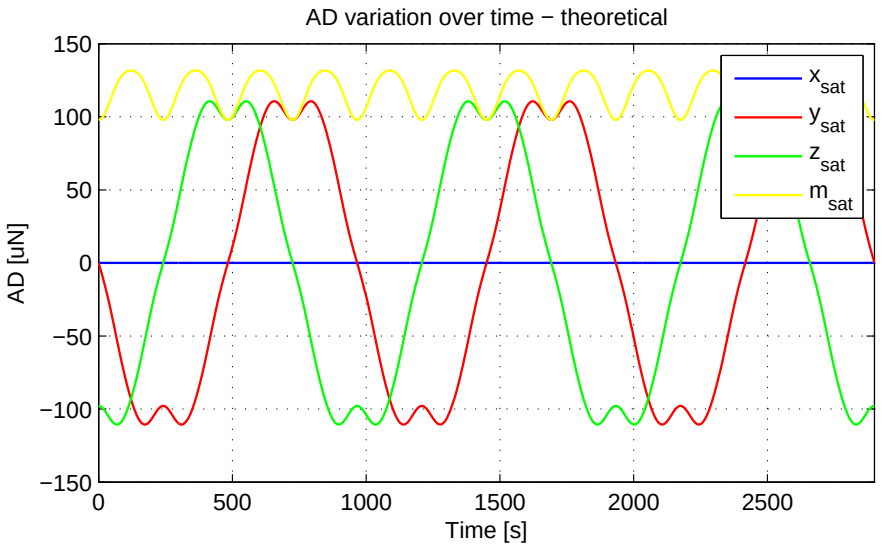

Figure 3.16: The three components of the Atmospheric drag on MICROSCOPE at high solar activity, including the magnitude m_{sat}

3.10.4 Solar Radiation Pressure on MICROSCOPE

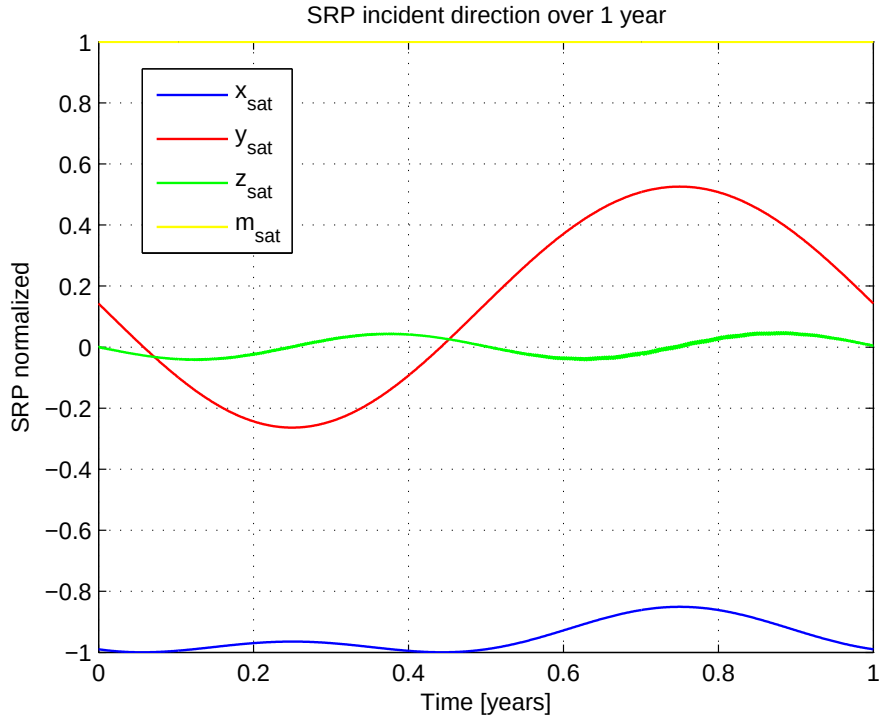

Figure 3.17: Incident direction of the SRP in the spacecraft frame of MICROSCOPE plotted for a duration of one year, starting at vernal equinox.

For MICROSCOPE the incident direction of the SRP in the spacecraft frame is plotted in Figure 3.17 for a duration of one year, assuming no spin of the satellite other than the spin following the nodal regression. Since the orbit of

MICROSCOPE is sun synchronous, this plot will be periodic with a period of one year.

For calculating the SRP on a spacecraft like MICROSCOPE, the critical parameters are of course the illuminated area, but also the coefficients determining the fraction of absorbed, specular reflected and diffusely reflected radiation. Unfortunately we only roughly know the dimensions of MICROSCOPE, and for the SRP coefficients we have to make some assumptions. As the spacecraft is always turning its solar panels towards the sun, with an angle varying slowly from $-15.28°$ to $31.72°$ from summer to winter, the time constant / rate of change on the SRP will be very small and neglectable compared to the atmospheric drag on MICROSCOPE, as seen on Figure 3.18. However, as the satellite goes into eclipse and when it leaves, the SRP will rise and fall over a very short instance, due to the high speed of the satellite. Since this only happens for MICROSCOPE around winter solstice, CNES has decided not to conduct experiments around this period, and consequently there is no need to consider this situation.

Consequently, we only consider the magnitude of the SRP. Since we lack information about the radiation coefficients, we consider the worst case scenario, where the radiation is incident perpendicularly to the exposed surfaces and all the radiation is reflected, entirely by specular reflection. The radiation coefficients then reads: $C_a = 0$, $C_s = 1$ and $C_d = 0$. In this scenario the exposed surfaces will be only the front face A_f of the satellite body and the solar panels $2 \times A_s$ as seen on Figure 3.19. Accordingly, the SRP is simplified to:

$$\begin{aligned} \boldsymbol{F}_{SRP,M} &= \sum_{1}^{n} \boldsymbol{F}_{spec}(i) = \sum_{1}^{3} 2PC_s(i)\cos^2(\theta)\hat{\boldsymbol{n}}A(i) = 2P\hat{\boldsymbol{x}}_{sat}(2A_s + A_f) \\ &= 2 \cdot 4.56\mu\text{Pa}(2 \cdot 1.1\text{m} \cdot 0.7\text{m} + 0.8\text{m} \cdot 0.8\text{m})\hat{\boldsymbol{x}}_{sat} = 20\mu\text{N}\hat{\boldsymbol{x}}_{sat} \end{aligned}$$

That is, at low and mean solar activity, where the density of the atmosphere is fairly low, the SRP can actually become the most significant disturbance for MICROSCOPE.

The model of the SRP derived in this project, is made for a generalized spacecraft in Matlab, following a sequence originating in the derivation from Section 3.8:

1. Loading physical constants and reflective characteristics of the spacecraft

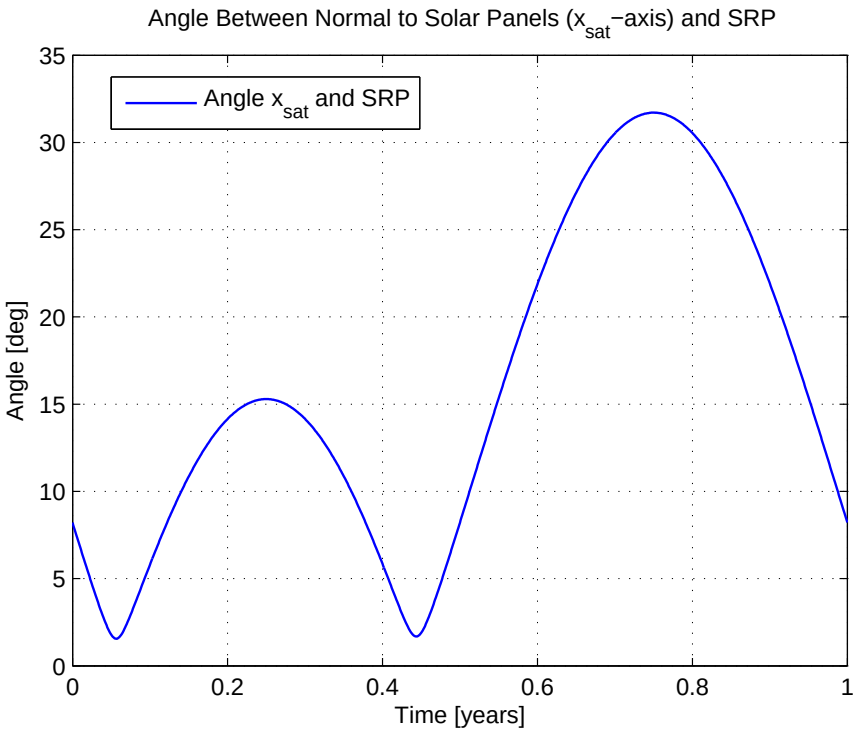

Figure 3.18: Angle between SRP and the x-axis of MICROSCOPE

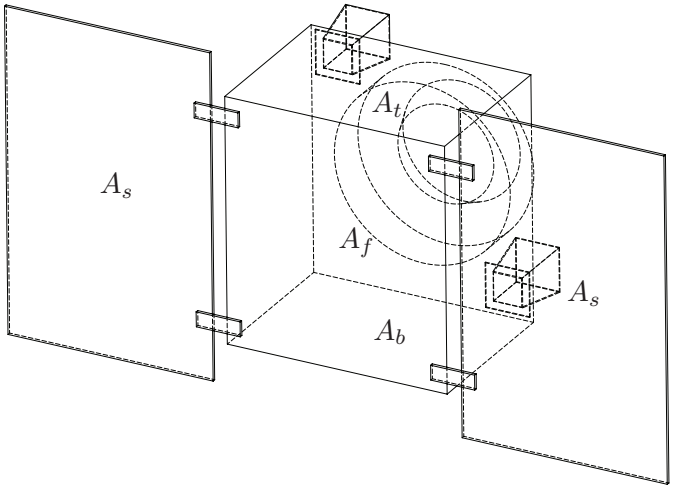

Figure 3.19: Surfaces exposed to the sun on the MICROSCOPE satellite.

2. Collecting the orbital elements of the spacecraft and spin rates about the three axes roll, yaw and pitch
3. Calculation of position and nodal regression from the orbital elements
4. Attitude determination from duration of the flight and spin rates
5. Determining the incident direction of the SRP from the position vector and the sun vector
6. Calculation of the magnitude of the SRP on the individual surface elements
7. Coordinate transformation to the spacecraft frame

3.11 Summary

Summing up this chapter, the math and physics needed to derive a model for some of the most important disturbances on a precision controlled spacecraft has been presented. Using this, some of the requirements for a micropropulsion system, designed to compensate for the disturbances consisting of atmospheric drag and solar radiation pressure, was deduced for the MICROSCOPE mission. Looking at the required performance of a micropropulsion system, which can fulfill the demands of the MICROSCOPE mission, the most critical factor towards start up and shut off characteristics turned out to be the atmospheric drag, with a rate of change of up to ≈ 40 μN/min. Also on the magnitude of the drag, the atmospheric disturbance - with a maximum value of ≈ 130 μN - could by far become the most significant factor compared to the solar radiation, when a high solar activity heats up the atmosphere and consequently increases the density. However, in normal space weather conditions, the solar radiation pressure - with a maximum value of ≈ 20 μN - exceeds the atmospheric drag, lying around 3 μN at mean solar activity.

Finally the restriction on the acceleration noise on the MICROSCOPE mission is justified by the range of the accelerometers: 1 $\mu\text{N}/\sqrt{\text{Hz}}$ from 0.1 Hz to 10 Hz. The residual acceleration requirements are 10^{-12} $\text{m/s}^2/\sqrt{\text{Hz}}$ (harmonic signals) and $3 \cdot 10^{-10}$ $\text{m/s}^2/\sqrt{\text{Hz}}$ (stochastic signals) at f_{EP}. Obviously it is very difficult to accurately predict the disturbances discussed here, and consequently micropropulsion systems are almost never used in open loop. They work into a very tight closed loop, which imposes a quick response time (otherwise they become instable). The response time (rise or fall for a small step of command) required on the MICROSCOPE is 250 ms.

Chapter 4

Sensor Techniques and Propulsion Principles

In the search for means to eliminate - or at least minimize - the impact of the disturbances described in the preceding chapter, we investigate in this chapter different sensor techniques for measuring the disturbances and the principles of propulsion serving as candidates for a micropropulsion system capable of compensating for the disturbances.

4.1 Sensor Techniques

For realizing a formation flying space mission, both attitude and relative position of the spacecrafts is measured. However, for single spacecraft drag free missions the attitude and acceleration of the spacecraft can be sufficient in order to actuate the thrusters according to the disturbances. In this section we go through a number of sensor techniques, suitable for constituting the sensor part of a control system for precision controlled space flight.

4.1.1 Star trackers and the Visual Based System

The most accurate and probably the most utilized method for determining the attitude of spacecrafts, is the use of stellar compasses / star trackers. Star trackers determines the attitude of a spacecraft on the basis of images acquired of the present star constellation within the field of view of its camera head unit. The Visual Based System (VBS) is an instrument developed by DTU Space based on

the highly successful microASC platform, a fully autonomous high accuracy star tracker platform that is used worldwide as a high performance attitude recovery instrument on board satellites. The standard microASC can drive from 1 to 4 CHUs, so as to provide continuous attitude information for even the most demanding space mission. The microASC platform, and its attitude performance, is fully space qualified, and at present it has been delivered to more than 20 satellites worldwide [19].

The purpose of the VBS is to visually determine the relative position and attitude between spacecrafts flying in close formation or vehicles performing rendezvous and docking. The VBS is currently flying on the Swedish technology demonstration mission PRISMA, which consists of two spacecrafts - a target satellite without control system and a main satellite with full control on all six degrees of freedom. On this mission the VBS has shown an extremely high position accuracy: at a 5 meter distance - 0.1 mm laterally and 0.5 mm on the distance. The typical direction accuracy is 3 arc seconds that corresponds to a 30 m diameter uncertainty circle at 1000km.

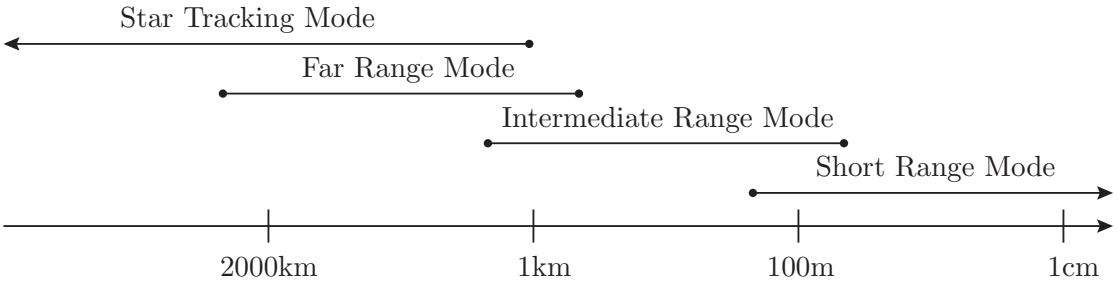

Figure 4.1: Modes of the VBS system and the ranges of operation [19].

The VBS has four different modes of operations; far range, intermediate range, short range cooperative and short range non-cooperative. The latter two modes, is implemented to enable formation flying, both when the target satellite is trying to help the navigation and when it is not. The mode switching diagram is shown in Figure 4.1. On the PRISMA mission the target satellite is helping the navigation in cooperative mode by flashing its dedicated infrared LED's, which is recognized by the VBS on the main satellite.

- **Attitude Mode.** The VBS DPU uses solely the standard CHU for attitude solutions.
- **Far range VBS mode.** The VBS DPU uses the standard CHU for searching and tracking target candidates, in ranges from 10,000 km down to 1 km.

Intermediate range VBS mode. The VBS DPU uses the standard CHU to obtain the target direction and distance. Range: 5 km down to 200 m.

- **Short range VBS mode non-cooperative.** The VBS DPU uses the standard CHU to obtain the target direction, distance and pose. Range: 200 down to 20 m.
- **Short range VBS mode cooperative.** The VBS DPU uses the NIR (Near InfraRed) CHU to obtain the target direction, distance and pose. Range: 100 down to 0.1 m.

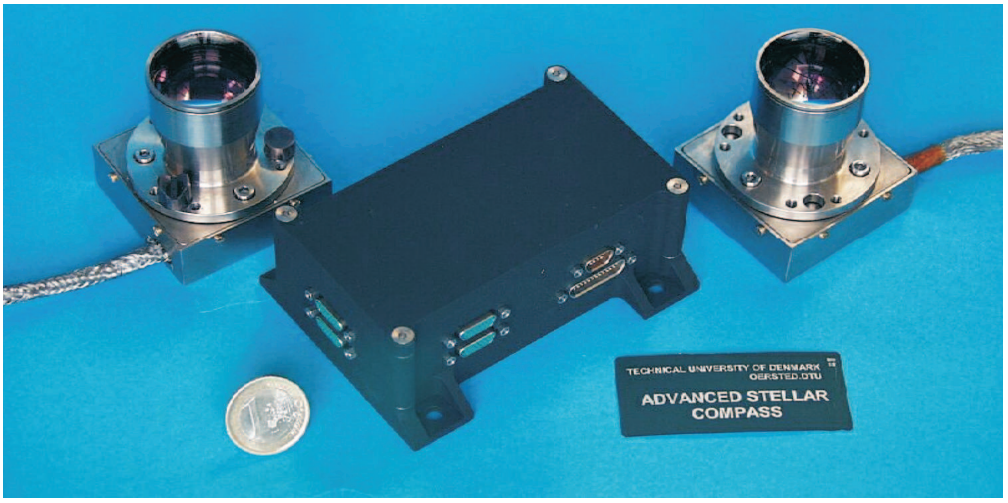

Figure 4.2: The microASC DPU with 2 CHU's. The microASC can run up to 4 CHU's and is the platform upon which the VBS system is build.

4.1.2 GPS and FFRF

Other examples of sensors for formation flight is the GPS system provided by the DLR and the FFRF (Formation Flying Radio Frequency) system provided by CNES. These systems has also been tested on the PRISMA mission.

The GPS system Phoenix is a twelve channel single-frequency GPS receiver based on a commercial-off-the-shelf hardware platform and qualified by DLR for use in low Earth orbit (LEO). The receiver is built around the GP4020 baseband processor of Zarlink, which combines the correlator, a microcontroller core with a 32 bit ARM7TDMI microprocessor and several peripheral functions in a single package. Phoenix provides a code tracking accuracy of better than 0.5 m and a carrier-phase accuracy of better than 1 mm at 45 dB-Hz. With a mass of the receiver board of 20 gr, a size of 70 x 47 x 15 mm and a power consumption of 0.85

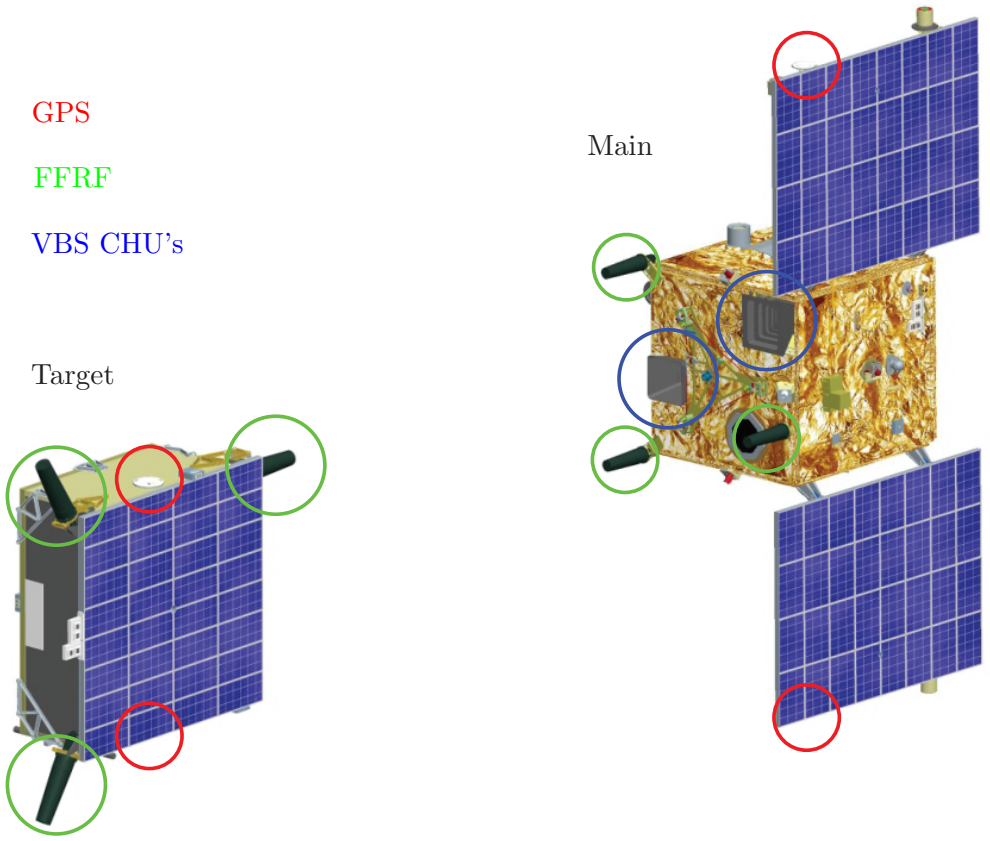

Figure 4.3: PRISMA Satellites. Placement of the 3 formation flying sensors/antennas.

W at begin of life, the receiver is particularly suited for small satellite missions like PRISMA [21].

As partner on the PRISMA mission, CNES participates with the experiment FFIORD, Formation Flying In-orbit Ranging Demonstration, consisting of the delivery of the RF metrology instrument (FFRF), and GNC software implemented on the Mango satellite. The FFRF subsystem can handle coarse relative positioning of 2 to 4 satellites. It produces relative position, velocity and line-of-sight (LOS) as inputs to the GNC subsystem for which it provides coarse metrology measurements. On PRISMA, MAIN is equipped with a triplet (1 Rx/Tx master and 2 Rx slaves) and TARGET is fitted with 3 single Rx/Tx antennas for omni-directional coverage. Ranging and angular measurements are extracted from received signals and are used for computing relative position (1 cm accuracy), velocity and LOS (1° accuracy) [21].

4.1.3 Accelerometers

An electrostatic accelerometer consists, fundamentally, of a PM (Proof Mass) suspended in a highly stable electrode cage. The principle of operation is to measure the electrostatic forces required from the electrodes to maintain the position of the PM with respect to the cage. Because the suspended proof mass of a perfect sensor is susceptible only to gravitational forces and the electrostatic forces applied by the electrode cage, the force applied is proportional to the difference between the total acceleration of the cage and the gravitational acceleration of the PM.

The concept of the three-axis electrostatic accelerometers based on the full electrostatic suspension of one unique PM is very suitable for space applications requiring very high resolution of acceleration measurement or drag-free control of satellites. This concept has been tested in orbit with the accelerometer CACTUS from ONERA in the late seventies and recently with the accelerometer ASTRE on board Columbia shuttle in June 1996. The accelerometer outputs are derived from the measurement of the electrostatic forces, necessary to maintain the mass motionless at the center of the accelerometer cage. The relative test-mass position and attitude are servo-controlled from measurements of capacitive sensors exhibiting resolutions of better than $10^{-10}\mathrm{m}/\sqrt{\mathrm{Hz}}$ depending on the geometrical configuration.

The test of the weak equivalence principle can be performed in orbit on board a drag-free satellite with two concentric electrostatic accelerometers including two cylindrical test masses made of different materials. The measured common acceleration is controlled to null along the three directions by the drag compensation system of the satellite. The differential acceleration is detected at the orbital frequency (or around the satellite spin frequency) along the common revolution axis [20].

4.2 Propulsion Principles

Rocket propulsion is an issue which is simple to understand but can be quite difficult to solve. Consequently the phrase "Its not exactly Rocket Science" came along, as the whole world observed how great nations like The Soviet Union and The United States kept failing over and over again in their struggle to fight gravity. Where they had the problem of controlling those massive forces needed to escape Earth's gravity, we are aiming for controlling minute forces. However the basic issue is the same.

4.2.1 Rocket Science

Basically what "Rocket Science" is all about, is to study methods for changing the relative linear - or for attitude control - angular momentum of an object of a certain mass and consequently inertia. Hence, the inertia is what all rocket scientists are fighting against, since this is the resistance a body exhibits against acceleration. Furthermore, in case the body of interest is in the vicinity of another body - such as the earth or the sun - we have to fight not only the inertia but also the gravitation. A situation where this is very apparent, is when trying to escape the gravitation of a planet, as experienced and followed with great attention during the space race. In this situation the energy content per mass unit of the rocket fuel can become a critical factor, since increasing the amount of fuel loaded on the rocket not only increases the inertia but also the gravitational pull.

Until now, the only known way of changing the momentum of an object, is by applying the consequences of Newton's laws of motion. The 3'rd law states: To every action there is always an equal and opposite reaction. A consequence of this law is that if one object exerts a force on another object, it will experience a force of equal magnitude but of exactly the opposite direction. The magnitudes of their accelerations however, might not be the same for the two objects. This is due to the effect of Newton's 2'nd law, stating that the acceleration of a body is in the same direction and proportional to, the net force acting on the body. The proportionality factor is $1/m$, where m is the mass of the body, and consequently the accelerations of the two objects are only equal in magnitude in the case that they have equal masses.

This means that if we say the object exerting the force is a rocket with mass m including fuel, and the object being affected by the force is an amount of fuel Δm loaded on the rocket, then the rocket will experience a force in the opposite direction with a magnitude of $F = \Delta m a_f$, where a_f is the acceleration of the fuel. This force is also equal to $F = (m - \Delta m)a_r$, where a_r is the acceleration of the rocket, thus found by:

$$a_r = \frac{\Delta m}{m - \Delta m} a_f \tag{4.1}$$

Since the fuel Δm eventually leaves the rocket, it reaches a top speed we call the exhaust velocity v_e. Consequently, more fuel is needed to keep accelerating the rocket, and thus the exhaust velocity becomes the dominant factor determining how effectively the rocket uses the fuel.

Assume the rocket engine is fired for a time Δt and the fuel is ejected with a constant mass flow and a constant exhaust velocity. If the velocity of the rocket before the burn was v_r, the velocity after the burn is $v_r + \Delta v_r$ and the mass of the rocket is reduced to $m - \Delta m$. Due to the principle of conservation of momentum, the total momentum before the burn has to be equal to the total momentum after the burn. Hence, similarly to Equation 4.1 we can write for the duration Δt of the burn:

$$\begin{aligned}
\frac{p_{r(1)}}{\Delta t} &= \frac{p_{r(2)}}{\Delta t} + \frac{p_{f(2)}}{\Delta t} \quad \Rightarrow \\
\frac{mv_r}{\Delta t} &= \frac{(m-\Delta m)(v_r+\Delta v_r)}{\Delta t} + \frac{\Delta m v_f}{\Delta t} \quad \Leftrightarrow \\
\frac{mv_r}{\Delta t} &= \frac{m(v_r+\Delta v_r)}{\Delta t} - \frac{\Delta m(v_r+\Delta v_r)}{\Delta t} + \frac{\Delta m v_f}{\Delta t} \quad \Leftrightarrow \\
\frac{mv_r}{\Delta t} &= \frac{mv_r}{\Delta t} + \frac{m\Delta v_r}{\Delta t} - \frac{\Delta m(v_r+\Delta v_r)}{\Delta t} + \frac{\Delta m v_f}{\Delta t} \quad \Leftrightarrow \\
m\frac{\Delta v_r}{\Delta t} &= \frac{\Delta m}{\Delta t}((v_r+\Delta v_r) - v_f)
\end{aligned} \tag{4.2}$$

Letting Δt approach zero, we have $\Delta v_r/\Delta t \rightarrow dv_r/dt = a_r$ and $\Delta m/\Delta t \rightarrow -dm/dt = -\dot{m}$ as the change in mass of the body with time, is negative in this case. And since the term $v_f - (v_r + \Delta v_r)$ is actually the exhaust velocity, Equation 4.2 simply becomes:

$$ma_r = \dot{m}v_e \tag{4.3}$$

Hence, to maximize the thrust, the rocket should have a maximized mass flow of fuel $\dot{m}$ and expel the fuel at the highest possible speed v_e. The force $F = ma_r$ is called the thrust of the rocket and is measured normally in Newtons, but also sometimes in Kilograms or Pounds. However, for a rocket where the mass flow is provided by a heated gas expanding through the diverging part of a nozzle, the full thrust equation reads:

$$F = \dot{m}v_e + (P_e - P_a)A_e \tag{4.4}$$

This is due to the fact that a complete expansion of the gas is never achievable in space, since this would require an almost infinitely long nozzle. Hence, the ambient pressure P_a will always be somewhat lower than the pressure P_e at the very end of the nozzle. Thus, the extra thrust $F_p = (P_e - P_a)A_e$ provided by this

pressure difference must be added, where A_e denotes the area of the nozzle exit. The fuel efficiency is normally quantified by the I_{sp} - specific impulse, which is basically a measure of the exhaust velocity. This quantity is normally given in seconds, being the time the thruster will burn while delivering a thrust equal to the initial weight of its fuel, and is thus calculated by:

$$I_{sp} = \frac{F}{\dot{m} \cdot g} \tag{4.5}$$

where g is the acceleration due to gravity at the surface of the Earth.

4.2.2 Chemical Rockets/Thrusters

To generate the necessary kinetic energy the fuel of a thruster has when it leaves the nozzle, a combustion process is used in chemical rockets. The combustion process takes place in a combustion chamber connected to a converging diverging nozzle, which converts the chemical-thermal energy into kinetic energy. Burning of chemical propellants at high pressure provides a relatively high release of energy - providing a high specific impulse, as seen in Table 4.1 - and so far this principle has shown to be very useful in high thrust applications. Since the thruster should function in space where no oxygen is present in any ambient atmosphere, both fuel and oxidizer must be carried on board the spacecraft. Mono-propellant fuels exists however, where both oxidizer and propellant is chemically bound in the same material. These are often used in solid state thrusters, where it can be difficult to proportion the amount of oxidizer. If the fuel is solid and the oxidizer is carried in its liquid state, it is called a hybrid rocket.

Fuel	Oxidizer	Combustion Temp. [K]	Specific Impulse [s]
Hydrogen	Oxygen	2980	390
Hydrogen	Flourine	4117	410
Hydrazine	Oxygen	3410	313
Hydrazine	Nitric Acid	2967	278
Hydrazine	Monopropellant	966	199
Hydrogen Peroxide	Monopropellant	1267	165

Table 4.1: Chemical Thrusters: Specific impulse for different types of propellant [26].

The disadvantage considering chemical combustion for low thrust applications, is the high release of energy in a combustion process, meaning that extremely small impulse bits are necessary. Furthermore, proportioning the oxidizer

and fuel in the right amounts for a proper combustion to take place, is hard when such small amounts must be used. This is due to the difficulties constructing tiny fully controllable pumps. Small amounts of liquids can be transported by capillary pumps working due to capillary forces, which can be constructed relatively easy as tiny tubes where the capillary forces are predominant. But the study performed in the project has shown that controlling the behavior of capillary flow can be very hard, so making the liquids for a chemical combustion flow, mix and burn in the desired manner is regarded as very difficult.

4.2.3 Resistojets

Similarly to chemical thrusters, resistojets also uses heat to produce a high pressure in a chamber to accelerate a gas through a nozzle. In a resistojet however, the heat is not generated by combustion, but by an electrical resistor, which makes resistojets one of many types of Electric Propulsion (EP). Since the thrust is controlled electrically, resistojets has an advantage when small corrections on the thrust is required. Generally resistojets do well in situations where electric energy is much more plentiful than mass, fuel efficiency is not a primary concern and low-thrust is acceptable. Resistojets are divided into two categories: thrusters fueled by gases and liquid fueled thrusters. Often the fuel is some non-reactive fluid, but can also work with hydrazine mono-propellant, which makes resistojets particularly attractive because they readily lend themselves to integration with previously developed and commonly used propellant storage systems for hydrazine mono-propellant chemical thrusters.

Another advantage is their low operational voltage, which, unlike that in other EP systems, does not require complex power processing. The principle is simple, reliable and can make use of a wide range of fuels including harmless fuels like water and ethanol. The disadvantages are a high power demand and a relatively low fuel specific impulse, especially compared to high voltage EP systems, but also compared to chemical thrusters, as seen in Table 4.2.

Fuel	Evaporation Temp. [K]	Specific Impulse [s]
Water	373	120
Hydrogen	351	72
Rapeseed oil	633	47

Table 4.2: Resistojets: Specific impulse for different types of propellant (Calculated in this project).

4.2.4 Cold Gas Propulsion

What characterizes Cold Gas Propulsion is that unlike chemical rockets and resistojets, cold gas thrusters expels a gas at very low temperature, since it is not heated neither by chemical combustion, nor by electrical heaters. What drives the gas is simply the high pressure under which the gas is stored, and consequently the thrust level is controlled by pressure controllers and valves. Very small valves are available today, of which some are based on piezoelectric actuators. Hence, combined with the low energy contained in the cold gas propellant, it is possible to deliver very small impulsbits. Accordingly, cold gas propulsion is still the preferred principle for low thrust applications.

However, cold gas propulsion obviously suffers from low specific impulse (around 50 - 100 s), and due to the need for fuel storage consuming high mass and volume, people are starting to move their attention to alternative methods. The PRISMA main satellite is flying 3 different propulsion systems, including a scaled down cold gas micropropulsion system with proportionally controlled valves. Additionally the PRISMA microthrusters have heater elements included to raise the specific impulse. However, already after 2 days the experiment suffered from a gas leakage, showing the great advantages people involved with micropropulsion experience.

4.2.5 High Voltage Electric Propulsion

As fabrication techniques within micro- and nanotechnology has been developing and become more and more multifarious, a new type of propulsion has been suggested and many groups around the world have attempted implementing it. Here we talk about propulsion characterized by the principle of the fuel being accelerated by an electric field. Hence the name Field Emission Electric Propulsion, often referred to as FEEP thrusters. Since the fuel is meant to be accelerated in an electric field, it has to be electrically charged. A typical configuration is the one illustrated on Figure 4.4, where the electric field created by the large potential difference $V_E - V_{ACC}$ - in the order of 500 V to 1000 V - is both ionizing the fuel and accelerating it. For these types of thrusters, metals with low melting point are preferable, in order to use as little energy as possible for melting the fuel and thereby facilitating the supplying of fuel by capillary pumps. Such metals are Caesium and Indium for instance, which have melting temperatures of 28.5°C and 157°C respectively.

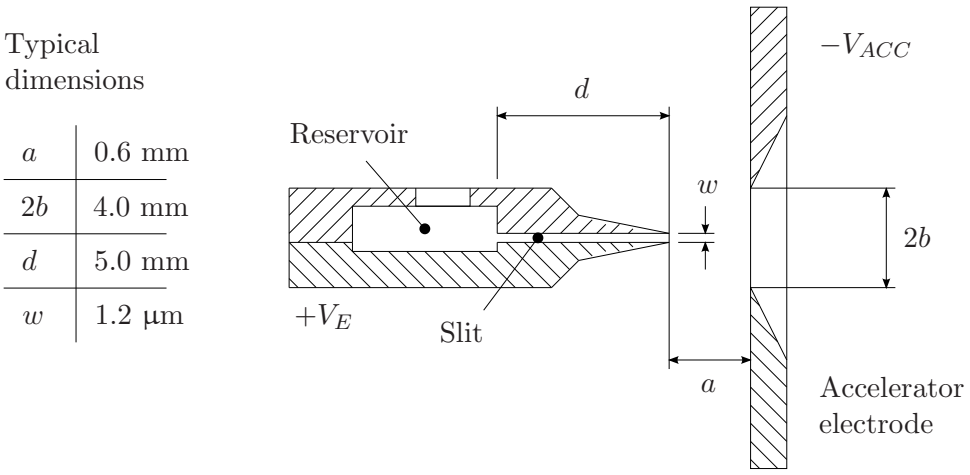

Figure 4.4: The principle of a FEEP thruster. A high voltage between the two electrodes ionizes the metal, and accelerates the ions through the negative accelerator electrode.

As opposed to other types of electric propulsion, the fuel of the thrusters is highly reactive, meaning that the plume of the thrusters is likely to contaminate the spacecraft. Experimental investigations performed for the thrusters which was supposed to be utilized on the MICROSCOPE mission, showed that it could lead to very detrimental deposits, even inducing chemical reactions with polymers. Hence, contamination is a primary concern when implementing this technology. Furthermore it can be a problem for many missions that the spacecraft utilizing the FEEP's will always end up being charged to some degree, due to back-flow of metal ions. This is somewhat reduced by applying an electron source as a neutralizer, but cannot be prevented completely [22].

Another significant issue is the risk of malfunction of a FEEP thruster due to arcing, sparking or flashover. A physical phenomenon that is known to vacuum discharge physicists as vacuum breakdown, i.e. the closing of an insulating vacuum gap by a low-voltage, high-current vacuum arc. This may cause damage to the emitter itself and perhaps to the high- voltage supplies, but the resulting transients from such a phenomena, may also inflict severe damage to the highly sensitive electronic equipment on board a spacecraft. The basic physical problem is due to the intrinsic physical and electronic properties of the element Caesium. Caesium is the preferred fuel for these FEEP's due to its low values of the liquid surface energy σ, of the work function ϕ and the high atomic mass m_a as seen in Table 4.3. But exactly these properties, together with a high vapor pressure at the very low melting temperature, are responsible for a very high risk of flashover and arcing [23].

Although there are many challenges to handle with FEEP thrusters, they

	Symbol	Unit	Caesium	Indium
Surface energy	σ	[J/m^2]	7.10e-2	5.6e-1
Work function	ϕ	[eV]	1.81	4.12
Ionization energy	W_i	[eV]	3.90	5.78
Vapour pressure	p	[Pa]	1.5e-4	<1e-14
Atomic mass	m_a	[u]	133	115
Melting temp.	T	[°C]	28.5	157

Table 4.3: Physical properties of the two most interesting fuels for LMIS (Liquid Metal Ion Source) FEEP thrusters.

are extremely attractive due to their overwhelming performance regarding power to thrust ratio and fuel efficiency. Caesium thrusters, which provide the best performance so far, exhibits values of 5.5 mW/μN and 6000 s respectively [23].

4.3 Summary

A wide range of sensors for precision controlled space flight exists, for which some can be used as stand alone and others need to cooperate with assisting systems. These sensor techniques include visually based systems, GPS, radio frequency metrology systems and electrostatic accelerometers. Among these the visually based system developed at DTU Space shows an all round superior performance for formation flight, and electrostatic accelerometers dominate the field of drag free flight. Different candidates for a micropropulsion principle exists for implementation in the project at hand. These include chemical combustion motors, resistojets, cold gas propulsion and FEEP's. Considering the drawbacks and advantages these principles has shown so far, the principle of a resistojet seems most tempting. Primarily due to the possibilities of simplification, which is a major concern both for integration of the principle with MEMS technologies, and for developing systems for space applications in general. But also due to advantage of controlling the thrust level electrically - yet requiring only simple power processing - and gaining a fair fuel efficiency.

Chapter 5

LTCC Based Resistojet

In this chapter we will describe the realization of the chosen propulsion principle. The idea behind the resistojet designed in this project, is to vaporize a fuel in a controlled manner and release the gas through small nozzles. The goal is to develop a concept being as simple as possible, meaning that we want to avoid integrating microvalves for each nozzle and fuel delivering systems utilizing complex pressure regulators. With this in mind, we came up with a simple concept illustrated in Figure 5.1.

Having liquid fuel - such as water - on board a spacecraft, the fuel tank needs to be pressurized and consequently the major challenge is not how to drive the fuel to the evaporation chamber of the thruster, but how to limit the flow into the chambers. This is done by using small capillaries, through which the flow is controlled by adjusting the pressure in the fuel tank using a heating element. To be able to cut off the thrust entirely, a valve can be integrated between the fuel reservoir and the thruster.

5.1 MEMS Fabrication Technologies

Having chosen a propulsion principle, the next step is to choose a suitable micro-fabrication technology and material for the thruster. The material must be able to withstand relatively high temperatures and be resistant to outgassing in space. Here we have considered semiconductor fabrication using silicon versus LTCC (Low Temperature Co-fired Ceramic) technology. The former is extensively used in the production of integrated circuits, microsensors and actuators and offers

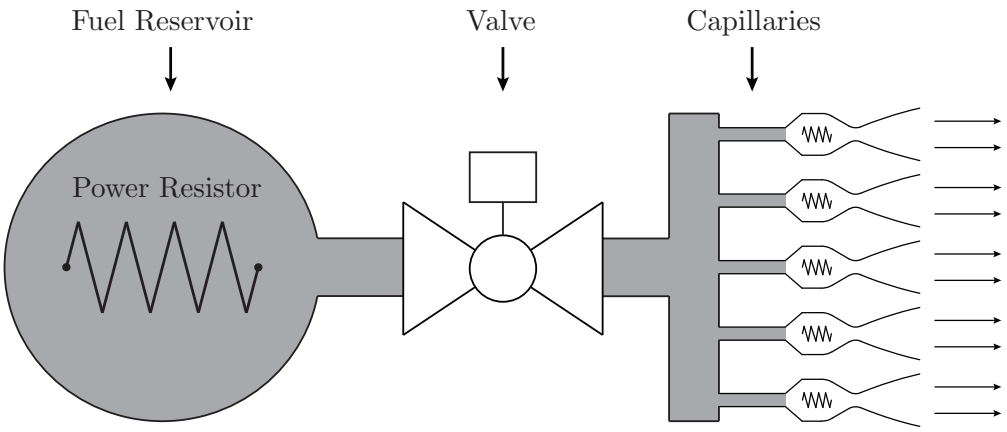

Figure 5.1: The concept of the resistojet developed in this project. A heating element in the fuel reservoir is used to control the pressure, in order to adjust the fuel mass flow through the capillaries supplying the evaporation chambers.

very high precision and reproducibility. The latter is a technology based on ceramic sintered at low temperature for producing multilayered integrated circuits using thickfilm technology, where semiconductor fabrication is based on thinfilm technology. LTCC is also used for fabricating microsensors and actuators and is being used in the development of different types of microthrusters, for instance the pulsed detonation thruster seen in [27]. The disadvantage using semiconductor fabrication is that it has to be performed in an extremely clean environment, which together with the high price of the materials used, makes the implementation of this technology very expensive. Furthermore it is very troublesome to process with other means than planar processing, which in general limits the mechanical structuring to 2D. Therefore our attention is turned towards LTCC, for which the requirements for cleanliness are moderate enough to facilitate production outside a cleanroom. Also LTCC is a very soft material prior to co-firing, facilitating processing techniques like punching, laser cutting and micromilling.

5.2 Thrust and Efficiency

The theoretical considerations on the resistojet being developed here, has the purpose of giving an impression on the necessity of the miniaturization of the microthruster, in order to reach a thrust as low as a few micronewtons. Furthermore, the theory will show how much thrust is achievable as function of power input in the form of heat. In a resistojet the heat is provided by electrical power being converted into heat in a resistor. Hence, assuming all the heat is transferred to the fuel from the resistor, a theoretical thrust curve can be obtained. This is done

in much the same way as for a chemical rocket. The only difference is that the heat is produced only by electrical resistance and not by any combustion.

The theoretical power efficiency of a resistojet, is limited partly by the necessary energy consumption for a certain amount of fuel evaporated - since this limits the mass flow - and partly by the temperature reached in the evaporation chamber - since this limits the exhaust velocity. Similarly to a chemical rocket, where this limitation is due to the chemical energy bound in the fuel and the temperature at which the fuel is burned. The energy consumption needed for the fuel evaporation is determined by the latent heat of vaporization L for the fuel of interest. This physical property is measured in J/kg and states how much heat E a certain quantity of a liquid requires in order to make a phase transition into the gas phase. Consequently:

$$L = \frac{E}{m} \tag{5.1}$$

By rearranging Equation 5.1 and by considering the principle of mass conservation, we find that the maximal achievable mass flow $\dot{m}$ for a certain power input P is derived by taking time derivative of Equation 5.1:

$$m = \frac{E}{L} \quad \Rightarrow \quad \frac{dm}{dt} = \frac{dE}{dt}\frac{1}{L} \quad \Rightarrow \quad \dot{m} = \frac{P}{L} \tag{5.2}$$

Assuming the steam at temperature T and molecular weight W obey the perfect gas law, the pressure in the chamber added by the mass flow, is found by [26]:

$$p_m = \frac{\dot{m}}{\sqrt{\gamma}\left(\frac{2}{\gamma+1}\right)^{\frac{\gamma+1}{2(\gamma-1)}}\frac{A_t}{\sqrt{\frac{RT}{W}}}} \tag{5.3}$$

where γ is the ratio of specific heats, R is the universal gas constant and A_t is the throat area of the nozzle. The total chamber pressure p_c is found as the sum of the p_m and the ambient pressure p_a, which is $p_a \approx 10^{-7}$Pa for LEO and therefore neglectable in space. The exhaust velocity is found by [26]:

$$v_e = \sqrt{\frac{2\gamma RT}{(\gamma-1)W}\left(1 - \left(\frac{p_e}{p_c}\right)^{\frac{\gamma-1}{\gamma}}\right)} \tag{5.4}$$

where p_e is the exhaust pressure. Assuming the steam is ideally expanded, the exhaust pressure is equal to the ambient pressure. This is obviously never entirely true, thus the thrust reads:

$$F = \dot{m}v_e + A_e(p_e - p_a) \tag{5.5}$$

Looking at Equation 5.4 and 5.3, we see that an increasing temperature leads to a higher exhaust velocity, for a constant mass flow. This translates into a higher fuel efficiency, as seen on Equation 5.5, since we can get the same thrust with a lower mass flow. The thrust is maximized by having an exhaust pressure as close as possible to the ambient pressure ($p_e - p_a = 0$). This is due to the fact, that as long as there is a pressure in the diverging part of the nozzle exceeding the ambient, the exhaust velocity continues to increase. However, in space there will always be some degree of under expansion ($p_e - p_a > 0$). The fuel efficiency is normally quantified by the I_{sp} - specific impulse, which is basically a measure of the exhaust velocity. This quantity is normally given in seconds, being the time the thruster will burn while delivering a thrust equal to the initial weight of its fuel, and is thus calculated by:

$$I_{sp} = \frac{F}{\dot{m} \cdot g} \tag{5.6}$$

where g is the acceleration due to gravity at the surface of the Earth.

Considering the fraction $\frac{p_e}{p_c} = \frac{p_e}{p_m + p_a}$ from Equation 5.4, of which the exhaust velocity is highly dependent, the performance of the thruster will be radically different in atmospheric conditions from that in vacuum. This is due to the fact that for a microthruster, the part of the chamber pressure produced by the mass flow of the fuel, is minute compared to the part of the chamber pressure present due the ambient - when atmospheric conditions are considered. Hence, the fraction $\frac{p_e}{p_c}$ will be large for operation in space and very small for operation in atmospheric conditions, and consequently looking at Equation 5.4 the theoretical exhaust velocity becomes large for space operation ($\approx$ 1200m/s for Water and $\approx$ 700m/s for Ethanol) and very small for operation at atmospheric pressure ($\approx$ 85m/s for Water and $\approx$ 50m/s for Ethanol). Additionally, in practice the exhaust velocity will most likely be significantly lower due to the boundary layer in the expanding part of the nozzle being extensive, compared to the dimensions of the small nozzles fabricated in this project.

To predict the performance of the reistojet in terms of thrust to power ratio and specific impulse, an assumption of the practically reachable temperature in the chambers is necessary. Reaching a higher temperature increases the efficiency, but also the thrust, if not limited by limiting the mass flow. We cannot limit the mass flow by turning down the power, since this translates into a lower temperature. The only way forward to get a reasonable efficiency and a low thrust, is then by limiting the mass flow using a smaller nozzle. Optimizing our fabrication we reached a nozzle throat diameter of only 210 µm. And using an infrared camera, we determined the temperature of the heating filaments as function power. With these parameters we have plotted the thrust and specific impulse versus power for both atmospheric conditions and vacuum, as seen in Figure 5.2, 5.3, 5.4 and 5.5. Hence, theoretically we should arrive at a thrust to power ratio of about 90µN/W in atmospheric conditions and 500µN/W in vacuum. In Appendix A the plots for the mass flow contribution to the chamber pressure vs. power and mass flow vs. power, are included. Specifically the mass flow is important, since this is used in the dimensioning of the capillary part of the thruster.

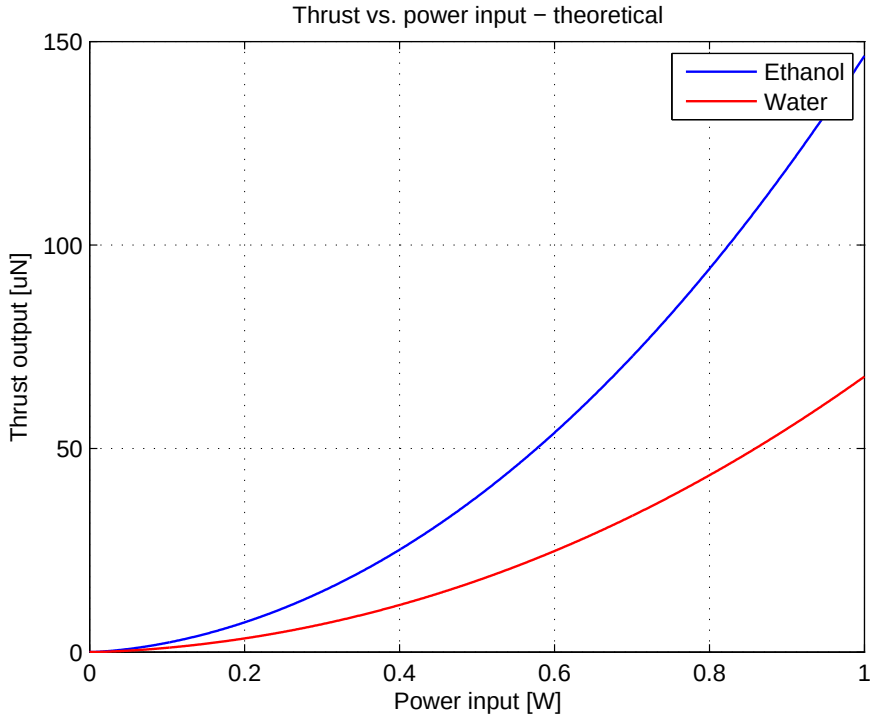

Figure 5.2: Theoretical thrust in atmospheric pressure

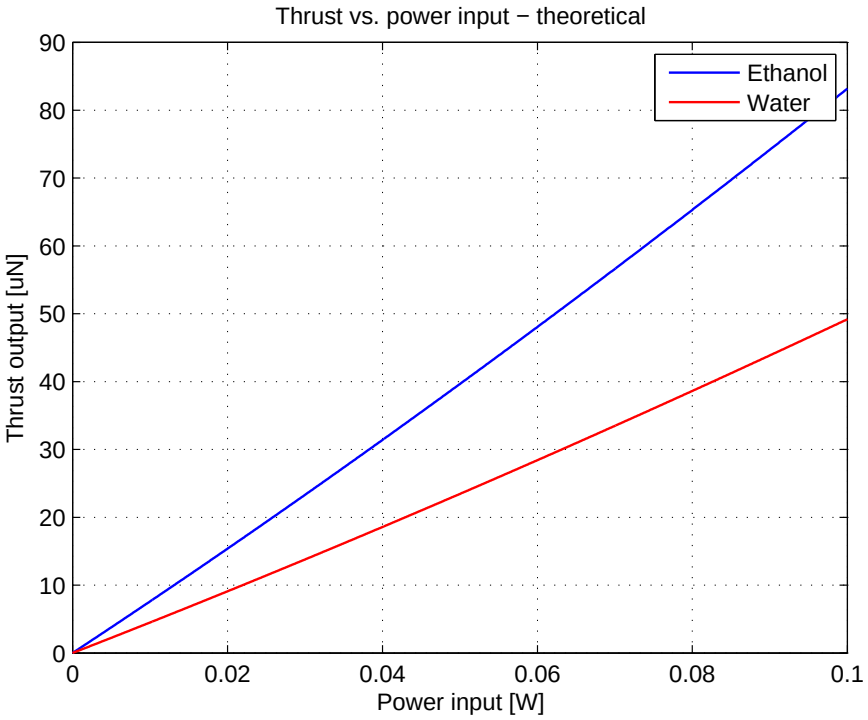

Figure 5.3: Theoretical thrust in vacuum

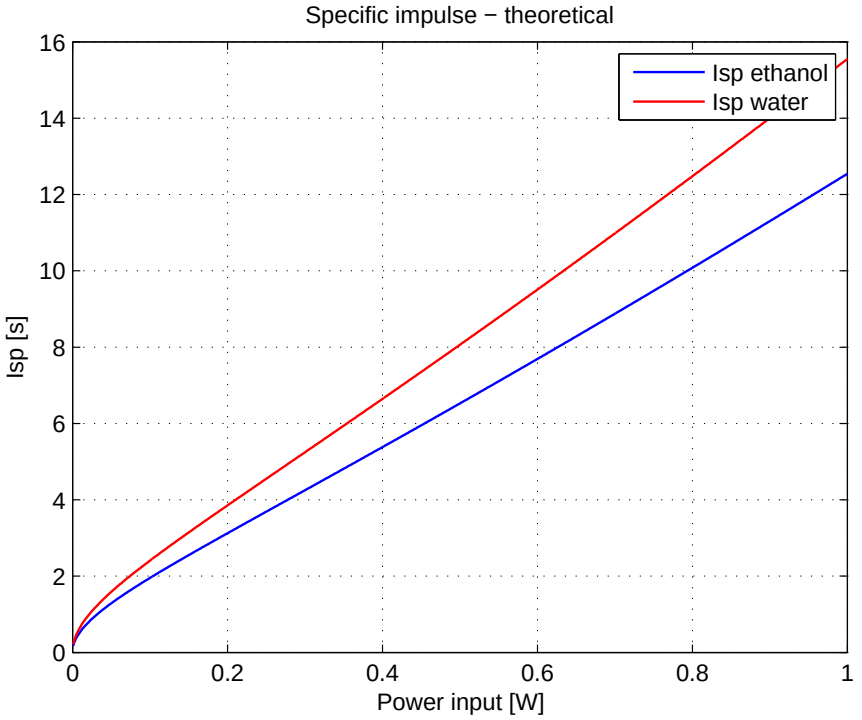

Figure 5.4: Theoretical specific impulse in atmospheric pressure

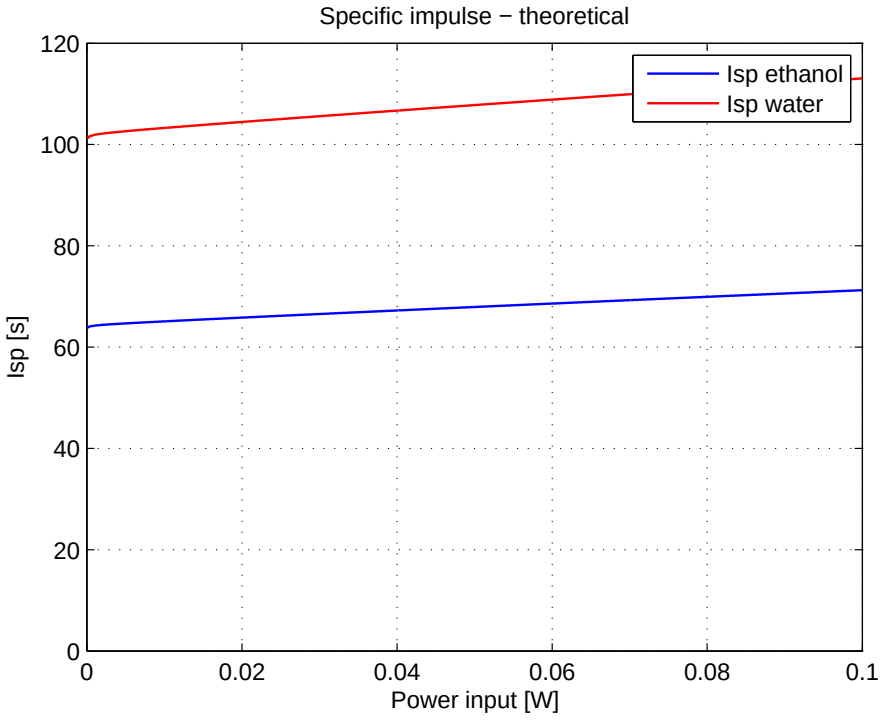

Figure 5.5: Theoretical specific impulse in vacuum

5.3 Converging Diverging Nozzles

Both 2D and 3D converging diverging nozzles are used for various thrusters based on releasing gas under pressure. Basically the objective of a nozzle is as smoothly as possible to release a gas under high pressure and let it expand to a unidirectional plume without creating turbulence or shock waves.

In the converging part of the nozzle, the flow should be kept subsonic until the throat is reached, from where the gas is expanding freely in the diverging part and the velocity continues to increase at supersonic speed towards the exhaust.

5.3.1 Conical Nozzle Design

The simplest design is a conical nozzle, which is relatively easy to manufacture and which can be sufficient in many cases. The design parameters of a conical nozzle include the converging cone angle β, the throat area (determined by the desired nominal thrust), the radius of curvature of the throat R_t, the diverging cone angle α and the expansion ratio A_e/A_t, as seen in Figure 5.6. The the diverging cone angle is an important parameter, determining the efficiency of the nozzle together with the expansion ratio, which is the ratio between the area of the throat and the

area of the exit. Bigger expansion ratio and smaller diverging cone angle, increases the efficiency of the nozzle, but with the cost of a bigger and heavier nozzle. If the nozzle otherwise has reasonable dimensions, the thrust can be approximated by:

$$F = \frac{1}{2}\dot{m}v_e(1 + \cos(\alpha)) \tag{5.7}$$

considering the thrust lost due to the fact that a unidirectional plume is not achieved. An $\alpha = 15°$ is often used, which gives a factor of $1/2(1+\cos(\alpha)) = 98.6\%$.

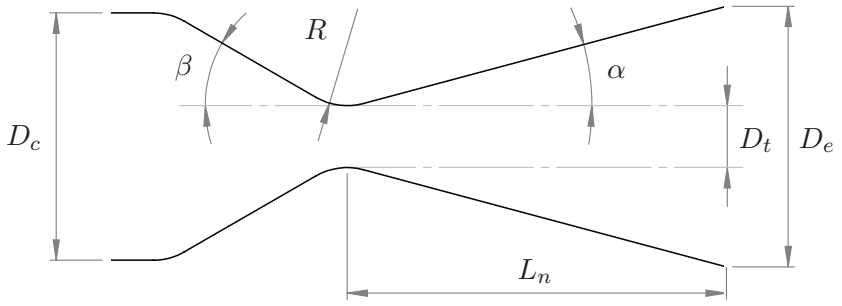

Figure 5.6: The diverging part of a conical nozzle often has a half angle of $\alpha = 15°$, to get a reasonable efficiency while cosidering the size of the nozzle together with the expansion ratio. The radius of curvature R_t of the throat is typically equal to the throat diameter ($R = D_t$) to reduce the fluid boundary layer. The angle of the converging part of the nozzle is typically $\beta = 30°$, but is less important for the performance.

5.3.2 Bell Nozzle

The so called de Laval bell shaped nozzle was invented towards the end of the l9th century by Carl de Laval, and is often harder to produce than a conical nozzle similar. However, the advantage of the bell nozzle, is that the efficiency can be increased by reducing the nozzle exit wall angle α (similar to the diverging cone angle for conical nozzles), while keeping the dimensions comparable to a corresponding conical nozzle. This is done by reducing the radius of curvature of the throat, at the very beginning of the diverging part (here denoted R_d), and by increasing the initial wall angle θ, as seen on Figure 5.7. Thereby a fast expansion is achieved in the initial divergent zone, follow by an axially directed flow due to a gradual change in curvature towards the exit.

A bell nozzle is often specified according to its equivalent 15°-diverging cone angle conical nozzle. Hence, the axial length L_n is specified as a fraction of the length of a 15°-diverging cone angle conical nozzle having the same throat area, radius of curvature of the converging part and area expansion ratio. A fractional length larger than $L_f = 80\%$, does not significantly improve the performance.

The curvature of the diverging part of a bell nozzle can take different shapes. A near optimum bell nozzle curvature uses the parabolic approximation procedures, suggested by G.V.R. Rao. The initial radius of curvature is $R_c = 0.75D_t$, while the diverging section starts with a circular part with radius $R_d = 0.191D_t$ and continues towards the exit along a parabola. A specific nozzle is designed on the basis of the desired throat diameter D_t, axial length of the nozzle L_n from the throat to the exit plane (or the desired fractional length L_f, based on a 15° conical nozzle), expansion ratio ϵ, initial wall angle of the parabola θ and nozzle exit wall angle α.

For the final nozzles produced in this project, an 80% bell nozzle was designed with an expansion ratio of 36, an initial wall angle of the 20° and an exit wall angle of 7.5°.

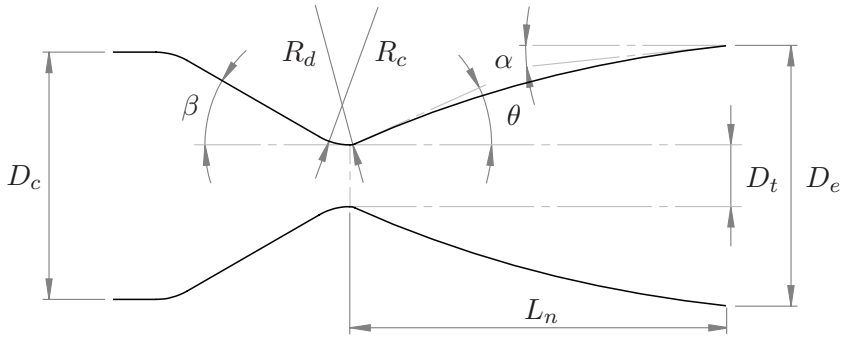

Figure 5.7: Designing a bell nozzle it is possible to reduce α and thereby increase the efficiency, without increasing the size of the nozzle. This is done by reducing the radius of curvature of the throat, at the very beginning of the diverging part (here denoted R_d), and by increasing the initial wall angle θ. Thereby a fast expansion is achieved in the initial divergent zone, follow by an axially directed flow due to a gradual change in curvature towards the exit.

5.4 Microfluidics

5.4.1 Capillarity

To limit the fuel flow the last stretch before it enters the evaporation chambers of the microthruster, the intention is to make the fuel flow by capillary forces in small tubes. For the testing done in atmospheric conditions - where the pressure in the fuel reservoir is the same as the ambient - the issue is to dimension the tubes such that they can provide a flow greater than what is necessary for the thruster to provide a continuous thrust. For operation in space, the purpose of the capillaries is to limit the fuel flow due the pressure difference between the fuel reservoir and vacuum. Theoretically this can be done either by dimensioning the length and diameter of the tubes such that the resistance towards the flow through the tubes - due to the viscosity of the fluid - is high enough or by dimensioning only the diameter of the tubes, such that the surface tension can hold back the drop of the fluid at the very end of the individual tube. Hence, the purpose of the following section is partially to become capable of determining the mass flow rate - expressed in terms of tube dimensions, fluid characteristics (such as surface tension and viscosity) and surface properties of the material of the tubes and partially to become capable of determining the pressure difference a tube of a certain diameter can handle. In Figure 5.8 Left the situation is illustrated where a fluid flows through a tube due to capillary forces and in Figure 5.8 Right we see the situation where the surface tension maintains a pressure difference exactly equal to the pressure difference between the chamber and outer space, at the limit where the contact angle becomes 180°.

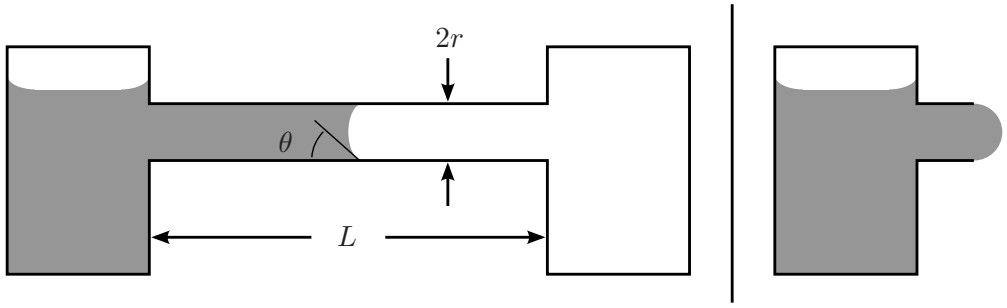

Figure 5.8: Left: Illustration of capillary filling. Right: Illustration of the situation where the pressure difference between the chamber and the ambient reaches the very limit of what the surface tension on the bobble can withstand.

Using the analogy of electrical current in an electrical conductor, the flow rate of liquids in small tubes - denoted Q and measured in milliliters per second - can be thought of as being the "current" normally measured in Amps. In the same

way, the pressure difference driving the liquid flow, is thought of as the "voltage", and consequently very similar to Ohm's law ($V = R \cdot I$) a relation between the flow rate and the pressure difference, can be written:

$$\Delta p = Q \cdot R \tag{5.8}$$

The contribution due to capillary forces can be expressed by:

$$\Delta p = \frac{2\gamma \cos(\theta)}{r} \tag{5.9}$$

Which is valid for a tube with circular cross section and radius r. For a detailed review, see [28]. Here γ denotes the surface tension of the fluid and θ denotes the contact angle between the fluid and the surface, as seen on Figure 5.8. The resistance to the flow is derived in [28] and is for the circular cross section given by:

$$R = \frac{8\eta L}{\pi r^4} \tag{5.10}$$

with η being the viscosity of the fluid and L being the length of the channel/tube. Consequently we have for the mass flow rate:

$$Q_m = Q_V \cdot d = \frac{2\pi r^3 \gamma \cos(\theta)}{8\eta L} \cdot d = \frac{\pi r^3 d\gamma \cos(\theta)}{4\eta L} \tag{5.11}$$

where d denotes the density of the fluid. The contact angle is determined by placing a small drop of the fuel of interest on top of a piece of LTCC ceramic and then acquire an image of the drop in a direction parallel to the surface of the ceramic. The contact angle can then be measured on the acquired image, as seen on Figure 5.9. On the image it is seen that the surface of the ceramic is very hydrophilic, meaning that the surface tends to attract the fluid. Hence, the contact angle is only 26°. Putting these parameters into Equation 5.11, which are seen in Table 5.1 for water, we get a mass flow rate of 3.22×10^{-4}kg/s in a tube of $L = 2.5mm$ and a radius of $r = 0.25mm$, when using water as a fuel.

Density	$d =$	1.0×10^{3}	kg/m^3
Viscosity	$\eta =$	1.0×10^{-3}	Pa s
Surface Tension	$\gamma =$	72.9×10^{-3}	J/m^2

Table 5.1: Physical properties of water necessary for determining the capillary mass flow.

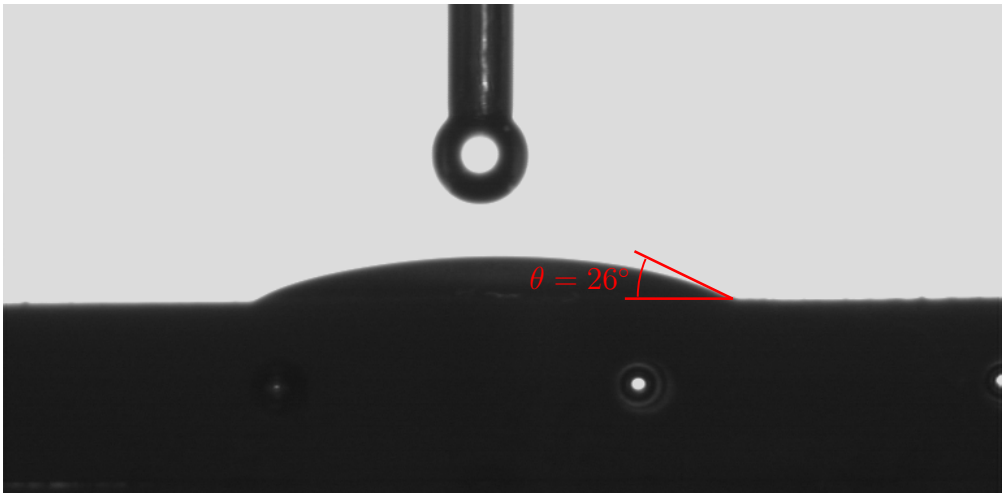

Figure 5.9: Measuring the contact angle of a water drop on top of a sample of LTCC ceramic. It is easily seen that the surface is very hydrophilic (water loving), with a contact angle of only 26°.

5.4.2 Porosity

Prototyping showed that the key to success for the microthruster, was the implementation of a porous material for limiting the mass flow. Estimating the mass flow rate in a hydrophillic porous material being wetted on one side, the microchannels contained in the material is assumed to work in a similar manner to an equally distributed array of parallel capillaries. The diameter $2r_c$ of these capillaries is defined to be equal to the mean pore size. To find how many capillaries the microchannels corresponds to, it is necessary to know the volume occupied by the microchannels within the material. This can be found in two ways. Knowing the density d_s of the glass which constitutes the solid part of the porous material, and knowing the density d_p of the porous material, the volume V_c occupied by the microchannels can be found by:

$$\frac{d_p}{d_s} = \frac{V_p - V_c}{V_p} = \frac{V_p - N_c t_p \pi r_c^2}{V_p} \Leftrightarrow \tag{5.12}$$

$$V_c = V_p(1 - \frac{d_p}{d_s}) = N_c t_p \pi r_c^2 \Leftrightarrow \tag{5.13}$$

$$N_c = \frac{V_p(1 - \frac{d_p}{d_s})}{t_p \pi r_c^2} \tag{5.14}$$

where $V_p = w_p l_p t_p$ is the volume of the porous material, N_c is the number of capillaries, t_p is the thickness of the porous material - thus the length of the capillaries - and r_c is the radius of the capillaries, as seen on Figure 5.10. Another way of finding the volume V_c of the microchannels, is simply to measure it directly, by dipping a sample of the porous material into a fluid, let it absorb as much of the fluid as it can, remove it from the fluid and then measure the volume of the fluid before and after. The volume V_p of the sample is simply found by measuring its outer dimensions (w_p, l_p and t_p). Potentially but not necessarily the volume of the solid part can be determined by measuring how much of the fluid is displaced, while the material is submerged. Having measured these volumes, Equation 5.14 simply reads:

$$\begin{aligned} N_c &= \frac{V_c}{t_p \pi r_c^2} \\ &= \frac{V_p - V_s}{t_p \pi r_c^2} \end{aligned}$$

Having the number of capillaries, the mass flow rate Q_p through the entire block of material from one side to the other, is found using Equation 5.11:

$$Q_p = N_c Q_m = \frac{V_p(1 - \frac{d_p}{d_s})}{t_p \pi r_c^2} \frac{\pi r_c^3 d_f \gamma \cos(\theta)}{4 \eta t_p} = \frac{w_p l_p (1 - \frac{d_p}{d_s}) r_c d_f \gamma \cos(\theta)}{4 \eta t_p} \tag{5.15}$$

where d_f is the density of the fluid. As expected the mass flow rate is proportional to the cross-sectional area $w_p l_p$, proportional to the porosity r_c and inversely proportional to the thickness t_p of the material.

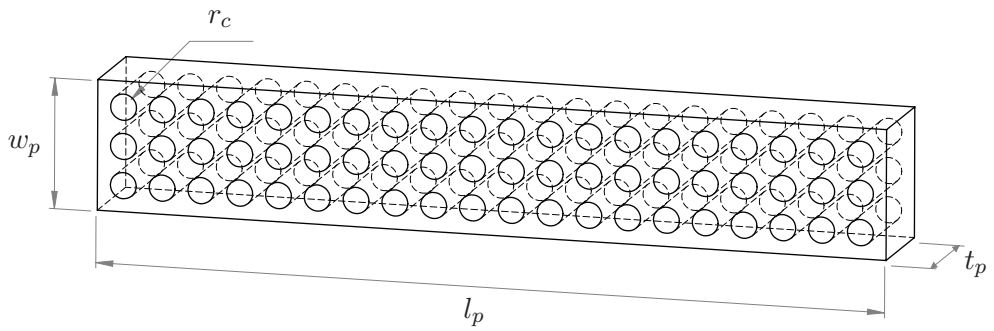

Figure 5.10: The mass flow rate through a block of a porous material we estimate by representing the porous material by a block with a number of perfectly aligned capillary tubes.

5.5 Design

In this section, issues to be considered when designing the prototypes are presented. Later in Section 5.8 of this chapter, the fabrication of the different designs is presented. Initially the objective is to develop a prototype for verifying the performance of the principle in atmospheric conditions, and thereby making a proof of concept. Later it is then considered how to test the concept in vacuum.

5.5.1 Platform and Concept

In order to delimit the experimental work of this project, a suitable platform on which the concept implemented here is build, has to be defined. This will serve as a template for testing the ideas coming up during the brainstorming. The chosen platform for fabricating the resistojets is based on substrates of LTCC processed by micromilling. Micromilling is chosen for the processing, since it offers 3D structuring of the material on CNC milling machines facilitating the manufacturing of 3D Bell nozzles for optimal performance. The CT 700 LTCC HERATAPE used in this project comes in sheets of thicknesses 130 µm, 200 µm and 300 µm. Hence, lamination of several layers are performed of sheets of the 300 µm thickness to reach a proper substrate thickness for the prototype being fabricated.

One of the primary advantages of MEMS technology is the possibility of a large redundancy. On the other hand this is also a necessary property, due to the difficulties in controlling the outcome of the processing perfectly. Hence, the implemented concept includes a number of 5×5 individual nozzles per thruster. Accordingly, a substrate of 20 mm by 20 mm with a thickness of 3 mm (before

sintering) and 5 nozzles integrated, is chosen as a platform for the prototyping. To facilitate micromilling, this substrate naturally needs to be made from two halves, which are laminated after milling. Ultimately, the aim is thus to stack 5 of these substrates to constitute one thruster. As part of the goal, i.e. to simplify the design as much as possible, and to avoid using microvalves which are highly unsuitable for space applications, the fuel is transported to the evaporation chamber by means of capillary forces in this concept.

5.5.2 Heating Element, Metallic Filament vs. Thickfilm Resistor

The most optimal heat transfer is acquired if the heating element is in direct contact with the fuel to be evaporated, such that the heat can be transferred by conductance and not only by radiation. In order to minimize the amount of heat transferred to the substrate of the thruster and thereby getting lost, the heating element should have as little thermal contact as possible to the substrate. Furthermore the resistance of the heating element should be high, such that the required current for applying a certain amount of power is limited. Otherwise a large amount of power will be disposed in the conductors supplying the heating element. A thin metallic wire/filament is initially chosen as the heating element, since this is easily integrated in such a way that is has little contact with the LTCC substrate. Normally when using LTCC, resistors are made as thickfilm resistors applied by screen printing. But as these has a large contact area to the LTCC on which it is applied, it is preferred to start experimenting with filaments as heating elements. Also by making the filament thinner at the very tip, the resistance of the filament can be significantly increased at the very point where the heat is needed. On later prototypes also thickfilm resistors was utilized. The advantage of these are the higher resistance, the smaller chamber required and better reproducibility. The disadvantages turned out to be the complexity of the structure and vulnerability to the fuel.

5.5.3 Implementation

In the following we go through the different designs of the prototypes fabricated in this project. These prototypes serves the purpose of conducting a proof of concept in atmospheric conditions, and consequently it was assumed initially that there would be no reason of being concerned about any pressure difference between the fuel reservoir and the ambient, as long as we use an open fuel reservoir.

Basically the problem is how to implement the heating elements with capillary fuel channels. On the first design fabricated - Design D4 - the filaments are placed as seen on the illustration of a cross sectional view in Figure 5.11 Left, where the filaments are in contact with the fuel at the very end of a 0.5 mm capillary. With this configuration the fuel instantly fills the whole chamber and nozzle when fueling the thruster, and when turned on the power dissipated in the heating elements is insufficient to evaporate the fuel since the mass flow through the supplying capillary is too large. The filling is thought to be due to wetting of the filament and consequently it is attempted on the next design - Design D5 - to withdraw the filament as seen in Figure 5.11 Middle. However, this is found not to be sufficient to solve the problem. Hence, on the third design fabricated the idea is to make a sharp edge on the very end of the capillary tube in order to prevent the fuel from crawling around the corner of the tube and thereby wetting the chamber and nozzle. Consequently, the 20mm × 20mm × 3mm substrate needs to be divided into 3 parts to make the fabrication possible; a top and a bottom substrate and a part with incorporated capillary tubes. A cross section of this design is seen in Figure 5.11 Right.

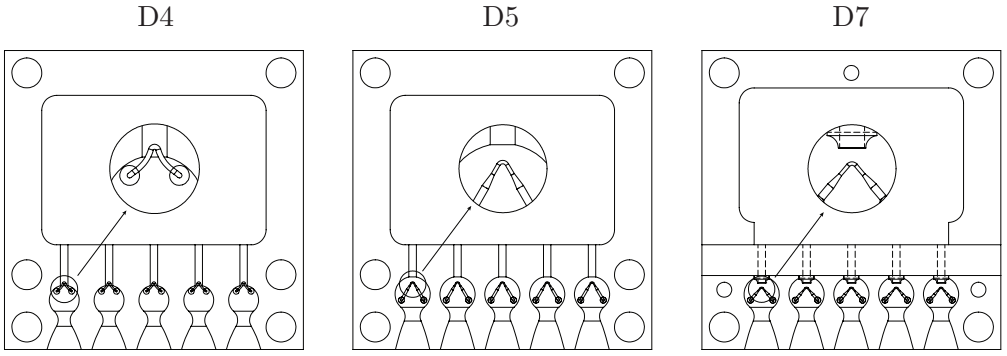

Figure 5.11: Placement of the metallic filaments on the first 3 prototypes fabricated.

The design D7 seen in Figure 5.11 Right provides a working thruster, although this thruster still suffers to some extent from occasional wetting of the chamber during operation, leading to recurring thrust breakdown. Furthermore the thrust is to 2 to 3 orders of magnitude too high at the current where the thrust suddenly rises rapidly. This is initially assumed to be due to a higher temperature in chambers than anticipated. The heat is mainly transferred to the water by radiation, which does not become significant until the temperature of the filament is extremely high. Consequently, when the chamber is eventually filled with steam, the steam gets heated to this high temperature, resulting in a too high thrust. Consequently, the fourth design is made to combine the advantages of having a sharp edge on the capillary tube, and having the filament in direct contact with

the fuel. Consequently, the part with incorporated capillary tubes is divided into two parts and channels are milled in order to make room for the filament, which is placed inside the capillary tube with the tip placed at the very end of the tube, as seen on Figure 5.12 E. Unfortunately this design was never tested, as the edges of the capillary tubes broke during sintering, due to lack of tolerance in the dimensioning of the channels containing the filaments. This was found conducting a DPA (Destructive Physical Analysis) as seen on Figure B.11 in Appendix B.

Due to the unreliable functioning of design D7 seen in Figure 5.11 Right, it is likely that design D9 would only increase the efficiency of the heat transfer, but still suffer from the same unreliability due to the similar dimensioning of the capillary tubes. Therefore, carrying on with the prototyping it was decided to try a new design - Design D13 - with significantly smaller capillary tubes (only 0.1 mm of diameter), which makes the surface tension of the fuel more dominating, thereby giving a better tolerance on the allowable pressure difference between the fuel reservoir and the ambient. Also the throat diameter on the nozzles were reduced to 0.5 mm on three of them, and only 0.25 mm on the two remaining, in order to attempt reducing the thrust as much as possible.

However, Design D13 makes it practically impossible to place metallic filaments inside the tubes and consequently the attention is turned towards thickfilm resistors as heating filaments. Using thickfilm resistors the problem is to make a design where the thermal contact to the substrate is minimized and the thermal contact to the fuel is maximized. Hence, a design is made where thickfilm resistors are printed on a single sheet of LTCC and the capillary tubes are drilled through both the sheet and the resistors, as seen on Figure B.12 in Appendix B. Consequently the very end of the capillary tubes will get hot, which is preferable. This single sheet of LTCC is placed perpendicular to the substrate, with the thickfilm resistors turning inwards the chambers as seen on Figure 5.12 Right. Fueling this design the diameter of the capillary tubes are actually sufficiently small for the surface tension to detain the fuel, but as soon as the thruster is turned on, it suffers from the same problem as the previous designs. Furthermore it was learned that the material of the thickfilm resistors gained a rapid irreversible increase in resistance being in contact with water while being heated.

After making these 5 prototypes, we learned that it is simply practically impossible to prevent wetting of the chambers and nozzles when heating up the thruster, despite the fact that the dimensions of the tubes should render it possible for the surface tension to detain the fuel at the very end of the tubes. Consequently, the fuel flow into the chambers needs to be limited to an extent where the heating elements can keep up with evaporating the fuel gradually. Hence, the capillary

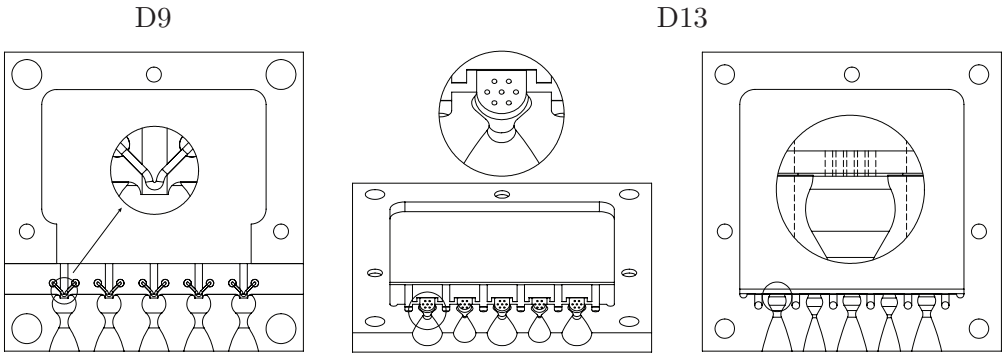

Figure 5.12: Left: Design D9 with the metallic filaments integrated inside the capillary tubes. Right: Design D13 with capillary tubes of only 0.1 mm of diameter, drilled through a single sheet of LTCC with printed conductors and thickfilm resistors.

tubes needs to be either micrometer size in diameter or around a meter long. It was attempted milling channels only 50µm deep and 100µm wide in single sheets of LTCC, and subsequently laminate them under high pressure in uniaxial press, as described in Section 5.8.1. After lamination however, the channels had collapsed and therefore this idea was dropped. As it turned out to be too troublesome to machine such small channels using the LTCC material, a research of porous materials which could be integrated with the LTCC material was initiated. This topic is discussed in the following section. The idea was then to use the porous material to limit the fuel flow. Three different prototypes were fabricated using this idea. These are the designs seen in Figure 5.13 and 5.14, where D15 was fabricated in both an A and a B version, with the A version having a metallic filament like the previous designs (D4, D5, D7 and D9) and the B version having a metallic filament winded as a coil to increase the resistance. Design D14 utilized the thickfilm resistors once more, but this time with a layer of cover glass, which on a test resistor had shown to be suitable for sealing the resistor towards the fuel. As seen on Figure 5.13 this facilitated the placement of the resistors very close to the face of the porous material. This thruster functioned very convincing, but only for a very short time, before the resistors malfunctioned, despite the fact that these resistors were sealed with cover glass, unlike the ones on Design D13. The explanation to this is likely that the resistors integrated on the thrusters cannot handle the high power being dissipated, since they are somewhat smaller than the resistors successfully tested with the cover glass sealing. Hence, the thickfilm resistors might work fine for operation in vacuum, where a smaller power is sufficient for the same thrust. The D15A and D15B worked satisfactory, and the D15B obviously gave a larger thrust range due to the larger resistance in the filaments. Consequently, the D15B was the one used for most of the characterization.

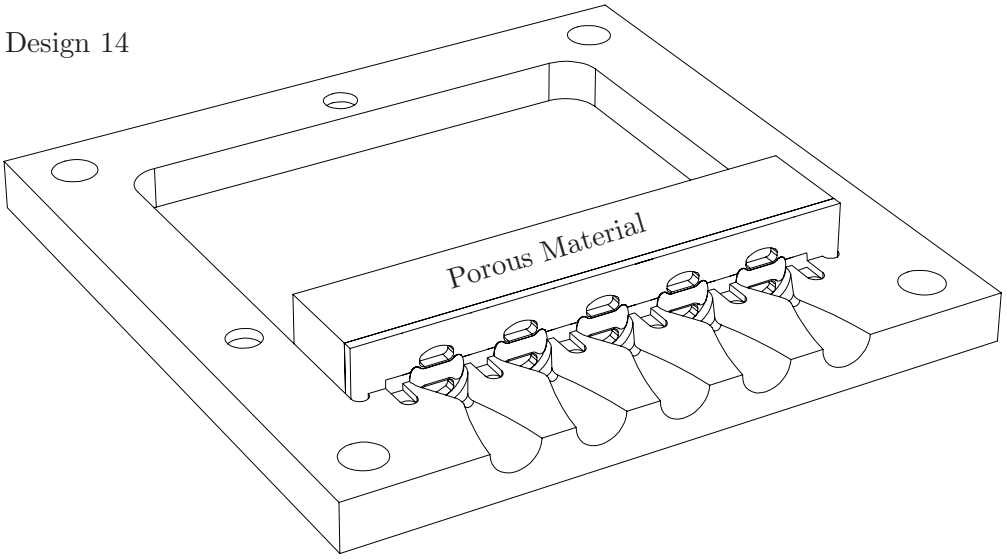

Figure 5.13: Design 14 utilizes thickfilm resistors, printed on a single sheet of LTCC, which is laminated vertically using coverglass paste at the entry of the evaporation chambers. Small holes are milled above and below the thickfilm resistors, from which the fuel evaporated.

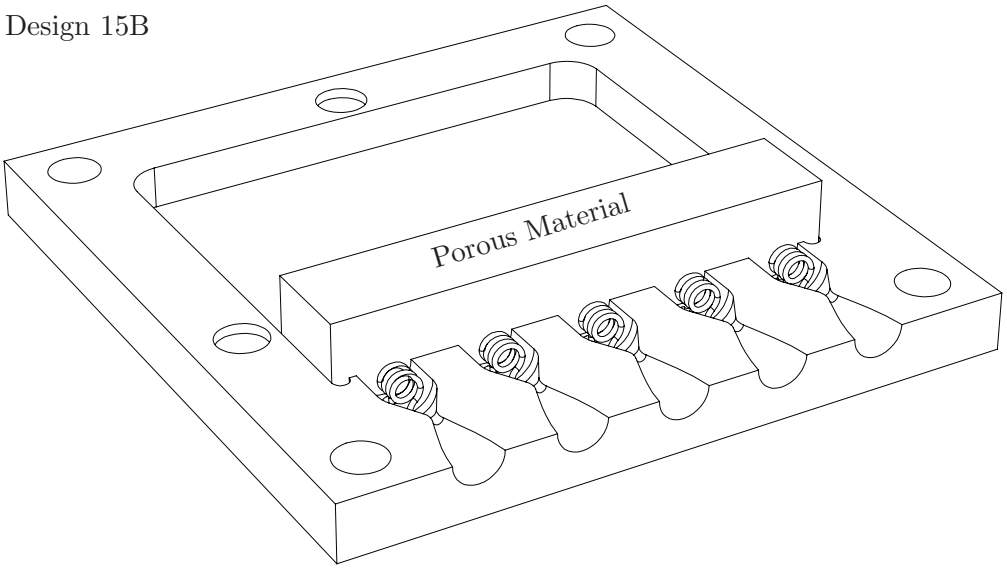

Figure 5.14: Design 15 A and B utilizes platinum filaments. On the D15A the filaments are similar to the previous designs (D4, D5, D7 and D9). On D15B the resistance is increased, making 4 windings by coiling the wire around a 0.6 mm rod.

5.6 Porous Materials

As learned during the prototyping, the only way to limit the fuel flow into the chambers, using capillarity for delivering the fuel, is to use capillary channels with diameters in the order of a few micrometers. Since fabricating such small structures using LTCC technology is practically impossible, porous materials are investigated in this project, which naturally have microchannels embedded inside the material. Specifically porous materials with the potential to be integrated with LTCC by co-firing are interesting. Consequently porous ceramics become interesting. The capacitive paste used for integrated circuits on LTCC was initially considered, as it was noticed that this material after being sintered seemed to be wetted when ethanol or water was applied. However, looking more closely in a Scanning Electron Microscope (SEM), the porosity seemed to be present only on the surface of the material, as seen on Figure C.1 in Appendix C. Clay is a material known to be porous when sintered. Hence, in an effort to make the capacitive material porous, a sample of the paste was mixed with clay. Another sample was mixed with carbon powder crushed in a mortar to make the particles smaller. These two samples, together with a sample of pure clay, was sintered using the same temperature profile as the one used for the LTCC. As seen on the SEM images in Figure C.2 to C.4 in Appendix C, all these 3 samples exhibited porosity in the submicron regime. However, the material obtained using the carbon powder became very inhomogeneous with pore sizes ranging from a few microns to a few hundreds of microns. Perhaps by filtering the carbon particles, a better result is achievable. Gipsum exhibited porosity in the desired range and was co-fired with LTCC with success. Hence, a few bulk rods of gypsum was made to measure the mass flow rate, and it was experienced that we could control the mass flow rate by mixing the gypsum with silicon carbide SiC. Silicon carbide is used by others for resistojets for station keeping, using it as bed material [29]. However, gypsum is very brittle and considering the risk of having gypsum particles blocking the nozzle throats, attention was turned towards other materials.

Studying the microfluidics we came along a material known as glass frit, from the book of Henrik Bruus, *Microfluidics* [28]. This material can be made from different types of glass, such as borosilicate and quartz, and is sintered in such a way that it becomes porous. It is mostly used in chemistry for filtering and comes in different porosities, as seen in Table 5.2. But the material is also used in microfluidic pumps, and was found to be suitable for integrating with the LTCC. Hence, calculating the mass flow through a block of glass frit using Equation 5.15, it was found that porosity P4 was suitable for a thruster operating in atmospheric

Class	ISO/4793	Poresize [µm]	Class	ASTM/BS	Poresize [µm]
00	P 500	250 - 500	EC	Extra Coarse	170 - 220
0	P 250	160 - 250	C	Coarse	40 - 60
1	P 160	100 - 160	M	Medium	10 - 16
2	P 100	40 - 100	F (BS)	Fine (BS)	4 - 10
3	P 40	16 - 40	F (ASTM)	Fine (ASTM)	4 - 5.5
4	P 16	10 - 16	VF	Very Fine	2 - 2.5
5	P 1.6	1.0 - 1.6	UF	Ultra Fine	0.9 - 1.4

Table 5.2: Available glass frit porosities for two different standards (ISO/4793 and ASTM/BS). The one used in this project is the P4.

pressure, and P5 was suitable for vacuum. Consequently, this material was used for the final prototypes.

5.7 LTCC in general

LTCC substrates are multilayered structures consisting of ceramic plates (also known as "green tape" or "green sheets"') which are screen printed, laminated and co-fired. The term co-firing is used since the conductors on the substrate are baked and sintered during the same heat treatment as the ceramic material. This is done at a relatively low temperature of 850°C, compared to HTCC where the sintering is done at about 1600°C [30]. LTCC is therefore compatible with high conducting thick films such as silver and gold. The advantage of this multilayered technology is that every layer of the ceramic can be processed independently before co-firing. This facilitates the fabrication of structures like cavities and grooves and screen printing of several conductor layers as well as passives. Therefore a dense integration of thick film based passive components is possible. That is why LTCC is used in many microwave circuits, where field effects are significant due to the low wavelength.

The process flow for fabricating LTCC structures is constituted by 4 main steps:

1. Preprocessing/mechanical structuring: individual sheets are cut into shape forming via holes, channels and other structures needed

2. Screen Printing: conductors and passives are screen printed onto the individual sheets and the via holes are filled

3. Lamination: the sheets are laminated using an uniaxial press and a fixture aligning each sheet

4. Sintering: the laminated substrate is sintered at a temperature of 850°C

The LTCC sheets used in this project have thickness of 0.3 mm and are fabricated from a composite material constituted by 50% alumina and 50% glass. Besides the ceramic materials the sheets contains a binding agent which provides the flexible behaviour the sheets exercises before sintering. During lamination the binding agent is joining the sheets such that the layers are merged into a single sheet. The composition of the binding agent varys depending on the supplier, and in the case of the LTCC we are using (CT 700 HERATAPE), the composition is confidential due to the policy of our supplier: Heraeus. When sintered the material has, according to the datasheet, a thermal expansion coefficient of $6.7 \times 10^{-6} \frac{1}{^\circ C}$ in the temperature range 25-300°C. This is close to value of silicon ($3.5 \times 10^{-6} \frac{1}{^\circ C}$), which makes this material suitable for bonding to silicon.

According to the datasheet a substrate shrinks by 14.4% for the length and width and 14.9 percent for the thickness when sintered. This means that in the design phase one has to scale the structures, including the print layout for the conductor layers. However, for the structures fabricated here the x and y dimensions (width and length) has been shrinking 15% (to 85% of their original value) and the z dimension (thickness) has been shrinking 21 - 23%. This is after lamination. The z dimension shrinks also during lamination process. Consequently, the z dimension shrinks to a final value of only 61.7 - 63.3% of its original value. See Table 5.3.

Number of layers	T_{BL} [mm]	T_{AL} [mm]	T_{AS} [mm]
2	0.60	0.48	0.37
3	0.90	0.75	0.57
5	1.50	1.20	0.94
8	2.40	1.89	1.50

Table 5.3: Measured thicknesses of the multilayered LTCC substrates fabricated in this project. The measurements are performed at each step in the process, using a vernier caliper. T_{BL}, T_{AL} and T_{AS} are the thicknesses before lamination, after lamination and after sintering respectively.

5.8 Prototyping

5.8.1 Lamination

In a regular process for fabricating LTCC substrates, the purpose of the lamination step is to assemble the preprocessed and already screen printed sheets of ceramic. Lamination is done applying a pressure of 270 bars in a uniaxial press, where the plates of the press are heated to 70°C to increase the mobility of the molecules of the binding agent. In this project we have utilized the lamination process both to get a substrate of the desired thickness for use in the micro milling processing, but also for assembling the milled parts afterwards. As mentioned earlier the total thickness of the laminated substrate is thinner than the sum of the thicknesses of the individual sheets before lamination. This is due to the fact that each sheet is compressed a little in the process. Likewise, it was unfortunately also not possible to maintain the z-dimension of the assembled micro thruster when performing the second lamination joining the two halves. Therefore attention was turned towards another method for the final joining of the parts of the thruster. For integrated thickfilm circuits a layer of cover glass is often applied on top of the entire substrate, in order to seal the circuit and to provide a protective layer. Hence, an idea came up to utilize this type of glass for the final joining of the parts of the micro thruster. This was implemented with great success, by screen printing a layer of the cover glass paste on top of one of the two halves of the thruster and subsequently joining the parts before finally sintering the entire structure. For integrating the glass frit with the LTCC thruster, it was attempted also to use cover glass paste for a lamination and co-fire the glas frit together with the LTCC. Although the lamination turned out very good, the glass frit lost its porosity during the heat treatment, as seen on Figure C.8 in Appendix C. Hence, instead the glass frit was applied after the sintering by epoxy glue. Later the problem with the glass frit loosing it porosity during heat treatment was solved by using quartz glass frit instead of borosilicate, but this in turn resulted in a bad lamination using the cover glass, since the LTCC is sintered well below the annealing point for quartz, which is around 1100°C.

5.8.2 Micro milling

At the DTU Nanotech - Department of Micro- and Nanotechnology a CNC (**C**omputer **N**umerically **C**ontrolled) micro milling machine is available. This machine facilitates milling of structures in PMMA polymer with very small cutting tools down to

25 µm in diameter. Since the LTCC material is soft prior to sintering, the milling machine is easily capable of processing this material as well as the polymer. To get at rigid substrate for milling, the desired number of sheets are laminated prior to milling (the lamination is described in Section 5.8.1). Hence the depth of the structures in the substrate no longer has to be a multiple of the thickness of a sheet, as for the regular use of the LTCC technology. From the 3D CAD models made in the software package SolidWorks, seen on Figure 5.15, a CAM (Computer Aided Machining) file is generated using the CAM extension software for SolidWorks. The micro milling machine available at DTU Nanotech is using so called G-Code for controlling its 3 slides for the x, y and z axes. G-Code is basically a long list of coordinates and feed rates, with interrupts every time a tool change is needed. Generating the G-Code for the milling machine, is done using the CAM extension SolidCAM. In SolidCAM the necessary tool paths are created using the geometry from the imported CAD model. For every feature of the model, separate operations are created where the tool paths are defined and most often different milling tools are selected for the different features. To save valuable operating time, different tool paths using the same milling tool are naturally put in sequence, since the upper level of the z-axis has to be reset for every tool change.

Creating a new operation, the type of milling operation is initially selected - eg. face milling, pocket milling, profile milling or 3D milling. The sequence in which the tool paths are created then reads:

1. Selection of geometry
2. Tool selection - type and size, eg. 0.5 mm End Nose Mill or Ball Nose Mill
3. Definition of required levels - eg. clearance level, upper level and pocket depth
4. Setting tool path characteristics - eg. contour, overlap, offsets and finish

Step down, which is the step in the z-direction for every machining, is for some types of operations chosen as part of the definition of levels and for other types as part of the tool path characteristics. Step down is most often limited due to the limited amount of material a certain milling tool is capable of cutting for every machining. But the step down can also be chosen due to a required finish, which is the case for our 3D milling. For the milling of the nozzles, which is done by 3D milling, a step down of 0.02 mm is chosen as compromise between processing time and surface definition, which is not improving notably for a lower step down. Otherwise for the other operations, we normally use a step down equal

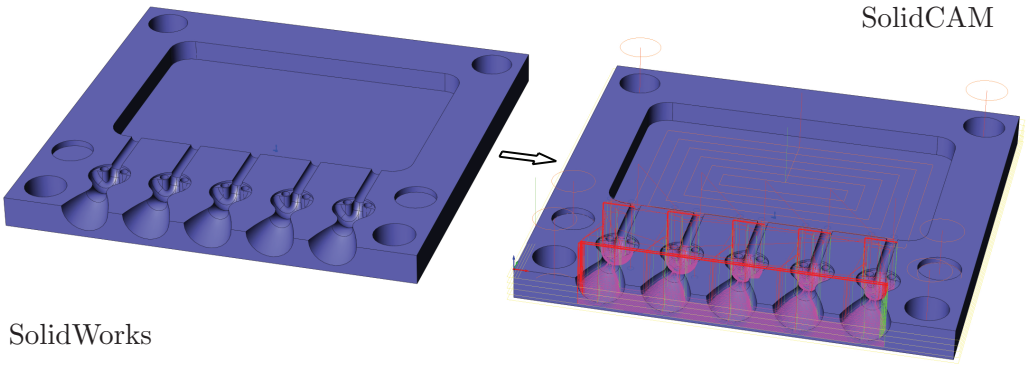

Figure 5.15: Generating so called G-Code for the CNC Micro milling machine, is done using the CAM extension for SolidWorks called SolidCAM. In SolidCAM the necessary tool paths are created using the geometry from the imported CAD model.

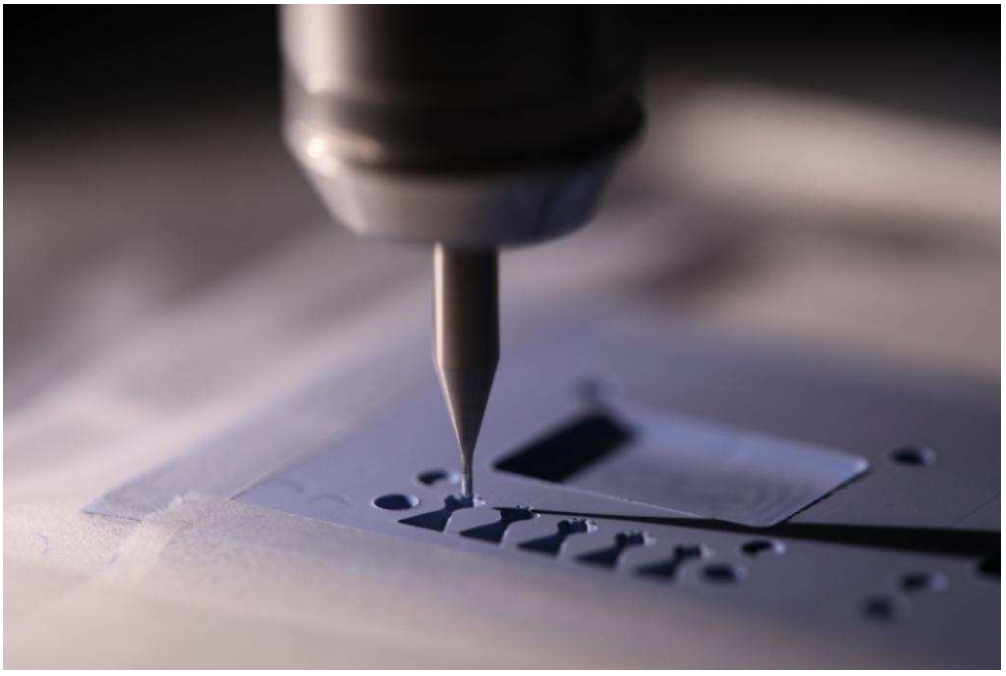

Figure 5.16: Micro milling of a LTCC substrate before sintering and after first lamination. The nozzles are cut by a Ø0.5 mm ball nose end mill.

to the radius of the tool, unless of course the desired depth is less. On Figure 5.16 a substrate is seen during milling of the nozzles of the first prototype. In addition to step down, it is also important to choose a proper spin rate for the tool of interest. The smaller the tool, the higher the spin rate. For the tools used in this project, we have used the following spin rates: 2 mm - 4000 rpm, 1.5 mm - 6000 rpm, 1 mm - 10000 rpm, 0.5 mm - 15000 rpm 0.250 mm - 20000 rpm and 0.1 mm - 28000 rpm.

As seen on Figure 5.16, the LTCC material is simply fixed by strips of tape

around the edges during milling, which is sufficient due to the minute forces induced by the small milling tools used here. The LTCC material is attached to a polymer substrate, which is mounted by double sided tape to the aluminum chuck of the machine. This prevents the milling tool from reaching the aluminum chuck. Polymer substrates are used for various attachments of the LTCC material to be milled. Hence, different polymer structures have been milled in this project as well. When milling the polymer it is important the milling tool is constantly wet in order to cool the tool, preventing the material from melting and getting stuck on the tool. When milling the LTCC, cooling is not critical, but it is an advantage to apply the air gun both to cool and to remove the shavings.

Milling the part with the capillary tubes for design D7, the tubes are initially drilled. Using pocket milling the substrate is subsequently machined utilizing an *End Nose Mill* such that small tubes extrudes from the substrate as seen on Figure 5.17 Top. Finally the sharp edges on the tubes are made using profile milling with a *Ball Nose Mill* as seen on Figure 5.17 Bottom. Fabricating the tubes for design D9, a much more complicated procedure is necessary. Due to the placing of the heating filaments, the part with the capillary tubes has to be devided in two halves, and consequently the tubes are milled using a *Ball Nose Mill* instead of being drilled. Initially the capillary tubes, the channels for the heating filament and the holes for the electrical connection are milled and drilled on a substrate. A special tool is then made for fastening the part perpendicularly for milling the sharp edges on the termination of the tubes. In order to prevent braking the edges during the milling, the processing of the tube terminations is done after the heating filaments are positioned and the two halves of the part are laminated and dried. In this way the part gains almost the same strength as for the part with the capillary tubes from design D7. Hence, after the lamination, the edges for the capillary tubes of design D9 is milled using the same procedure as the one seen in Figure 5.17.

For the design D13 the capillary tubes were downsized significantly and consequently it was assumed to be too complicated to use a wire as heating filament. Hence on this design the heating elements were integrated as thickfilm resistors constituting the very last part of the capillary tubes. The tubes was thus drilled through a single sheet of LTCC after thickfilm resistors had been printed on the sheet. In order to perform drilling and milling on a single sheet of LTCC (with a thickness of only 0.3 mm) a fixture was made from two polymer plates. A top plate with 4xM3 screw clearance holes was milled with a rectangular hole in the middle to make room for the drilling and milling tools when processing the LTCC sheet. In addition a bottom plate was made with 4xM3 tapped holes. Placing 4

screws in the holes, the LTCC sheet was then fixed between the two plates during processing.

Due to the long process sequence needed for producing screen print masks, as described in Section 5.8.5, it was attempted for the rapid prototyping to make screen print masks by CNC micro milling. Initially they were made from a piece of transparency placed between two PMMA polymer plates during processing, similarly to milling the LTCC sheet described above. However, this resulted in frayed edges due to flapping of the transparency, despite the fact it was fixed between the polymer plates. A much better result was attained from fixing the transparency by double sided tape. Initially this made the glue on the tape stick to the milling tool, but this was solved by applying the air gun with full pressure, which removed both the shavings and the glue.

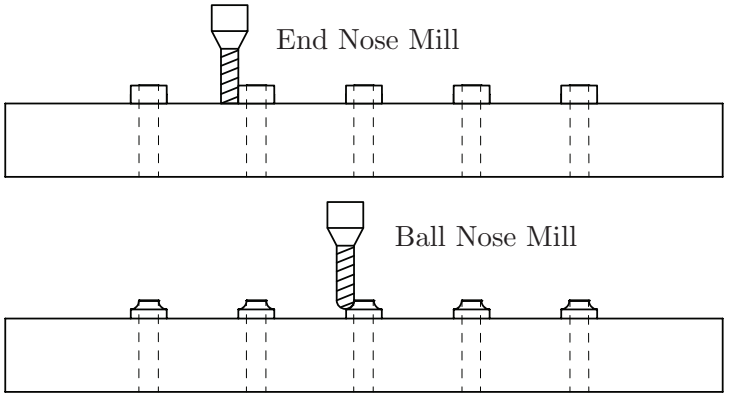

Figure 5.17: Milling the capillary tubes for design D7 and D9. For design D9, the LTCC is fastened in a specifically designed aluminum clamp, to fix the two laminated parts containing the metallic filaments.

5.8.3 Metallic Filaments

Initially it was decided to use a metallic filament as heating element. Accordingly, a conducting material with a high electrical resistance was needed. Immediately one turns the attention towards tungsten, which is used frequently in filaments for lighting purposes. Also nickel and a few other metals was considered. But testing their compatibility with the LTCC and more importantly the conductive paste used for establishing electrical connection, it was found that only platinum exhibited a satisfactory contact resistance while establishing a stable mechanical interface as well.

Since platinum is a very good conductor, it is not directly suitable as a heating filament, but is useful for the testing in atmospheric conditions since it is resistant

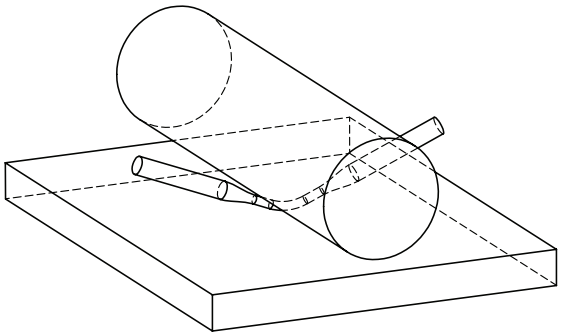

Figure 5.18: Thinning of the platinum filaments using a steel rod. See the result on Figure and B.2 in Appendix B

to corrosion. Hence, to increase the resistance of the platinum filament a the very tip where the heat is needed, a method for thinning the filament is applied. Placing the filament on a steel plate and using a circular steel rod to roll the filament back and forth while applying a gentle pressure on the rod, as seen on Figure 5.18, the diameter of the middle part of the filament is reduced from 0.15 mm to 0.10 mm, i.e. a factor of 2/3 of the original diameter, meaning that the resistance is increased by a factor of 2.25. In practice the resistance increased from 13mΩ to 25mΩ. On the latest prototype filaments where made by winding the platinum wire around a 0.6 mm rod using a lathe to turn the rod. The resistance was then increased to 65mΩ, but with the price of getting a larger evaporation chamber, meaning a longer start up time.

5.8.4 Thickfilm Resistors

Using the thickfilm resistors as heating elements, on design D13 and D14 the resistors are applied on a single sheet of LTCC to minimize their thermal contact with the rest of the substrate. Usually we use screen printing when applying conductors and resistors, but for some of the rapid prototyping the thickfilm paste is applied by a needle or a small paint brush, giving a worse edge definition obviously, as seen on Figure B.12 and B.13 in Appendix B. Testing the prototype based on design 13, while being heated above 100°C, an extreme increase in the resistance of the thickfilm resistors occurred (from $\approx 20\Omega$ to $\approx 500\Omega$) as the resistors gained contact with the fuel (both water and ethanol). This increase in resistance was irreversible. Only by re-firing the material, the resistance could be somewhat restored to a value of approximately 50Ω. This problem was found to be solved by applying a layer of cover glass before sintering, on top of a set of test resistors. However, testing the design D14 where the resistors where covered, the prototype suffered from the same malfunctioning as the D13. Hence, the problem might not

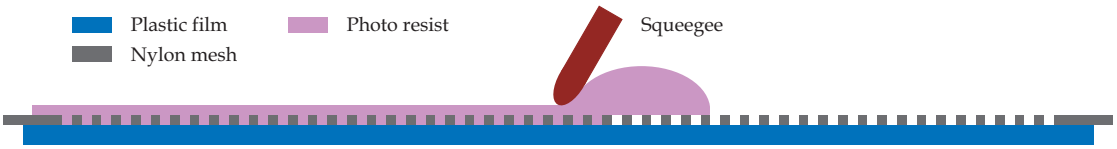

Figure 5.19: The resist is applied on the back of the mesh, while a thin piece of plastic film is placed on the front. The resist is dispersed by moving a squeegee back and forth 3-4 times.

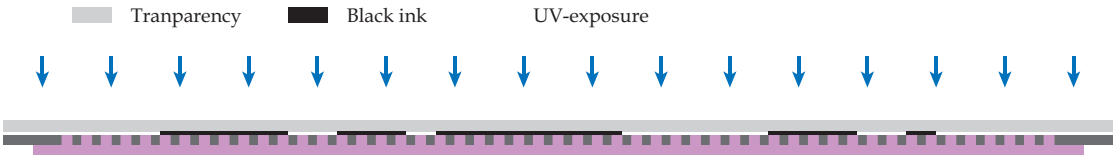

Figure 5.20: The plastic film is removed now that the resist is dry. With the ink on the transparency turning towards the mesh, the resist is exposed to UV-light for 10 min.

only be due to the fuel degrading the resistors, but also due to the high power being dissipated in those small resistors.

5.8.5 Screen Printing

Conductors are applied using silk screen printing where we have borrowed the thick film laboratory at DTU Electro. For this kind of conductor printing a stencil is made on a fine mesh and used as a screen for the printing. A polyester mesh with 325 threads per inch carried by an aluminum frame is applied a layer of photo resist, as illustrated on Figure 5.19. This is done by placing a thin piece of film on the front of the mesh, placing the frame on a table with the film turning downward and applying the resist on the back of the mesh moving a squeegee back and forth 3-4 times. In this way all the holes in the mesh gets filled with resist. Before performing exposure the frame with the mesh is put aside for drying for at least half a day.

Masks for the exposure of the mesh are printed on a piece of transparency by the company CB-Svendsen A/S. The resist used is negative, meaning that unexposed resist is removed during development. Consequently the black ink is printed on the transparency in the areas where the conductors are meant to be printed. The plastic film is removed now that the resist is dry and the mask is placed upon the front of the mesh with the ink turning against it, see 5.20. The resist is then exposed to UV-light for 10 min before it is developed showering the mesh with lukewarm water. A stencil with the pattern of the print layout then comes forward. See Figure 5.21.

Figure 5.21: The stencil is developed by showering the mesh with lukewarm water until the pattern to be developed clearly appears.

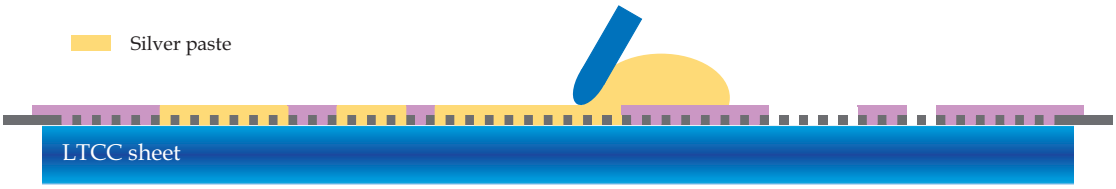

Figure 5.22: Silver paste is screen printed onto the LTCC sheet after a number of iterations has been performed printing an overlaying transparency to adjust printing pressure and alignment.

The screen printing is performed on a machine where the sheet is fixed on a vacuum chuck, which is positioned with respect to the stencil by two micrometer screws. The machine automatically moves a squeegee back and forth pressing the conducting paste through the stencil. See Figure 5.22. For the adjustment of the pressure on the squeegee and the alignment of the chuck, a piece of transparency is placed upon the LTCC sheet. The pressure on the squeegee is adjusted through a few iterations printing on the transparency, to get the entire pattern transferred optimally. Looking at the screen print on the transparency and the structures on the LTCC sheet below the transparency, the positions of the alignment marks on the two is noticed and the micrometer screws are adjusted accordingly. When the position of the screen print is satisfactory the transparency is removed and the LTCC sheet is printed.

Finalizing the screen printing process the printed sheets are dried in an oven at a temperature of 80°C for 15 min. The silver paste is observed to be absorbed by the sheets when they have been dried, see Figure 5.23. Consequently, the conductors on a LTCC substrate is very much in level with the surface of the substrate. After sintering the thickness of the conductors are measured by a profilometer, showing about 2 - 4 µm above the surface of the ceramic.

The experiments shows that it is possible to reach a tolerance on the line width of 20 µm, meaning that the conductors maximally gets 20 µm narrower than intended, as seen of Figure 5.24. The fact that the conductors always gets somewhat narrower than intended, can be due to lack of pressure on the squeegee or lack of paste on the stencil.

Figure 5.23: After the sheets has been drying for 15 min at 80°C, the silver paste is absorbed by the sheets and is almost in level with the surface of the sheets.

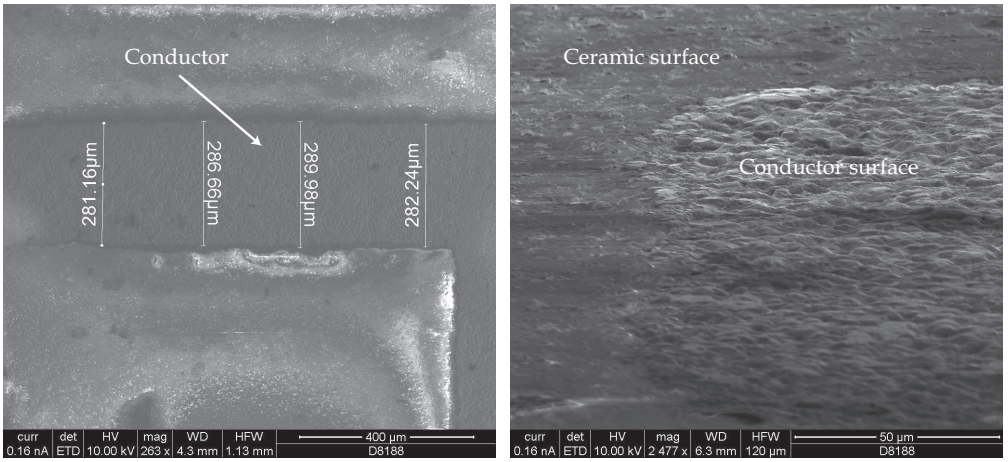

Figure 5.24: SEM image of conductors on an LTCC substrate after sintering. The conductor on the left hand image is designed to be 300 µm. The conductors are observed to be very much in level with the substrate surface, as seen on the right hand image.

5.9 Summary

Implementing the principle of a resistojet with a micropropulsion system, a concept providing a simple technique for controlling the fuel flow is suggested. With this concept in mind, an LTCC based resistojet microthruster is developed. The theoretical considerations necessary when dimensioning the microthruster and predicting its performance has been presented, and the theoretical performance in atmospheric conditions versus vacuum is compared. The different designs implemented during the prototyping is described, and the fabrication techniques utilized, along with the issues solved producing the individual prototypes, is presented. In this respect, the solution to the ever recurring problem of the fuel wetting the chamber and nozzle, was to implement a porous material for limiting the fuel flow. Two different ways for implementing thickfilm resistors as heating elements was developed, and the resistance of platinum filaments was successfully increased by either thinning the filament or winding a coil.

Chapter 6

Characterization

Since we have no vacuum chamber which could be immediately implemented for measuring the thrust directly, the characterization will focus on verifying the theoretical performance of the thruster in atmospheric conditions and to implement a promising principle for measuring micro-Newtons. Important parameters to characterize include:

1. Thrust level
2. Power vs. thrust
3. Startup and shut off charateristics
4. Fuel consumption, i.e. specific impulse
5. Thrust continuity and noise

6.1 Test Setup

Measuring forces in the microNewton regime is not an easy task. Building a test setup which has the extreme sensitivity needed, while being able to carry all the wiring, power supply, receiver and battery needed to drive the thruster has been troublesome. Due to this fact, many other research groups measure the secondary effect of the thruster, meaning the reaction force of the plume striking a probe. In this project we have used the same principle as Henry Cavendish used in 1797-1798 for measuring the gravitational constant. Hence, the thruster is placed on a horizontally oriented arm, which is suspended at the COM (center of mass) by a

glass wire mounted vertically to a very stable steel arm fastened to a concrete wall, thereby constituting a torsional pendulum. On Figure 6.1 the setup is illustrated as observed from above and it is seen how the thrust delivered by the device is transformed into an angular deflection of the glass wire, which becomes measurable firing a laser beam onto a small mirror.

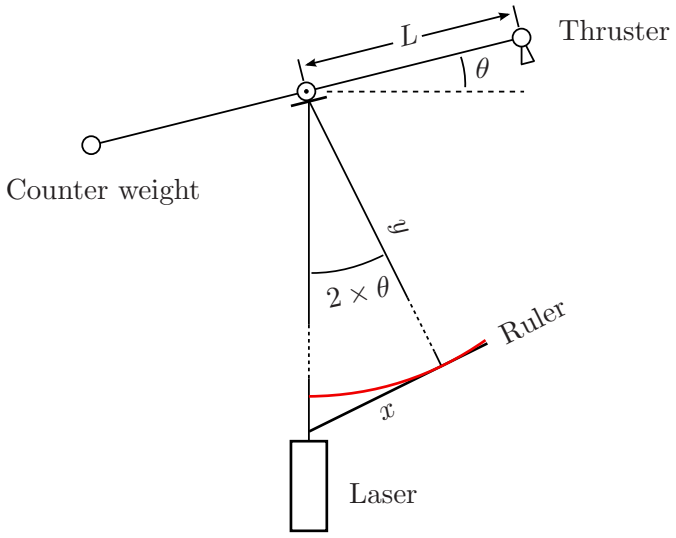

Figure 6.1: Sketch of torsional balance as it looks from above. A laser is fired onto a small mirror mounted on the horizontal arm, reflecting beam towards a stationary meter.

By knowing the torsional coefficient of the glass wire, the thrust can then be determined by measuring the angular deflection of the horizontal arm, when firing the thruster tangentially to the arm, thereby twisting the glass wire. Hence, for the relation between the angular deflection θ and the force/thrust F delivered by the microthruster, we have:

$$\theta = \frac{F \cdot L}{\kappa} \tag{6.1}$$

where L is the length of the arm, i.e. the distance from the thruster to the center of rotation, and κ is the torsional coefficient. For determining the angle θ we measure the position of the reflected laser spot on a ruler, which is placed a distance y from the mirror, as seen on Figure 6.1. Hence, the position of the laser spot will read:

$$x = y \cdot \tan(2\theta) \approx 2\theta y \tag{6.2}$$

This approximation is found to be good ($2\theta y > 99\% \cdot y \cdot \tan(2\theta)$) for a thrust less than 100µN. Consequently we have for the relationship between the thrust F and the position of the laser on the ruler x:

$$\frac{x}{2y} = \frac{F \cdot L}{\kappa} \quad \Leftrightarrow \quad F = \frac{x\kappa}{2yL} \tag{6.3}$$

6.1.1 Torsional Coefficient of the Torsional Balance

For the above described principle of measurement to work satisfactory, it is crucial that the torsional coefficient κ of the system is well known, since this parameter determines the sensitivity of the setup. Considering the system as a torsional pendulum, the torsional coefficient can be determined by measuring the period of oscillation of the pendulum. The period of oscillation relates to the torsional coefficient by [33]:

$$T = 2\pi\sqrt{\frac{I_C}{\kappa}} \tag{6.4}$$

And solving for κ we arrive at:

$$\kappa = I_C \left(\frac{2\pi}{T}\right)^2 \tag{6.5}$$

where T is the period of oscillation and I_C is the mass moment of inertia about the COM, which is defined as the sum of all the mass elements times their distance to COM squared, expressed by:

$$I_C = \sum_{i=1}^{N} m_i r_i^2 \tag{6.6}$$

In practice we determine the moment of inertia using a 3D CAD model of the setup seen on Figure 6.4. Hence, with the period of oscillation and the mass moment of inertia, we can determine all the dimensions of the setup, which will give a reasonable sensitivity.

6.1.2 Tensile Strength and Shear Modulus

Finding the suitable dimensions of the setup, a compromise between mechanical strength and sensitivity of the setup has to be found. Since we have chosen a glass wire for the pendulum, the practical limits on the length and diameter is very

much determined by how carefully it can be handled by the glassblower and other people handling the wire. Furthermore the limitation on how light the horizontal arm can be made, will put a lower limit on the diameter of the wire due to its tensile strength. Theoretical values of the tensile strength of borosilicate glass can be found to be as high as 6.5 GPa, but the practical strength lies around 27 MPa to 62 MPa, the reason being that glass is normally covered in microscopic cracks which generate local stress concentrations [34]. Using the tensile strength TS we can find the maximum allowable mass of the torsional pendulum for a given diameter of the wire, or the minimum allowable diameter for a given mass:

$$mg = TS \cdot A = TS \cdot \pi \cdot \left(\frac{d}{2}\right)^2 \quad \Leftrightarrow \quad d = 2 \cdot \sqrt{\frac{mg}{TS \cdot \pi}} \tag{6.7}$$

The wire we have acquired has a diameter ranging from 0.52 mm to 0.68 mm and a length of 645 mm. Hence, the wire can carry about 600 - 1300 g at the weakest point. The final total mass of the horizontal arm of the pendulum - including the joint, battery, receiver, controller and thruster - reached just below 1 kg (920 g), but the wire still sustained the weight.

To check if we arrive at a reasonable magnitude for the torsional coefficient, the shear modulus - which can be compared to a table value - for the glass wire is calculated by:

$$Z = \frac{8l\pi I_C}{T^2 r^4} \tag{6.8}$$

where l and r is the length and radius of the glass wire respectively. The length of the wire is measured to be 645 mm. Due to the fact that the diameter of the wire varies from 0.52 mm to 0.68 mm, the shear modulus is calculated as an average from 5 measurements of the diameter, distributed evenly over the length. These measurements reads: [0.68 0.64 0.59 0.53 0.52]. Hence, the experimentally determined shear modulus reads 24.5 GPa, which is 94% of the table value, reading 26.2 GPa.

6.1.3 Mechanical Design and Setup

The first issue that arises in the mechanical design of the above described setup, is how to fix the 0.5 mm glass wire in both ends. In order not to clamp directly onto the glass with the risk of crushing it, the wire is fixed inside a small epoxy

filled steel tube and centered applying a Teflon bushing as seen on Figure 6.2. A clamp consisting of two aluminum half parts - also seen on the figure - is then anchoring the steel tube applying four M5 bolts. The mechanical structure of the test setup is designed to be as stiff as possible and isolated from the surrounding environment, in order to minimize ambient disturbances. Consequently, the clamp carrying the glass wire and thus the whole torsional pendulum, is fastened to a strong steel arm which is mounted on a concrete wall.

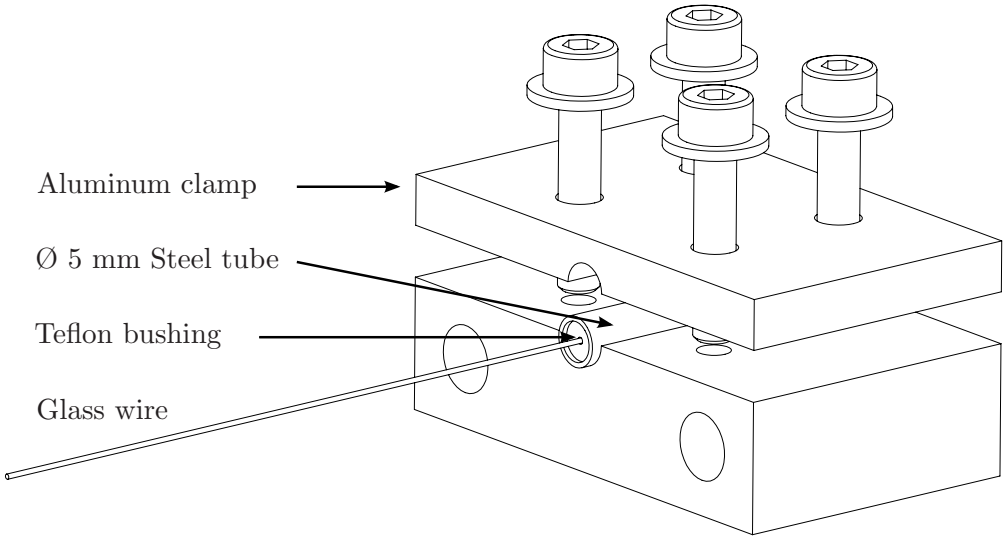

Figure 6.2: In order to be able to fix the glass wire without clamping directly onto the glass, the wire is protected by a steel tube filled with epoxy - fixing the wire inside the tube. To center the wire in the tube, a small teflon bushing is fitted inside the steel tube.

In the lower end of the glass wire, it is fixed inside another steel tube using the same technique as developed for the upper end. However, in the lower end the aluminum clamp has a different design, since the mounting onto the horizontal arm of the pendulum is very different from the mounting onto the steel arm in the upper end. Since the glass wire is only 0.5 mm in diameter, it is obviously very fragile to stresses trying to buckle it, arising from any imbalance of the horizontal arm. Obviously the horizontal arm should be counterbalanced to compensate for the mass of the microthruster, but as the fuel is being consumed during measurements, a small imbalance will yet emerge. Consequently, at the mechanical interface to the horizontal arm, a movable joint is integrated with the design of the lower end clamp, utilizing two ball bearings and a steel shaft as seen on Figure 6.3. The aluminum part constituting the interconnection between the joint and the horizontal arm, is designed to place the COM low to reduce the movement due to any imbalance, and the milled grooves are added to minimize its mass and thereby its contribution to the total mass moment of inertia. Finally the horizontal arm is made of carbon fiber, to obtain both low weight and stiffness. It has a

total length of 793 mm and is suspended at the center. Hence, the thruster is mounted on the horizontal arm applying a small adapter, in a distance of 385 mm from the center of the arm and thus from the rotational center of the torsional pendulum. Consequently, a thrust delivered by the microthruster of say $F = 10\mu\text{N}$ will produce a torque on the pendulum of $\boldsymbol{\tau} = \boldsymbol{r} \times \boldsymbol{F} \quad \Rightarrow \quad \tau = rF\sin(\phi) = 0.385\text{m} \cdot 10^{-5}\text{N} = 3.85 \cdot 10^{-6}\text{Nm}$, where ϕ is determined by the orientation of the thruster on the test setup and is chosen to be $\phi = 90°$ to maximize the sensitivity.

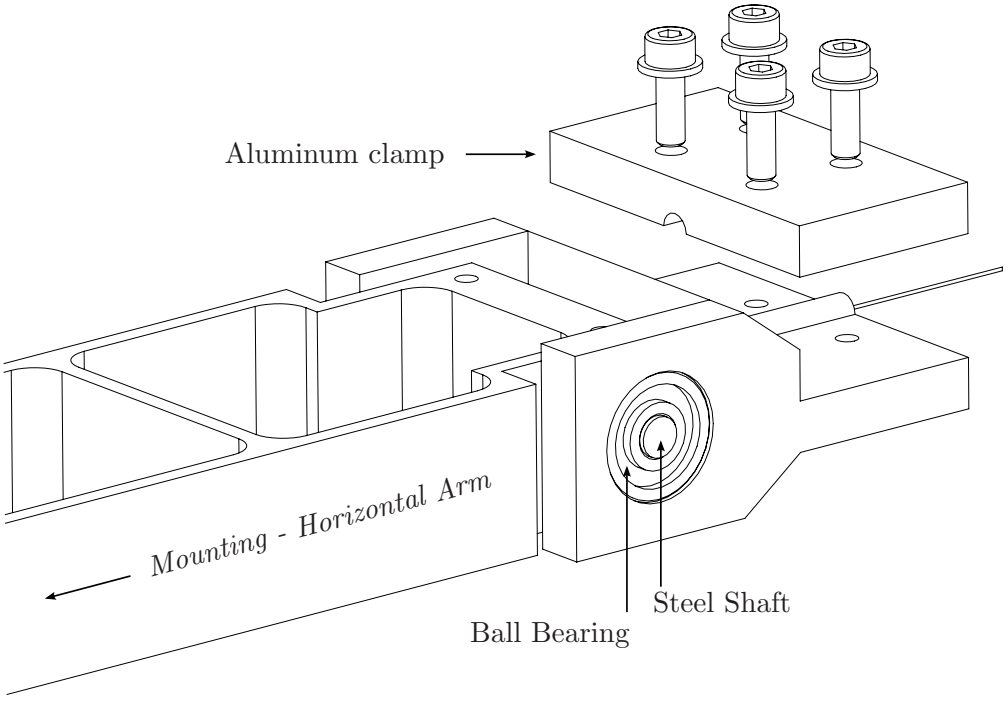

Figure 6.3: The mechanical interface to horizontal arm, is constructed to work as a self-balancer, by mounting the horizontal arm some 13 cm below a ball bearing joint.

To avoid turbulent air - originating from any movement in the laboratory - from interfering with the pendulum, a cover having no mechanical contact with the setup is constructed to shield the setup. This cover is made from polycarbonate glass, to make it possible to observe the behavior of the test setup while operating it. The final issue to be taken care of is the establishment of electrical connection from the power supply to the thruster mounted on the torsional pendulum. Here the challenge is to minimize the influence on the pendulum of the wires supplying the thruster. Hence, the wires are guided and attached only until the termination of the steel arm carrying the pendulum, from where they are left hanging freely and loosely all the way down along the glass wire until they are fixed on the horizontal arm close to the rotational center.

Figure 6.4: Image of the test setup. The horizontal arm is made of carbon fiber to minimize the weight and thereby the mass moment of inertia. In order to be able to balance out the setup, a low friction joint is made about 10 cm above the COM using ball bearings.

6.2 Power Supply

On the test setup fabricated in this project, it is crucial that the electrical connection to the thruster is affecting the mechanical properties of the torsional pendulum as little as possible, due to the minute forces we are measuring. The challenge using wires to supply the thruster, is to place them so that the pendulum would not have to twist them when oscillating. Accordingly the two wires needed to carry the current for the thruster, were left hanging loosely and only fastened on the horizontal arm at the very center. Using thick wires is preferable in order to keep the resistance low, since high current is needed for the thruster designs utilizing the platinum filaments. However, thick wires will influence the torsional coefficient more, therefore a compromise was chosen. But is was found to be too difficult to place the wires satisfactorily. Besides affecting the torsional coefficient of the pendulum, it was experienced that the heating of the wires occurring when putting current through them, made them move slightly and thereby twisting the pendulum.

Consequently, it was decided to use a dedicated power supply mounted on the horizontal arm with a dedicated battery, and controlling it remotely by radio. On Figure 6.4 the complete setup can be seen. The radio was a 2.4 GHz remote control, with 25 steps from zero to full throttle. Hence, the power supply was Pulse Width Modulated (PWM), delivering a constant voltage modulated at 1.56 kHz, such that every step on the remote control increased the pulse width by approximately 25 µs. For the battery, 3 LiPo cells (giving 11 V collectively), capable of delivering 32 A continuously, were used.

6.3 Test Results

The two prototypes of design D15 A and B respectively, are the ones used for the performance tests. Since we are using a remote controlled power supply, it is not immediately possible to read out the power consumption directly. Hence, the power consumption is determined from the position of the throttle on the remote control. Initially precise measurements of the resistance of the individual filaments is acquired. Then an IV-characteristic is obtained of the thruster including wiring to determine the resistance of all the connections to the filaments. Using these measurements it is possible to determine how much power is dissipated in the filaments only. For the design D15A we have a resistance of ≈ 13 mΩ per filament and for the D15B we have ≈ 65 mΩ at 100 mA. As seen on the IV-characteristic

for the D15B, the resistance increases with the power due to the heating of the filaments, which has a temperature profile given by:

$$R_T = R_0(1 + A \cdot T + B \cdot T^2) \tag{6.9}$$

where $A = 3.9083 \cdot 10^{-3}$ and $B = -5.775 \cdot 10^{-7}$ for platinum. Hence, by looking at the temperature dependency of the resistances, an estimate can be made on the temperature in the chambers during operation.

The measurements we have at this point are very limited. But two measured thrust curves have been achieved for atmospheric pressure so far, which seems to be quite linear, as seen in Figure 6.5. The thrust to power ratio turns out to be about 50μN/W, which is more than half of the theoretically expected value, meaning that about 45% of the power consumption is lost. The specific impulse was measured several times for both design D15A and D15B, and for both of them the I_{sp} lies around 1 second, which is also in the same order of magnitude as predicted for atmospheric pressure. Furthermore the rise time was measured to be approximately 30 seconds for 0 to 40μN, and the tail off time going back from 40μN to 0 was about 5 seconds.

Finalizing the characterization of the thruster developed in this project, a sequence of tests lie ahead. Together with the thrust to power ratio and specific impulse, the following properties characterizes a microthruster:

- Thrust rise time: Time it takes for the system to go from zero thrust to full thrust.
- Thrust tail off time: Time it takes for the system to go from full thrust to zero thrust.
- Throttling capability or Thrust Magnitude Control (TMC): The capability to control/change the thrust of an individual thruster given as a percentage of nominal thrust; For example, a throttling capability of 50% means that the thrust can be reduced to 50% of its nominal value.
- Minimum impulse bit: Smallest achievable impulse for a single burn
- System specific impulse: Defined as the total impulse delivered per unit propulsion system weight and is typically expressed in seconds. The system specific impulse shows that to deliver a certain total impulse we should seek

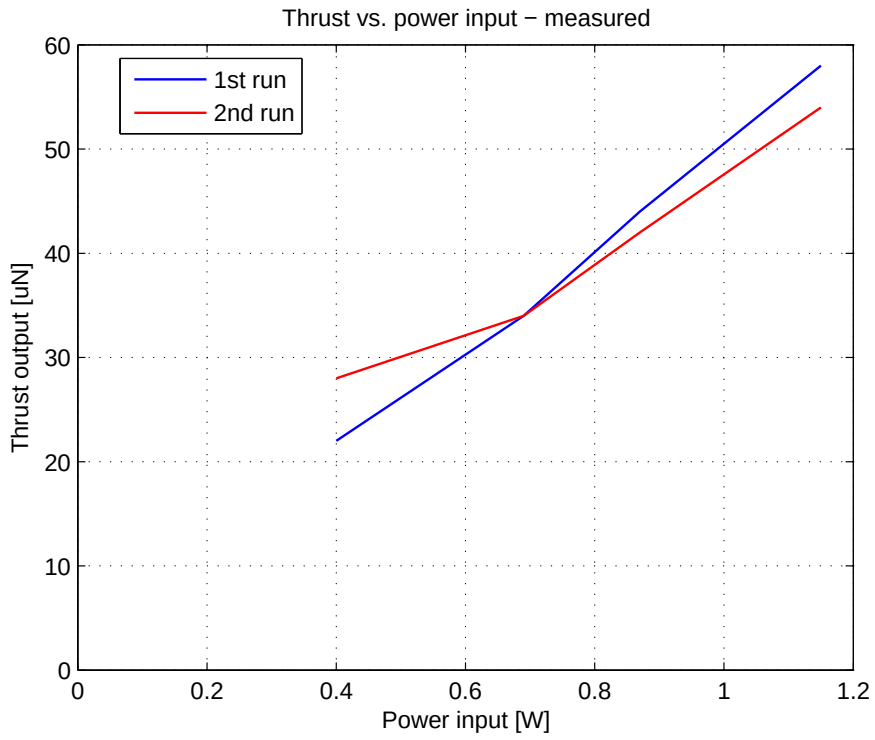

Figure 6.5: Measured thrust versus power for atmospheric pressure. The thrust curve seems to be quite reproducible and the thrust to power ratio is in the same order of magnitude as the theoretical, and somewhat lower as expected, due to power loss through conductance and thermal radiation.

to minimize propulsion system weight. As such, it is an important comparative measure of the efficiency of a propulsion system; The higher its value, the better the performance of the system. It is noted that some rocket scientists divide by mass instead by weight thereby expressing system specific impulse in meters/second rather than in seconds.

- Volumetric specific impulse: The total impulse delivered per unit of propellant volume. The higher the value, the smaller the size of the propellant storage and hence the spacecraft. High volumetric specific impulse requires high specific impulse and a dense propellant. Instead of the volumetric specific impulse one can use propellant density and (gravimetric) specific impulse.

- (Cumulative) life span: The total life (burn time) of the motor expressed in seconds or hours.

- Duty cycle: The nominal (single) burn time of the motor expressed in seconds.

- Pulse duty cycle: The duration of a pulse versus time in between two pulses expressed as a percentage (%). Especially at very short burning times and low duty cycles the pulse is too short to attain a situation of equilibrium in the motor and combustion will be incomplete. In addition, heat losses will have much effect, causing a low burning efficiency and hence a low specific impulse.
- Motor mass: The mass of the motor dry (without propellants in the lines) expressed in kilogram (kg).
- Thrust-to-weight ratio: A dimensionless factor expressing the ratio between the vacuum thrust and the weight of the motor; The higher the value, the better the accelerating properties of the motor.
- Thrust noise: A measure of how stable the thrust is.

6.4 Summary

A test setup is developed utilizing the principle of a torsional balance, to transform the thrust delivered by the devices into a measurable parameter. Hence, the thruster is placed on a horizontally oriented arm, which is suspended at the COM (center of mass) by a glass wire mounted vertically to a very stable steel arm fastened to a concrete wall. Using this setup, the thrust vs. power is measured, as well as specific impulse and rise time / tail off time. The measured results shows to be in well agreement with the theoretical predicted values for thrust to power ratio and specific impulse. Other relevant characteristics to measure in the future reads: Throttling capability, Minimum impulse bit and Thrust noise.

Chapter 7

Outlook

Starting up the study on micropropulsion, we have investigated the problem to be solved and we have presented a method for compensating the disturbances on a spacecraft in LEO. The following chapter gives an outlook of the work to be done in continuation of this project, in order to finalize and improve the system.

7.1 Disturbance Forces

Studying the space environment and its influence on formation flying spacecrafts, an area which is a primary concern but only treated briefly in this thesis, is the differential gravity on the spacecrafts. We have shown the equations of relative motion between spacecrafts assuming perfect Keplerian orbits of the spacecrafts, but how to model the differential forcing due to gravity is not treated. Modeling the differential forcing, it is important to consider the perturbations of the Earth's gravitational field. Most important is the inclusion of the second-order zonal coefficient (J_2), discussed in Section 3.5 Chapter 3, providing an analytical solution to the relative motion of formation flying spacecraft in the presence of an oblate Earth.

Taking into account the residual magnetic torque, is also highly relevant when disturbances from the space environment in LEO is considered. This torque is produced by the interaction of the Earth's magnetic field and the satellite's residual magnetic field. Hence, this disturbance will be very different from one mission to another, dut to its dependency on the magnetic properties of the materials of which the spacecraft is contructed. For satellite construction any conductive or

magnetized material where it is possible should be replaced with less conductive equivalents in order to reduce the torque generated.

Due to lack of characteristics for the MICROSCOPE mission, we had to make som rough assumptions on the drag coefficient, surface area and reflective coefficients. With more knowledge about these, a better model could have been made for MICROSCOPE. Looking at the solar radiation pressure, is furthermore interesting for drag free missions in general, to consider the time constant as the satellite enters and leaves eclipse.

7.2 Micropropulsion System

7.2.1 Hyperacuity

A complete accelerations and attitude control system for formation flight utilizing micropropulsion, needs sensor techniques which can determine the intersatellite distance and attitude with extreme accuracy. The VBS has shown to be superior for formation flight, and can most certainly be enhanced further for this application. One way of doing this is by improving the algorithms used to perform the *Hyperacuity*, utilized by the star tracker platform. Two light sources imaged on a CCD (Charge Coupled Device) can be resolved only if their separation leaves at least one pixel with a detectably different intensity, otherwise the pattern is indistinguishable from a single elongated light source. However, two targets can be localized relative to each other to values transcending the spacing of the pixels; this hyperacuity mechanism achieves this by identifying, with sub-pixel precision, the light center of each target, across all the pixels it covers. Improving this mechanism on the VBS, could perhaps give an even better pointing accuracy.

7.2.2 Thruster Completion

This project has only reached a proof of concept of the implementation of the principle of a resistojet for a microthruster. Hence, more research and development should necessarily be put into this principle to reach a system ready for space flight. Regarding the microthruster fabrication done in this project, the integration of the glass frit with the LTCC could be improved. In this project the glass frit was integrated after sintering the thruster body, by using epoxy glue. This might not be suitable for space application, and also puts a limit on the allowed operating

temperature. Another way to integrate the glass frit, is to design the thruster body and to dimension it in a way, such that the shrinking of the LTCC material is utilized to seal and fasten the glass frit. This of course would require the use of quartz glass frit, which was found to be resistant to the temperature conditions during sintering.
Unfortunately the thickfilm resistors integrated with design D13 and D14, was never tested successfully on a prototype. This is most likely due to the high power needed to provide a measurable thrust in atmospheric conditions, but is still considered the most elegant and reproducible way of implementing a heating element. Further research into this, is therefore attractive.

At this point the only drawback of the concept developed here, seems to be that we are dependent on having a valve between the fuel reservoir and the glass frit transporting the fuel the last stretch before it enters the evaporation chambers. This is to prevent fuel from leaking when the thruster is off, due to the hydrophillic properties of the glass frit, which maintains a wet surface at the entry point for the evaporation chambers and thus results in evaporation from the surface of the glass frit. However, two solutions to this issue might be implementable. One is to use a fuel which is phobic to the glass frit and another is to make a surface treatment of the glass frit making it hydrophobic. This would simplify the concept even further.

7.2.3 Testing, Qualification and Characterization

The crucial experiment to perform to prove this concept for a microthruster is suitable for space applications, is a vacuum test. Testing the performance in vaccum by measuring the thrust directly, is not an easy task, and the work done is this project has only made it more clearly how hard it is to measure forces in the microNewton regime. This was learned using the test setup described in Chapter 6, where only the heating of the wires supplying the thruster was enough for disturbing the measurements. Also electrostatic attraction was experienced several times, when the pendulum came too close to nearby objects. However, a preliminary vacuum test, validating the method suggested for controlling the mass flow, could be performed simply by placing a fuel reservoir sealed with a disc of glass frit (making the fuel reservoir penetrable only through the glass frit) in a vacuum chamber, and measure the mass flow leaving the reservoir.
For making a full vacuum test, measuring the thrust directly, a scaled down version of the setup used so far could be made to fit a vacuum chamber. However, instead of using the laser setup for reading out the displacement of the pendulum, the

principle of an electrostatic accelerometer could be utilized. Hence, one of two plates to be charged is placed on the horizontal arm of the pendulum as close as possible to one end, and the other plate is placed in its vicinity but fixed to the surroundings and not to the pendulum. In the other end of the horizontal arm, the thruster is mounted, and consequently the thrust can be measured by measuring the electrostatic reaction force necessary to maintain the distance between the two electrodes (plates). Alternatively, the displacement of the pendulum could be measured by using laser interferometry.

Chapter 8

Conclusion

Looking at current and future space missions utilizing precision controlled space flight, we have seen the relevance of this project and the long term perspectives of the technology developed here. The objective of the study of this thesis, was to develop a method by which an entire, efficient, control system enabling precision formation flight can be realized. This objective has been achieved. Hence, a model has been derived for deducing the requirements for a micropropulsion system, by studying the space environment, and applicable sensor techniques for determining the impact of the disturbances from the space environment, has been investigated. Finally, a promising candidate for a micropropulsion principle was chosen and implemented with success, using microfabrication technology combined with multilayered ceramics technology, more specifically LTCC. The key element to success was the investigation on porous materials, were we became aware of a material utilized extensively in the field of chemistry, knows as sintered filter discs or glass frit.

From the modeling of the disturbance forces on the MICROSCOPE spacecraft, reading atmospheric drag and solar radiation pressure, the requirements for a micropropulsion system being utilized for realizing drag free space flight was deduced. It was found here that the most significant disturbance on MICROSCOPE will be the atmospheric drag, both regarding magnitude and time constant. The magnitude of the atmospheric drag can become as high as ≈ 130 μN during times with high solar activity. This is due to the fact that the increased solar radiation present during high solar activity, heats up the atmosphere and can increase its density with 2-3 orders of magnitude. By comparison the worst case scenario for the solar radiation pressure, was a magnitude of ≈ 20 μN. Furthermore the worst case time constant (or rate of change) on the atmospheric drag, was found to be ≈ 40 μN/min. For the solar radiation pressure, the y and z components are

very small and neglectable compared to the x component, since MICROSCOPE is turning the face with solar panels towards the sun at all times. Hence, the time constant on the SRP is all in all neglectable, since the time constant on the x component is determined only by the slow precession of the satellite orbit with respect to the sun. Furthermore, the MICROSCOPE satellite only gets into eclipse around winter solstice and therefore no experiments are conducted during those times, since the SRP obviously varies a whole lot in this situation.

Due to the engagement of our department in the PRISMA mission, where our VBS Visual Based Sensor system is a primary payload, our department possesses an extensive knowledge and experience regarding sensor techniques for formation flight. On PRISMA, 3 systems are tested, where the VBS has shown to be the most promising technology so far, with a lateral accuracy better than 0.1 mm and an accuracy on the distance of 0.5 mm, both measured at a 5 meter distance to the target. Hence, developing a complete control system utilizing micropropulsion together with the VBS technology, seems very tempting. Investigating different known principles of propulsion and ranking them with respect to each other, the principle of a resistojet was considered the most promising candidate for building a simple and reliable downscaled thruster. Consequently, we developed a concept for a micropropulsion system utilizing a very simple principle for controlling the fuel flow into the evaporation chambers. In our concept this is done by controlling the pressure in the fuel reservoir by heating the reservoir with an eletric heating element. The capillary channels embedded in the applied porous glass frit then limits the flow into the chambers. Hence, the range within which the flow should be controlled, can be adjusted to comply with the ambient operating pressure, by choosing the appropriate porosity of the glass frit and optimizing its thickness.

The developed concept was then implemented using LTCC ceramic technology, which facilitates extremely useful fabrication techniques like micromilling and laser cutting. In this project the LTCC technology together with micromilling, was used to fabricate 3D converging diverging Bell nozzles for optimal performance. The heating elements was then integrated with an element for each chamber and nozzle, using both thickfilm technology and platinum filaments, facilitating the control of the thrust on each nozzle individually. Unfortunately the thickfilm resistors suffered from rapid disintegration, increasing their resistance irreversibly, when being in contact with either water or ethanol at high temperatures. This was solved by applying a layer of cover glass, but still, when producing the small thickfilm resistors integrated with our thrusters, they malfunctioned most probable due to the high power demand of the thruster, when operating in atmospheric pressure.

The measurements we have at this point are limited. But the thrust to power ratio has been measured and reads about 50 μN/W, i.e. 55% of the theoretically expected value. The specific impulse was measured for both design D15A and D15B, and for both of them the I_{sp} lies around 1 second, where the theoretically predicted ISP for atmospheric pressure is 1 - 3 seconds. Furthermore the rise time was measured to be approximately 30 seconds for 0 to 40μN, and the tail off time going back from 40μN to 0 was about 5 seconds. Consequently, this project has performed a proof of concept of the miniturization of the resistojet principle for delivering a thrust in the microNewton regime. And this principle seems to offer a simple, reliable and fairly effective method for realizing a micropropulsion system.

Bibliography

[1] http://www.esa.int/Our_Activities/Observing_the_Earth/The_Living_Planet_Programme/Earth_Explorers/Swarm/Objectives

[2] http://www.space.dtu.dk/English/Research/Projects/Swarm.aspx

[3] http://spaceinimages.esa.int/Images/2012/03/Swarm

[4] http://www.space.dtu.dk/Forskning/Projekter/GRACE.aspx

[5] *PROBA 3 - Science Management Plan*, 24 June 2009

[6] http://www.cnes.fr/web/CNES-en/2983-myriade.php

[7] D. Nicolini, L. Ceruti, B. Kent, G. Santangelo, L. Serafini, N. Solway, *Micro-propulsion Subsystem Developments For Drag-Free Spacecraft*

[8] http://lisa.nasa.gov/

[9] *The Science Case for LISA Pathfinder*, http://www.rssd.esa.int/SP/LISAPATHFINDER/docs/LPF_Science_Case.pdf

[10] http://www.esa.int/Our_Activities/Observing_the_Earth/GOCE/Satellite

[11] http://spaceinimages.esa.int/Images/2008/03/Solar_panel_inspection

[12] S. D'Amico, E. Gill, O. Montenbruck, *Relative Orbit Control Design For the Prisma Formation Flying Mission*

[13] Karsten Grossekatthöfer, Zizung Yoon, *Introduction into quaternions for spacecraft attitude representation*

[14] Wertz, James R., *Spacecraft Attitude Determination and Control*, D. Reidel Publishing Company, Dordrecht, Holland, 1997.

[15] Bong Wie, *Space Vehicle Dynamics and Control*, American Institute of Aeronautics and Astronautics

[16] Sidi, Marcel J., *Spacecraft Dynamics and Control*, Cambridge University Press. 1. Edition, 2001

[17] Liu and Lühr, *Thermospheric mass density variations during geomagnetic storms and a prediction model based on the merging electric field*

[18] http://en.wikipedia.org/wiki/Drag_coefficient

[19] John Leif Jørgensen, Mathias Benn, *VBS - The Optical Rendezvous and Docking Sensor for PRISMA*

[20] P. Touboul, M. Rodrigues, E. Willemenot and A. Bernard, *Electrostatic accelerometers for the equivalence principle test in space*

[21] http://www.lsespace.com/

[22] Jean-Francois Roussel, Thomas Tondu, Jean-Charles Matelez, Enrico Chesta, Stephane DEscrivan, and Laurent Perraud, *Modeling of FEEP Plume Effects on MICROSCOPE Spacecraft*, IEEE TRANSACTIONS ON PLASMA SCIENCE, VOL. 36, NO. 5, OCTOBER 2008

[23] J. Mitterauer, *Micropropulsion for small spacecraft: a new challenge for field effect electric propulsion and microstructured liquid metal ion sources*, Vienna University, Puplished online in Wiley InterScience

[24] Manuel Ruiz Delgado, Radiation Pressure *Modeling the Space Environment*, European Masters in Aeronautics and Space, E.T.S.I. Aeronáuticos Universidad Politécnica de Madrid, April 2008

[25] Online report, *"Solar wind - magnetosphere coupling and the terrestrial impact"*

[26] Peter Fortescue, John Stark, Graham Swinerd, *Spacecraft Systems and Design*

[27] Tsung-Hsun Lu, Po-Yuan Chiu and Ming-Hsun Wu, Department of Mechanical Engineering, National Cheng Kung University, Tainan, Taiwan, *Development of Pulsed Detonation Micro Thruster Using Low Temperature Co-fired Ceramic Tape Technologies*

[28] Henrik Bruus - DTU Nanotech, Oxford University Press 2008, *Theoretical Microfluidics*

[29] M. A. Othman, A. E. Makled, *Evaluation of Resisto-Jet Thruster Engineering Model for Space Application*

[30] Yoshihiko Imanaka, *Multilayered Low Temperature Cofired Ceramics (LTCC) Technology*, Fujitsu Laboratories Ltd., Japan

[31] Prof. P. Ryser, *Introduction to LTCC for Engineers*, Thick-film Technology Group, Laboratorie de Production Microtechnique, Sep 2006

[32] Palles-Areny, Webster, *Sensors and Signal Conditioning*

[33] Gunnar Christiansen, Erik Both, Preben Østergaard Sørensen, *Mekanik*, Departement of Physics, Technical University of Denmark

[34] http://www.roymech.co.uk/Useful_Tables/Matter/Glass.html

[35] Jay McMahon, Daniel Scheeres, *Secular orbit variation due to solar radiation effects: a detailed model for BYORP*

Appendix A

Theoretical Plots

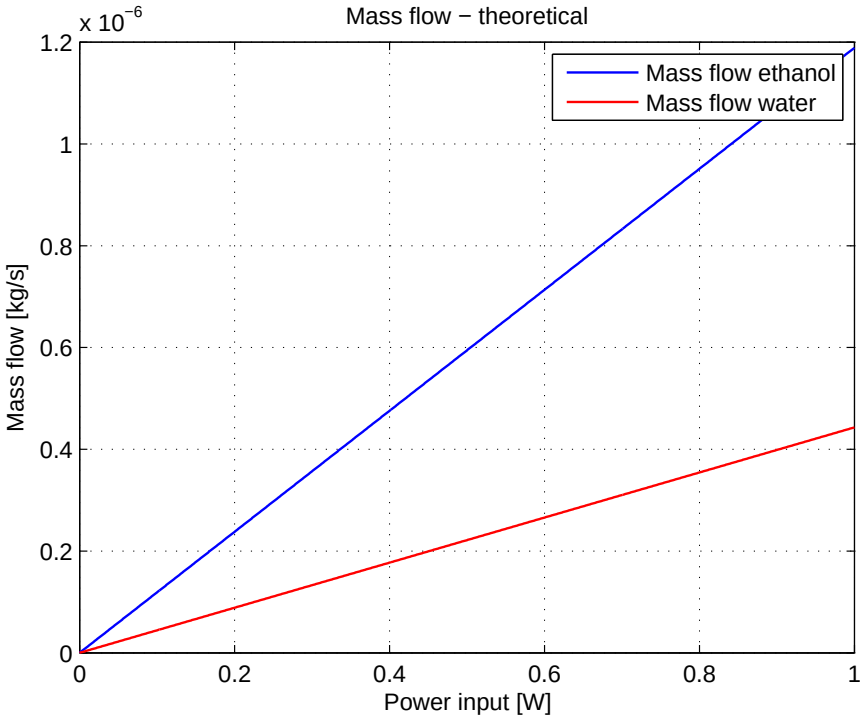

Figure A.1: Theoretical mass flow in atmospheric pressure

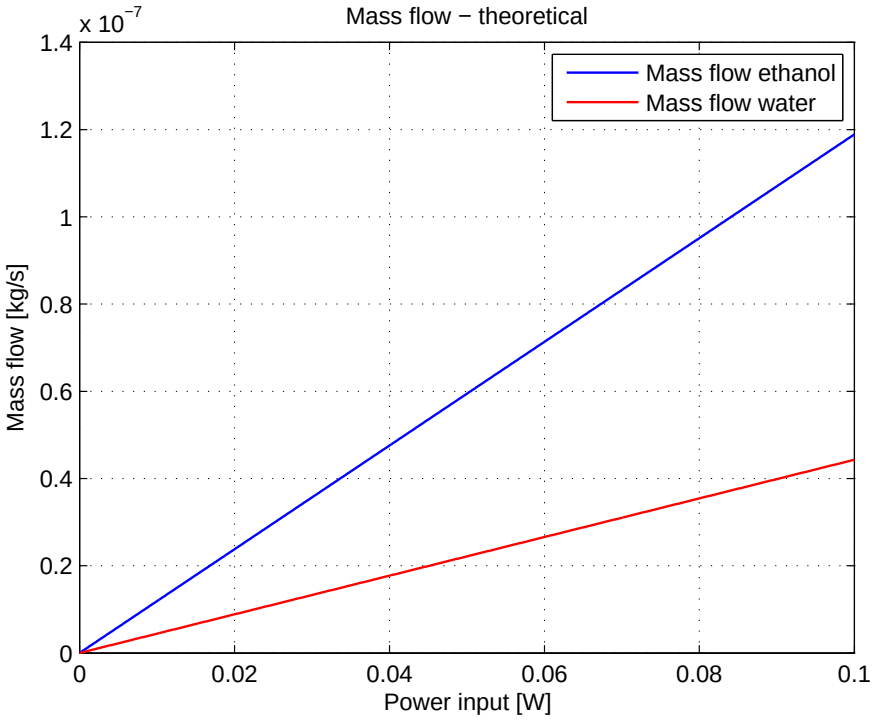

Figure A.2: Theoretical mass flow in vaccum

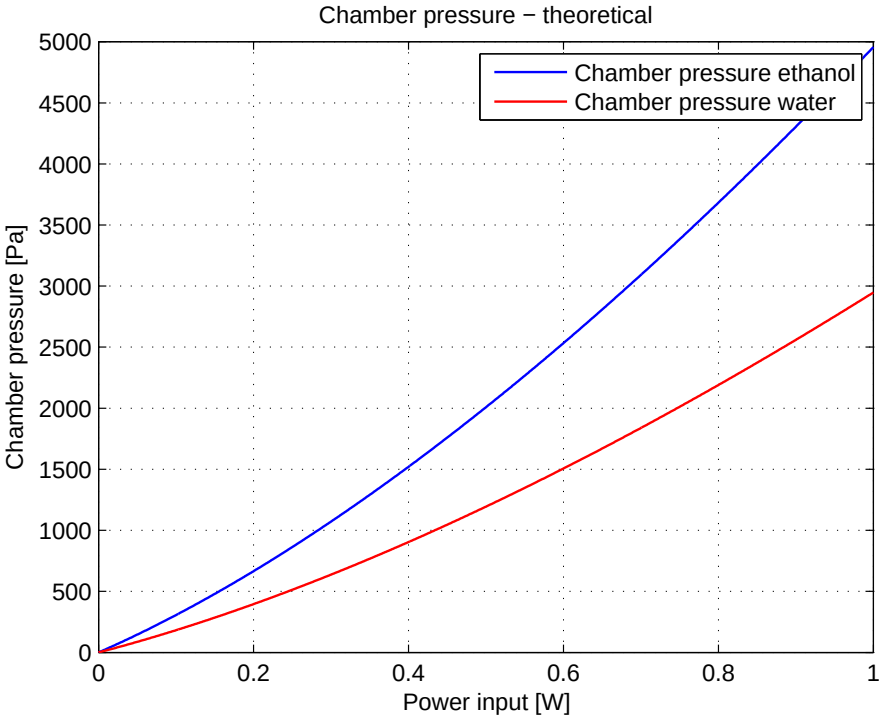

Figure A.3: Theoretical chamber pressure in atmospheric pressure

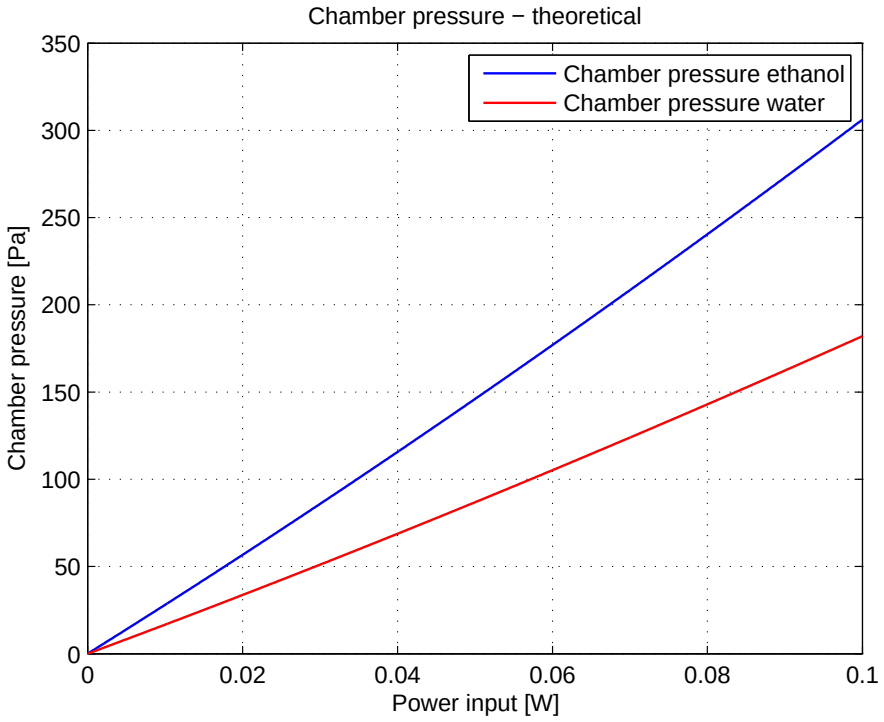

Figure A.4: Theoretical chamber pressure in vacuum

Appendix B

Pictures From Prototyping/Fabrication

B.1 Design D4

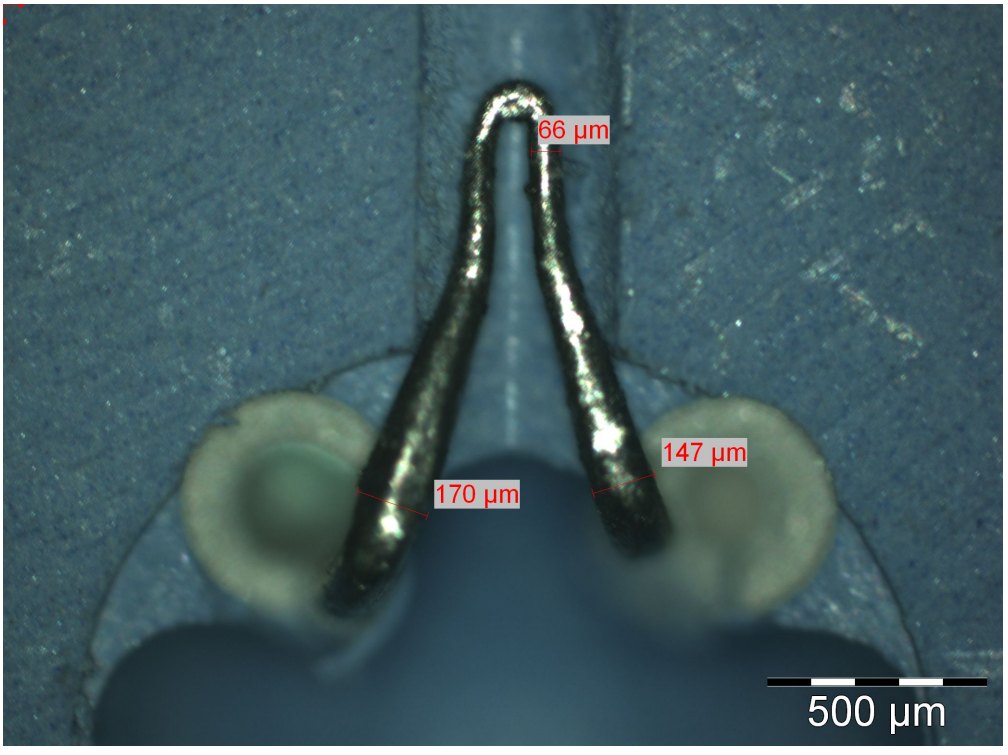

Figure B.1: Design D4 heating filament

B.2 Design D5

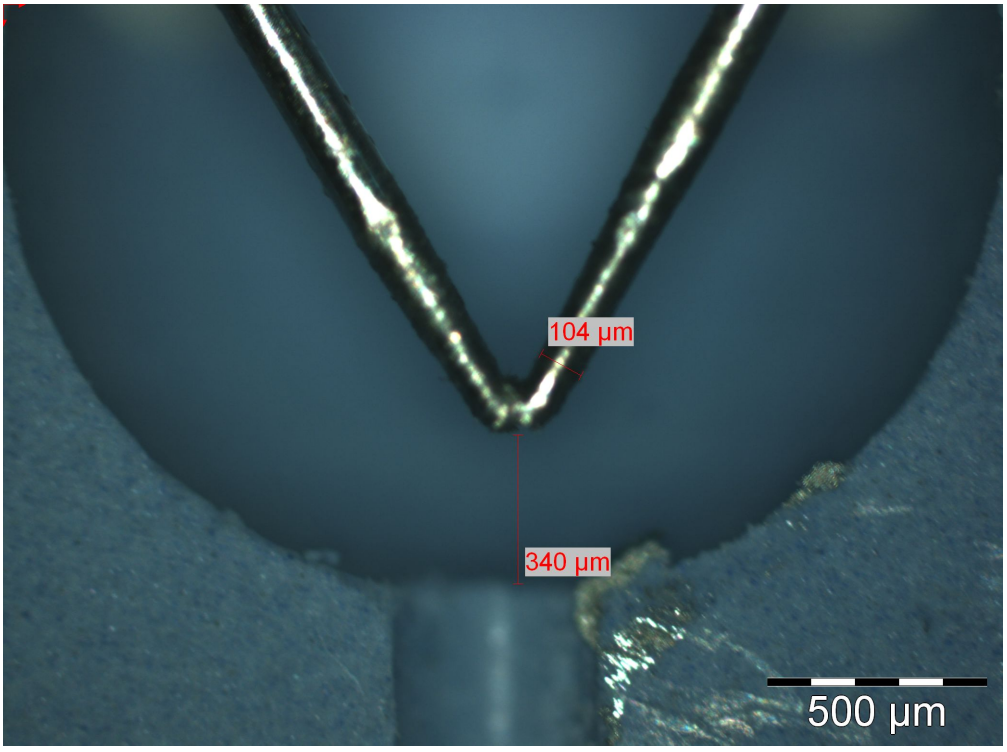

Figure B.2: Design D5 heating filament

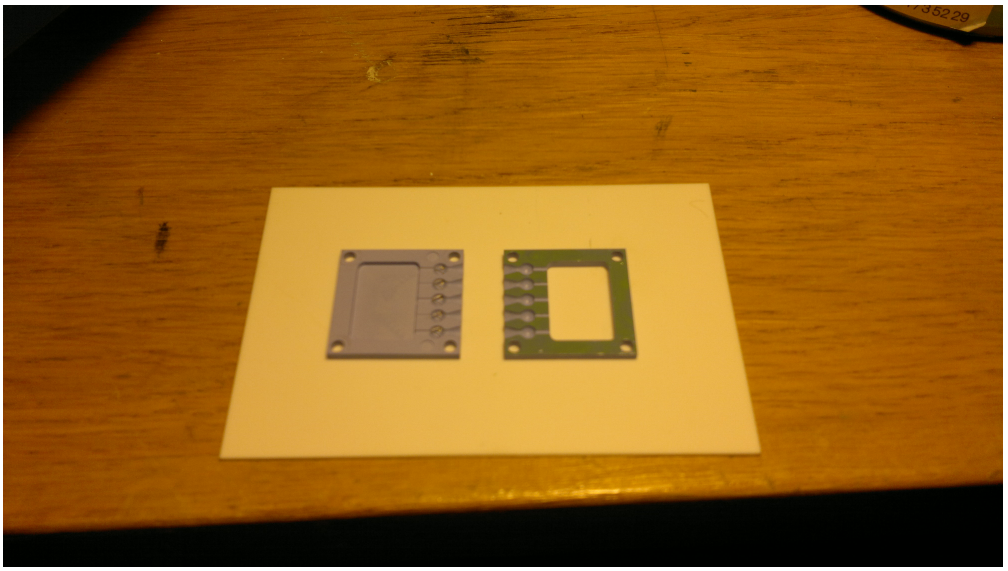

Figure B.3: Substrates just before assembling/lamination

B.3 Design D7

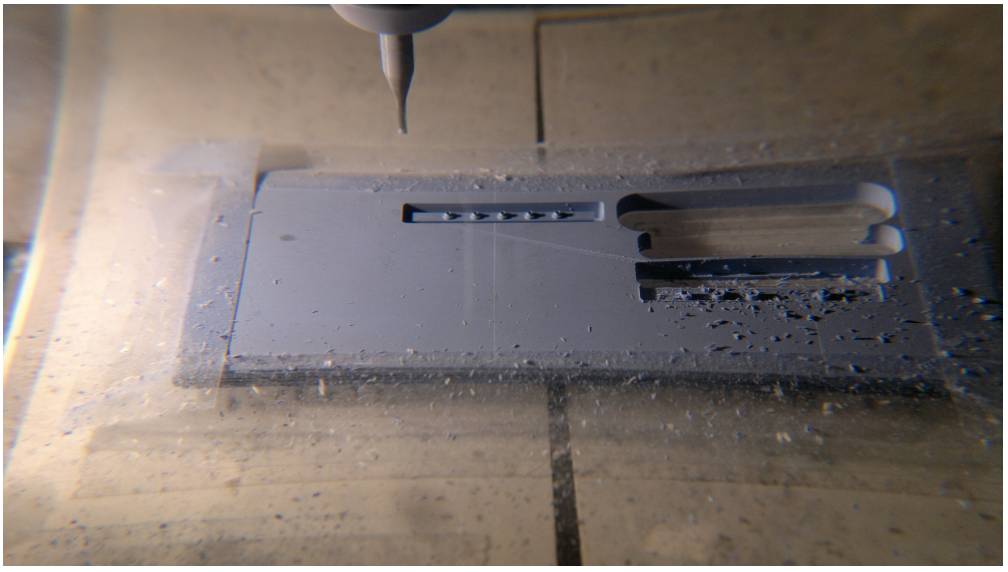

Figure B.4: Fabricating capillary tubes for Design D7

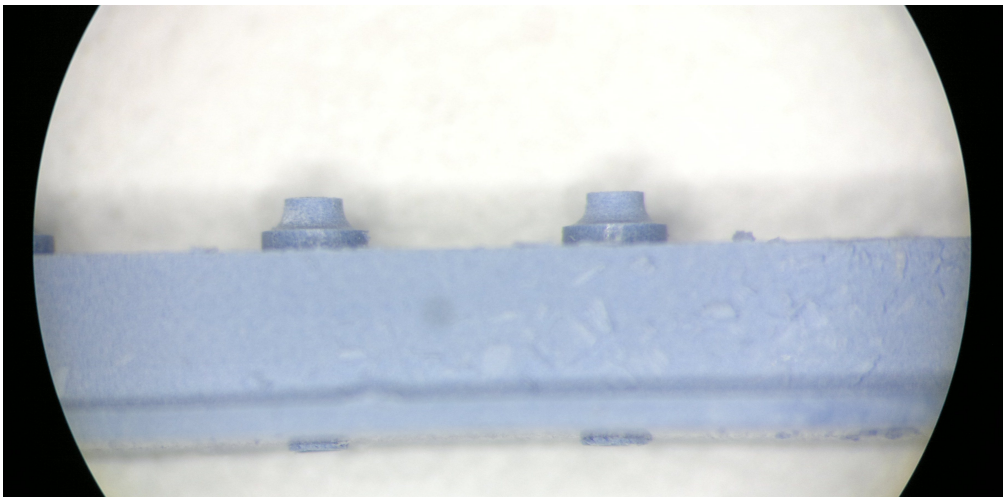

Figure B.5: Capillary tubes for Design D7

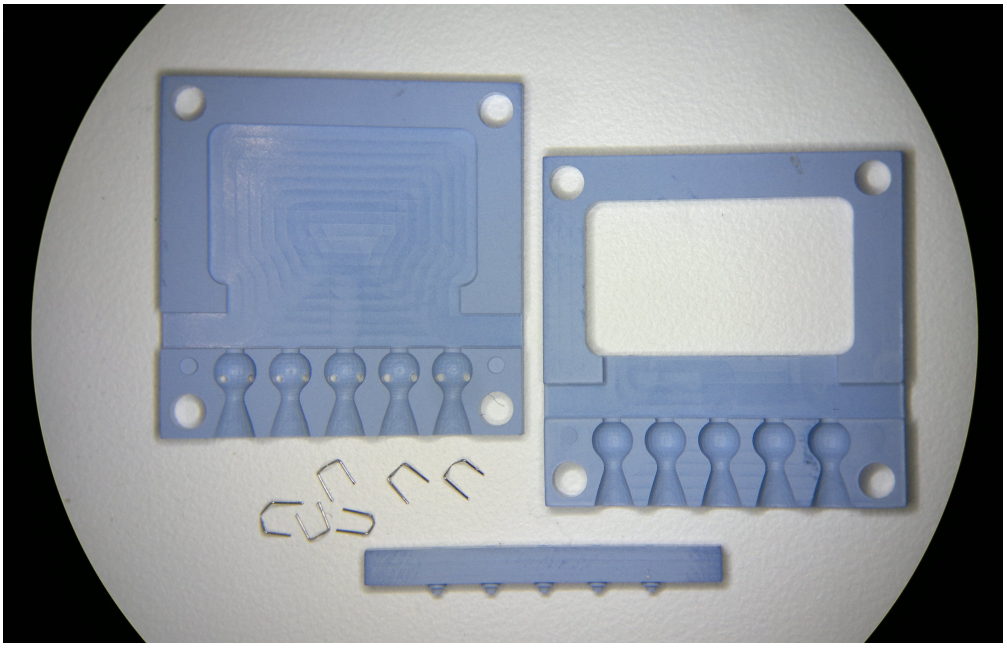

Figure B.6: All parts for Design D7

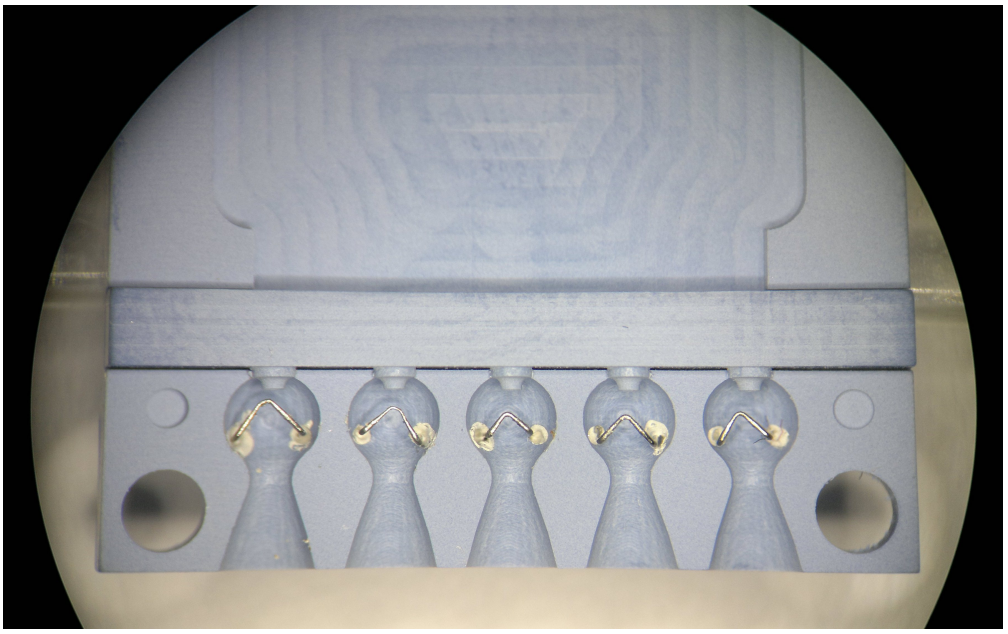

Figure B.7: Assembly of Design D7

B.4 Design D9

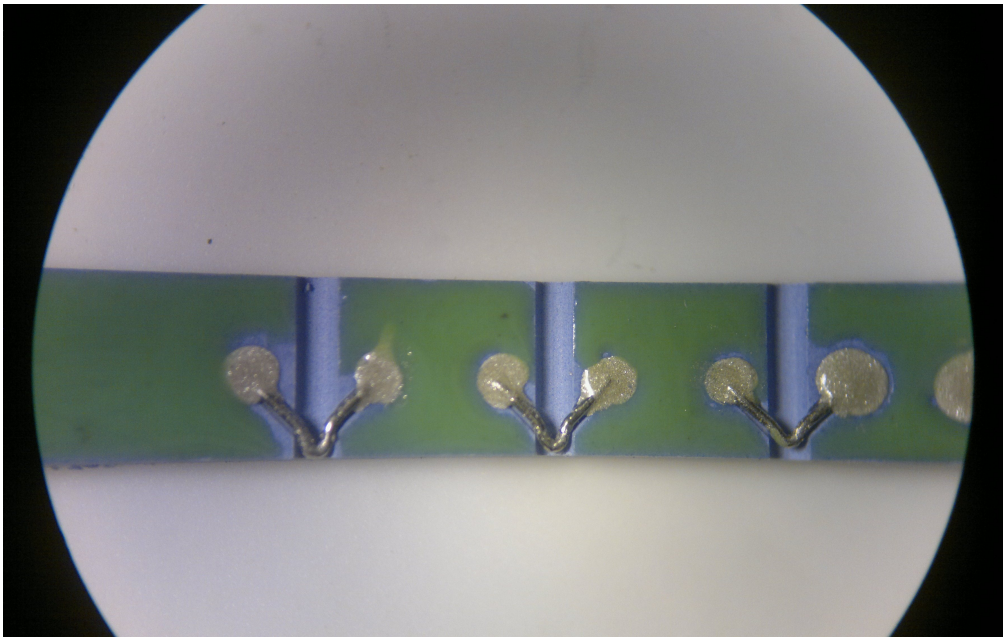

Figure B.8: Heating filaments integrated with the capillary tubes, before lamination.

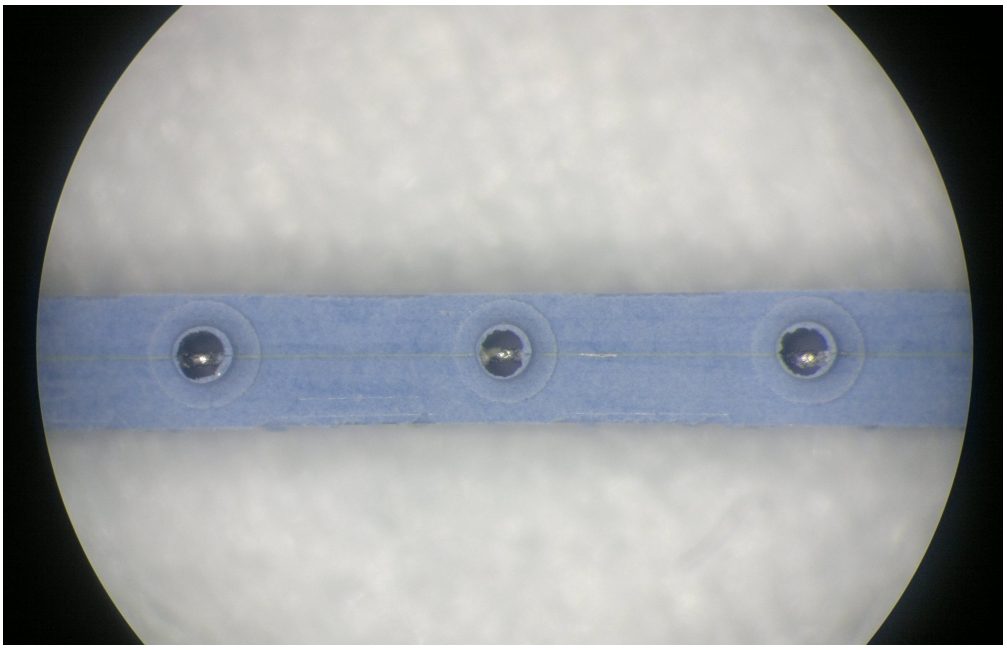

Figure B.9: Heating filaments integrated with the capillary tubes, after lamination and after edge milling.

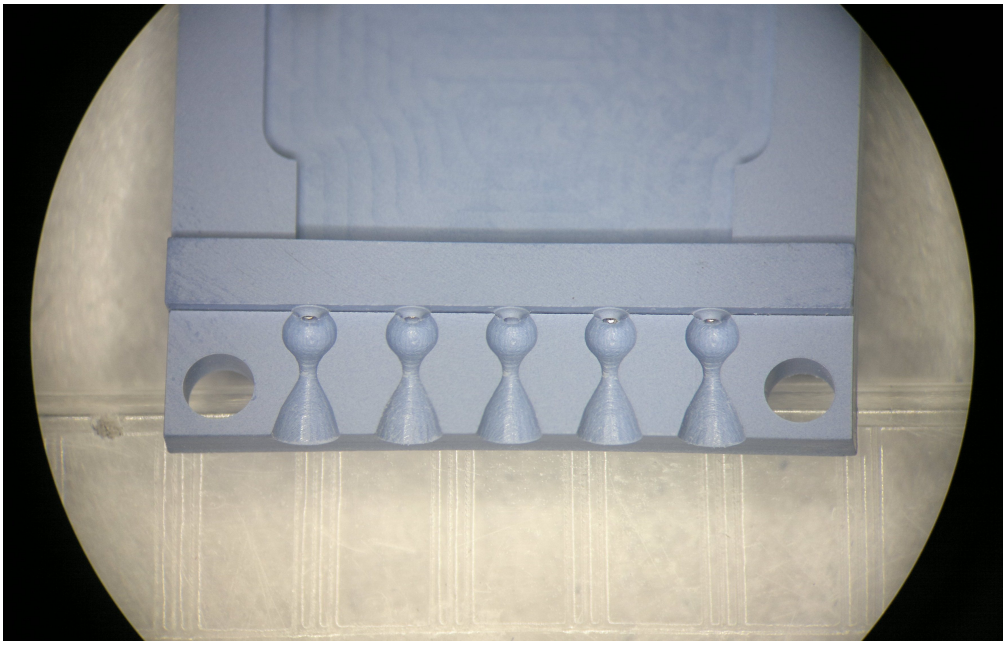

Figure B.10: Assembly of Design D9

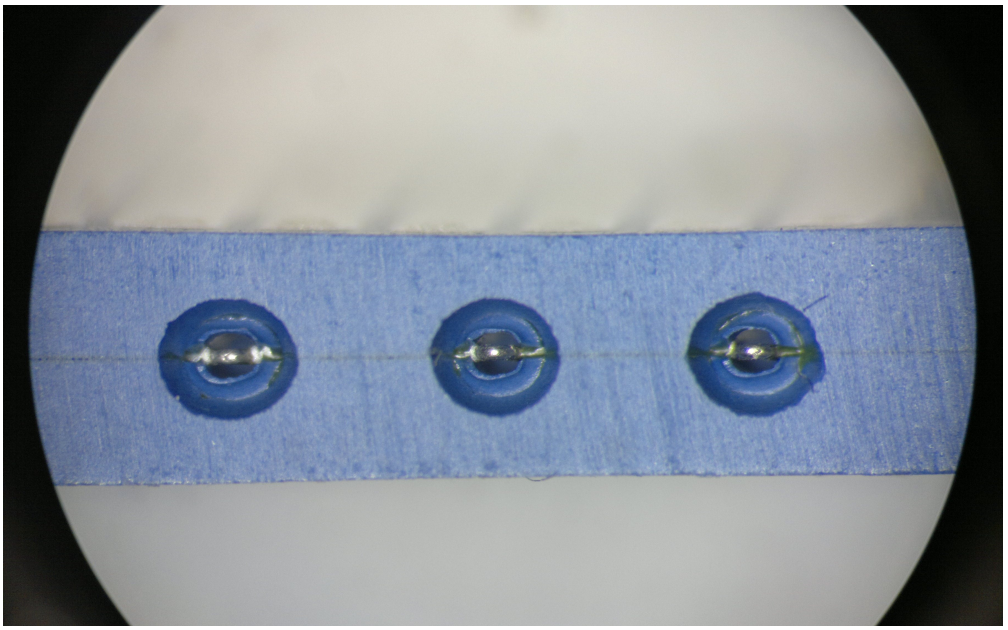

Figure B.11: Design D9 after sintering. DPA was performed on this prototype, revealing the broken edges of the capillary tubes due to lack of tolerance for the heating filaments.

B.5 Design D13

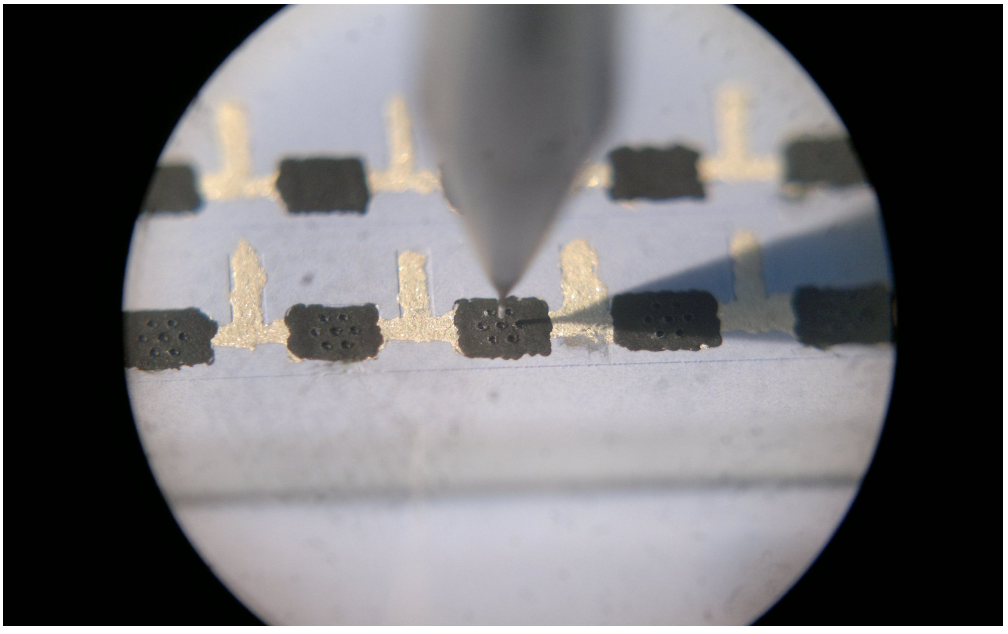

Figure B.12: Drilling capillaries Design D13

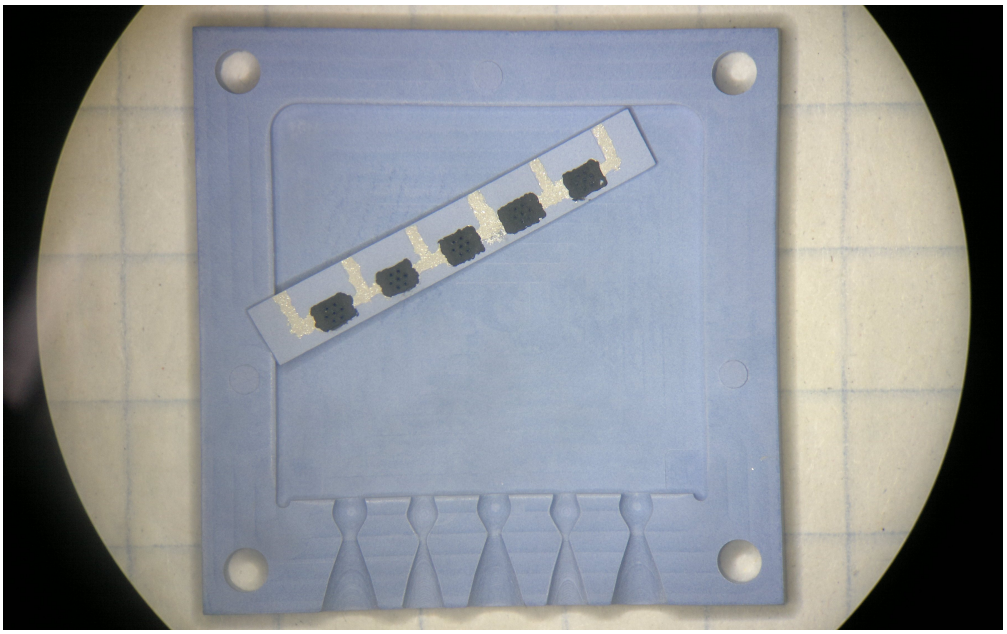

Figure B.13: Design D9 With Thickfilm Heaters

B.6 Design D14

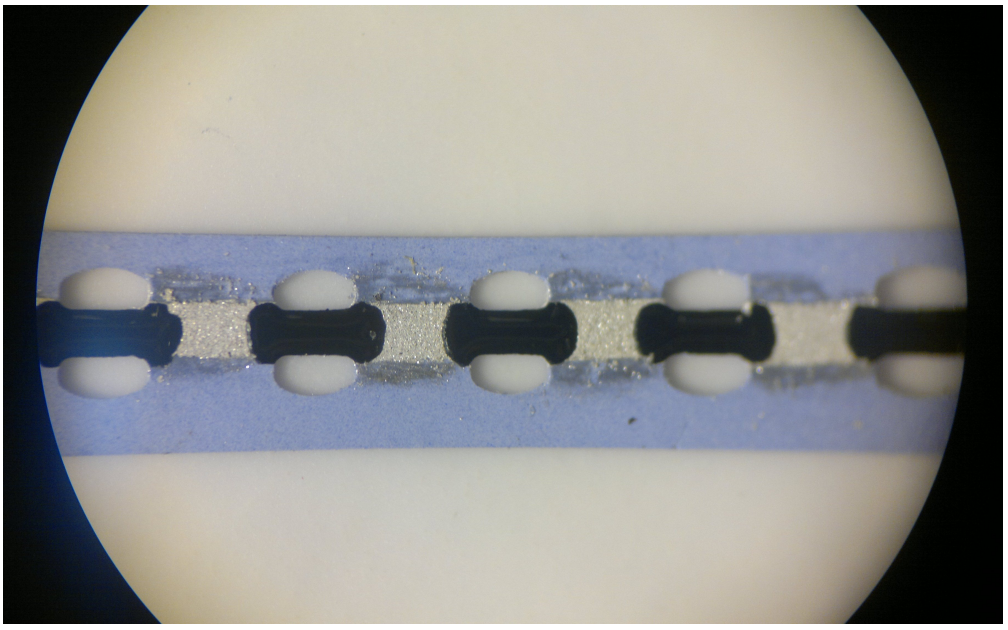

Figure B.14: Design D14 thickfilm heaters printed on a single sheet of LTCC

B.7 Design D15A and B

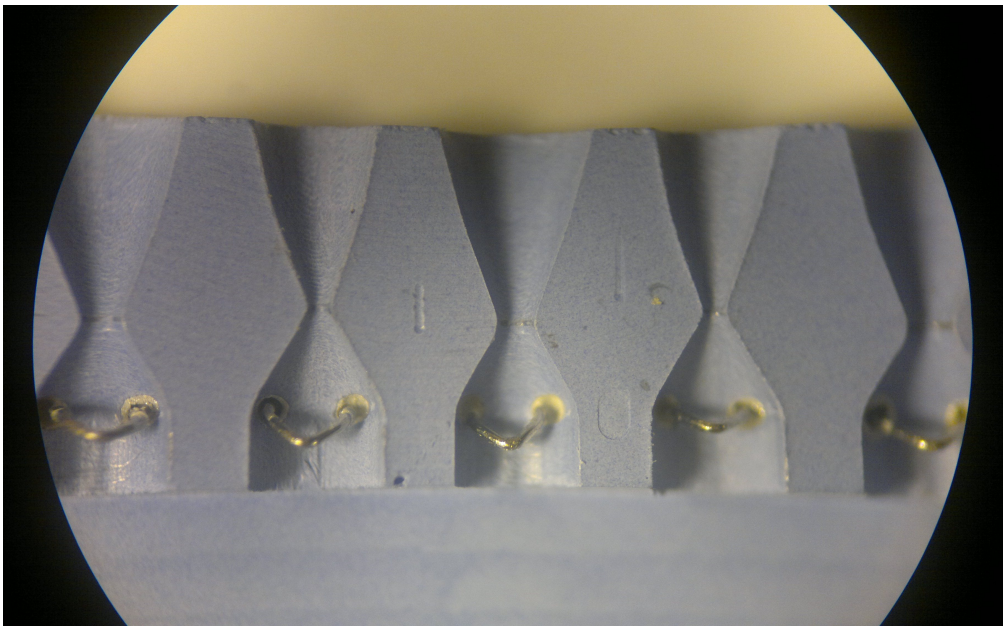

Figure B.15: Design D15A, one of the working prototypes

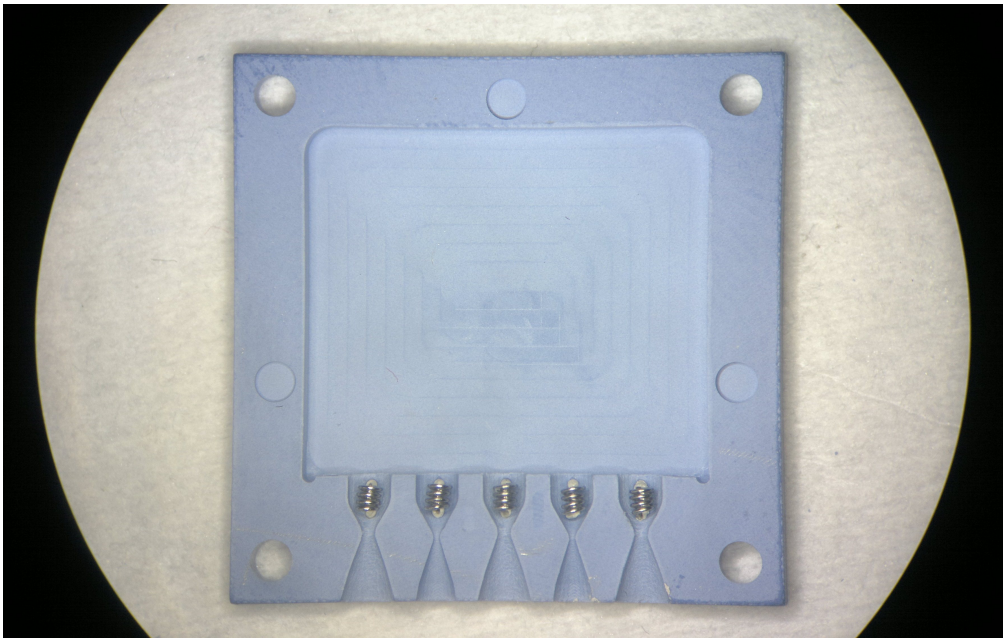

Figure B.16: Design 15B, the thruster performing the best so far

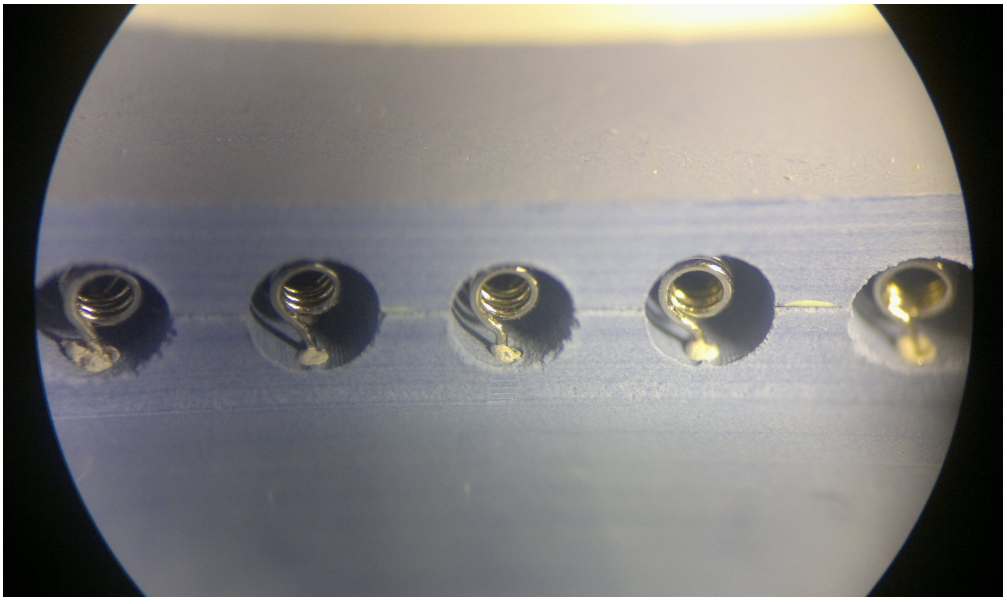

Figure B.17: Design D15B Chambers

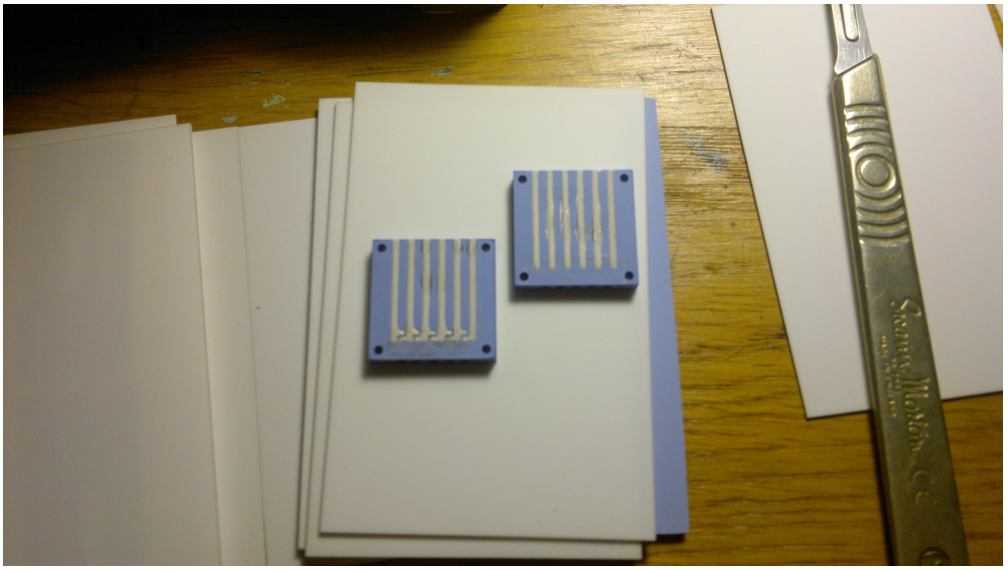

Figure B.18: Design D14 and D15A Backside, after printing conducters

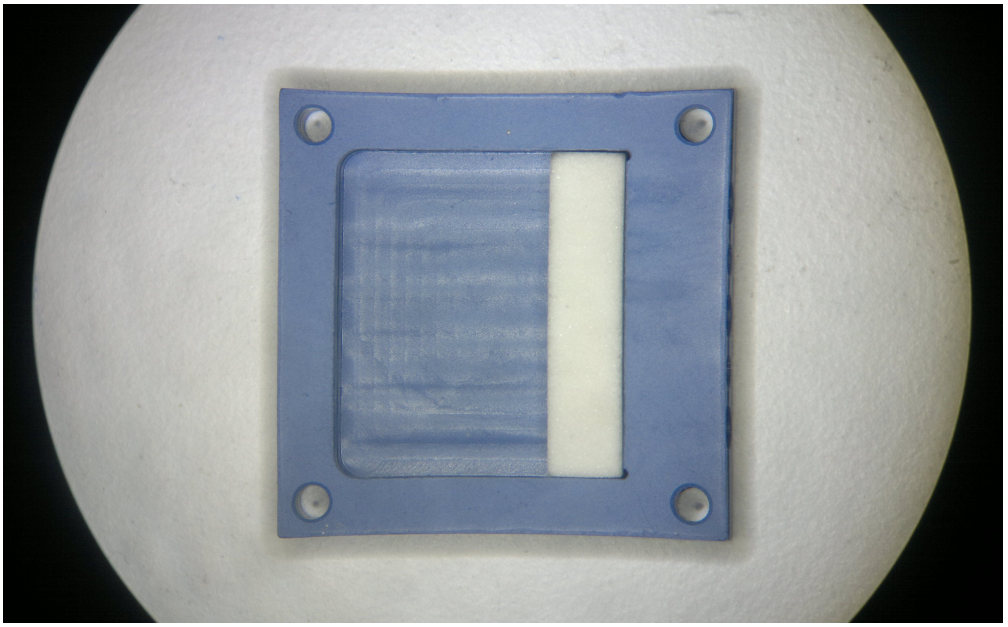

Figure B.19: Design D15A completed with borosilicate glass frit applied utilizing epoxy glue

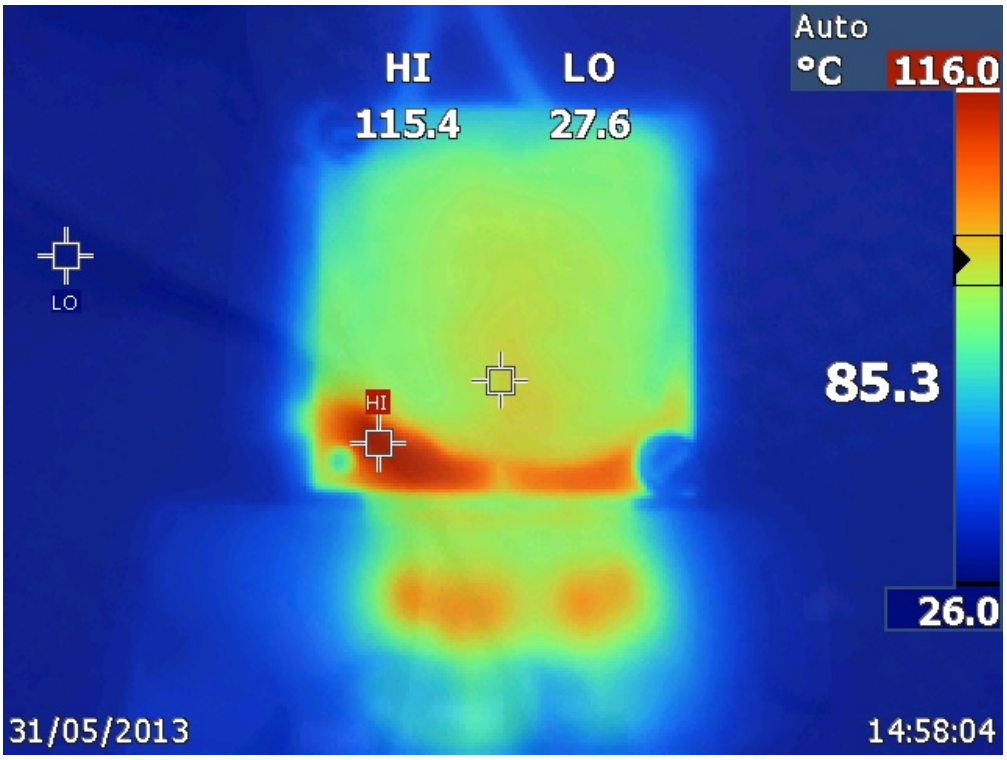

Figure B.20: Thrust jet heating a plate lying slanted in front of the nozzles. The thruster is 17 mm x 17 mm

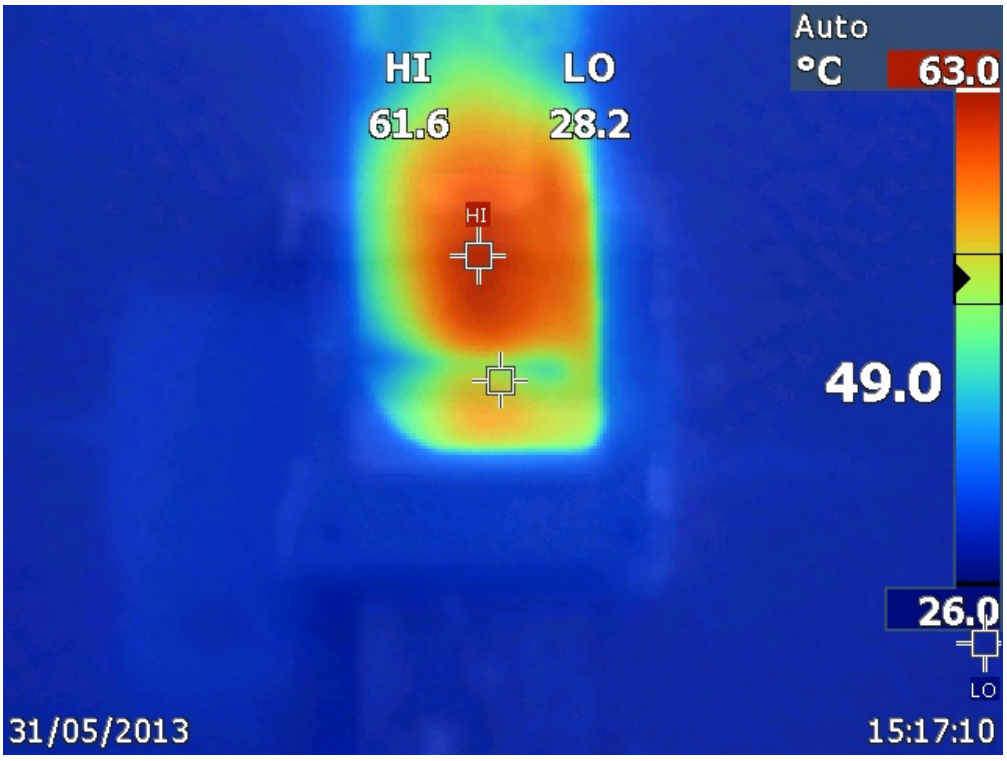

Figure B.21: Thrust jet heating a slanted plate in front of the nozzles. The thruster is in top just outside the picture, the jet originates from the top of the picture

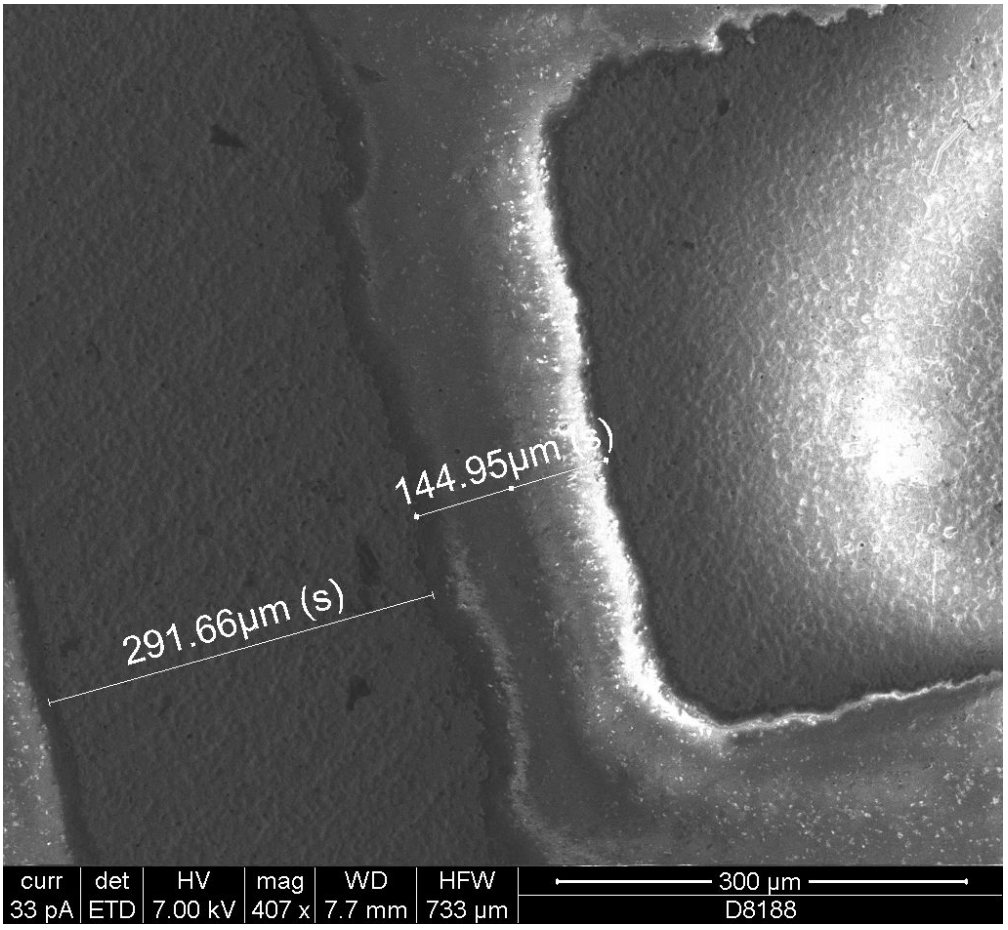

Figure B.22: SEM image of conductors on LTCC. The line width definition is observed.

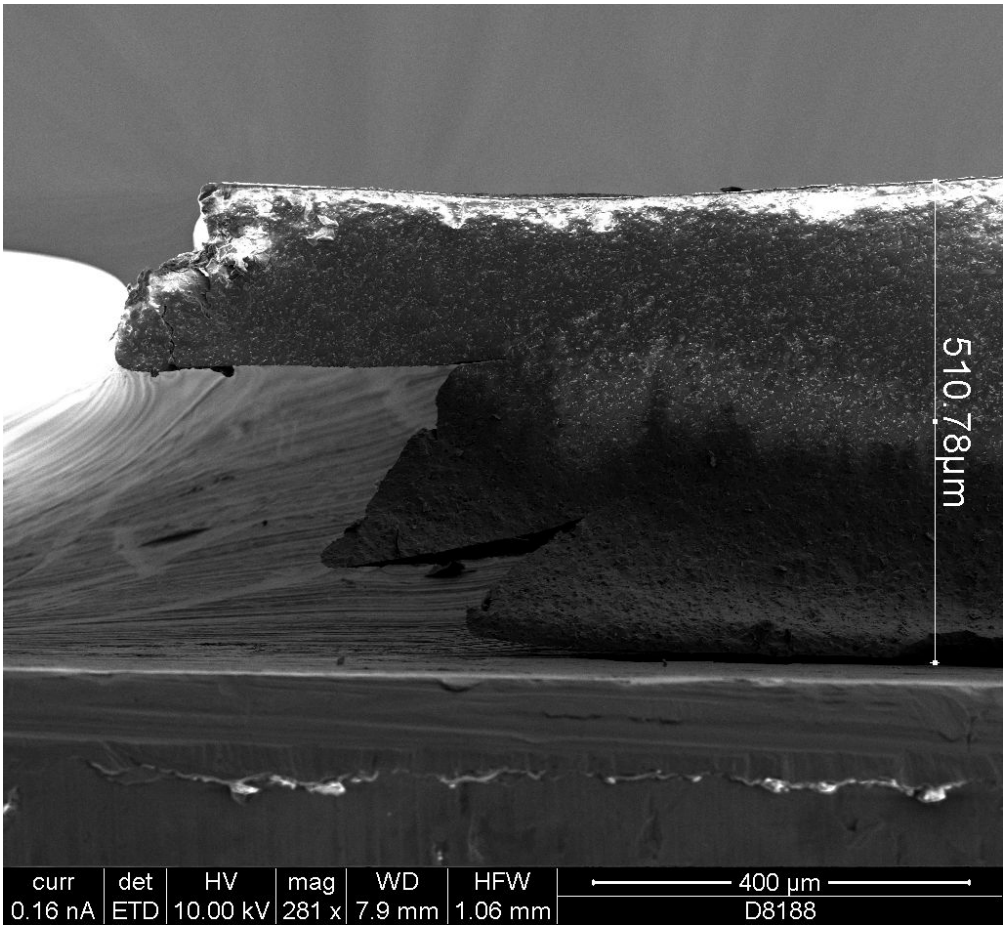

Figure B.23: SEM image of the lamination of 3 LTCC sheets after sintering.

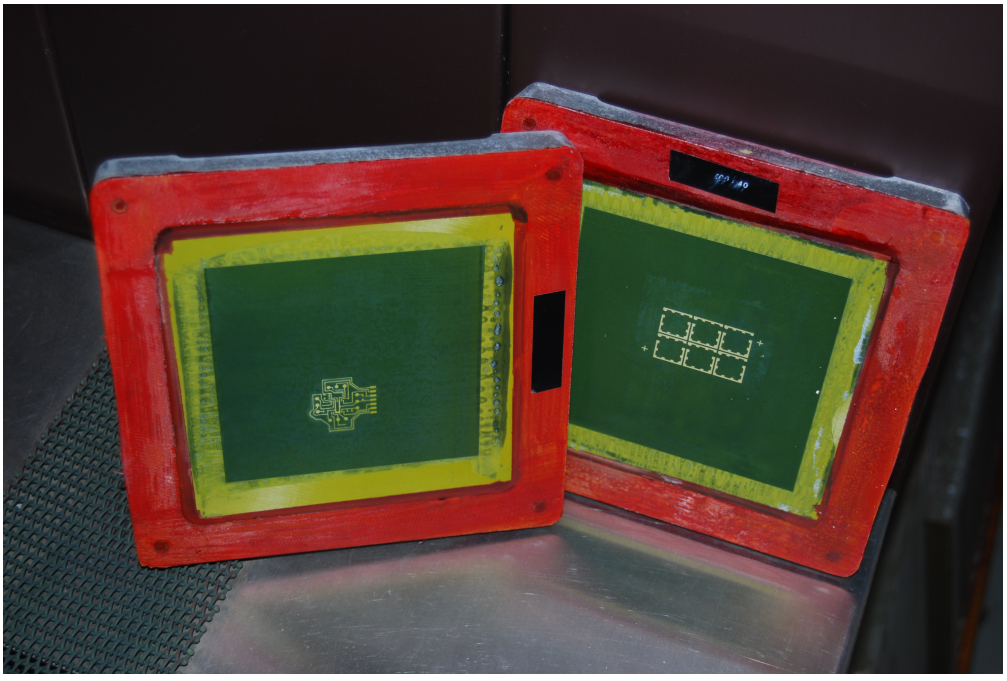

Figure B.24: Fully developed stencils on a nylon mesh carried on an aluminum frame. The stencils are developed showering them in lukewarm water.

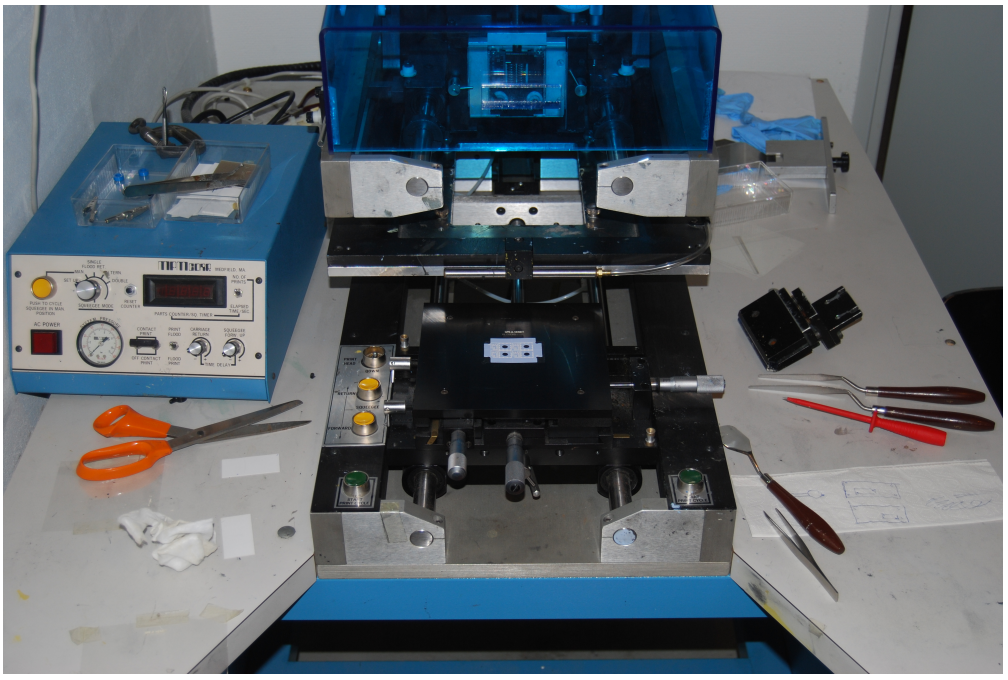

Figure B.25: Screen printing machine. The blue box to the left is for controlling the pressure on the squeegee. In the middle the chuck with a printed sheet is seen. The micrometer screws are used to align the substrate to the stencil.

Appendix C

SEM Images Porous Materials

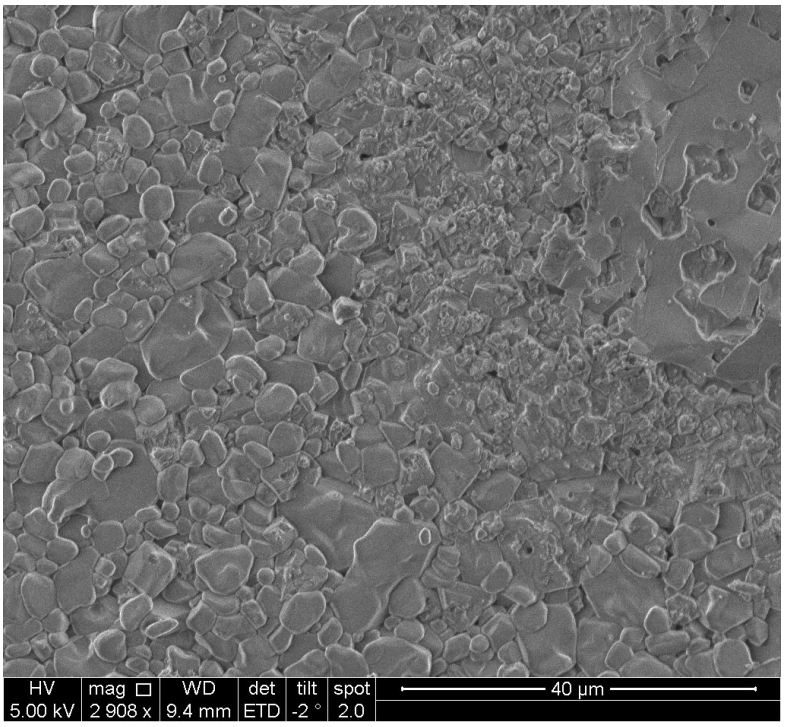

Figure C.1: Pure sintered capacitive paste. The porosity is limited to the surface.

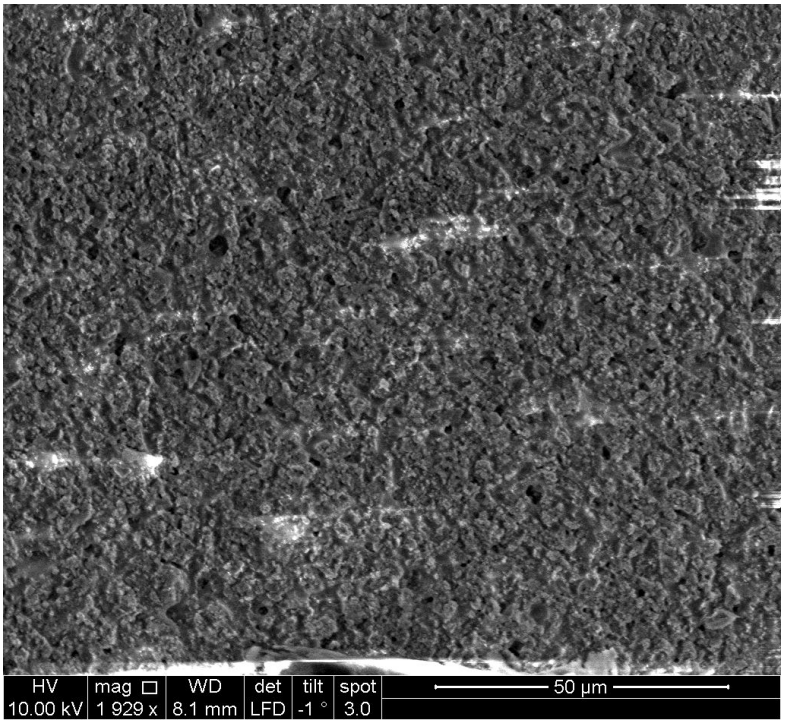

Figure C.2: Sintered capasitive paste mixed with clay. Some porosity is achieved, but the pores are in the submicron regime.

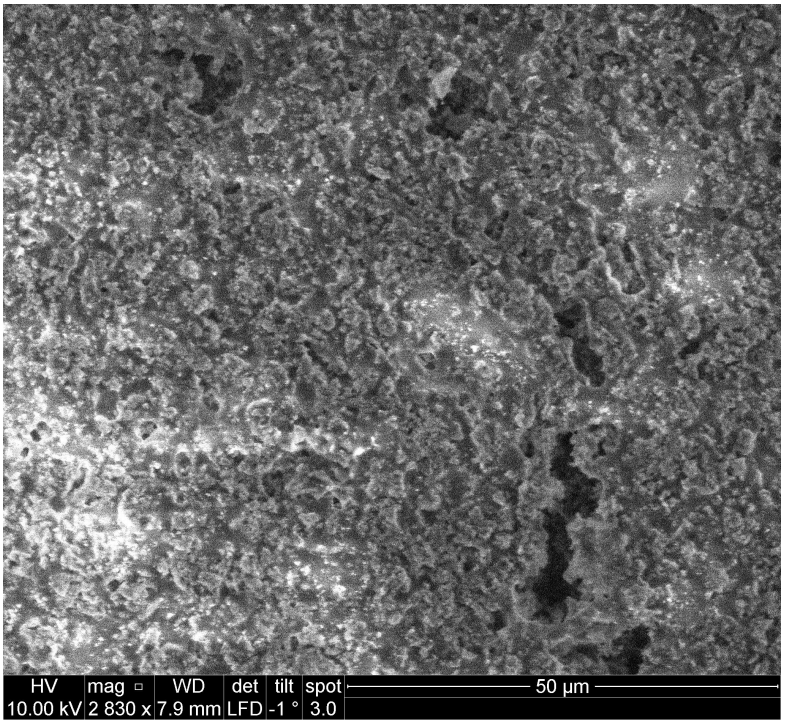

Figure C.3: Sintered capasitive paste mixed with carbon powder. Inhomogeneous porosity is achieved. The pore sizes ranges over several orders of magnitude.

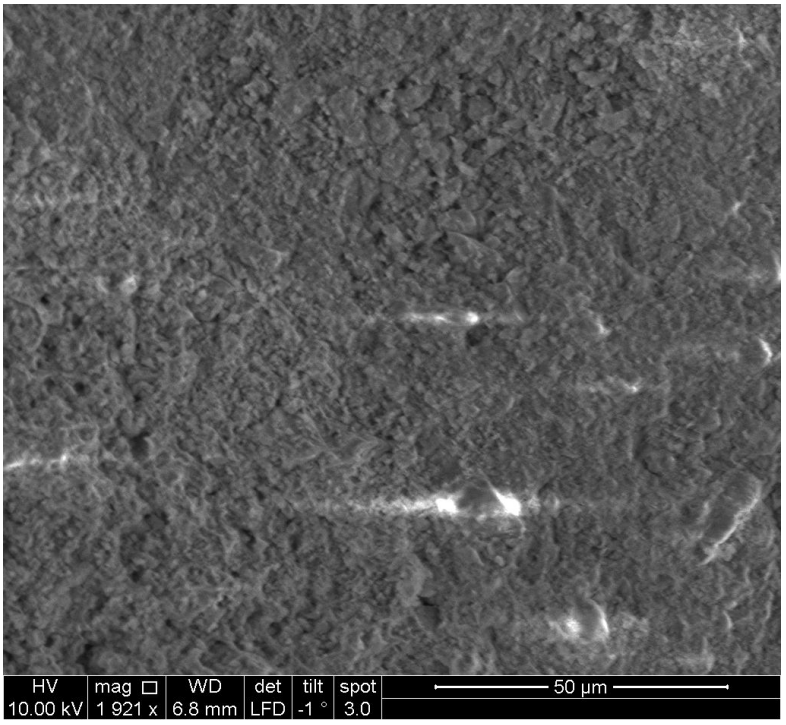

Figure C.4: Sintered clay is porous, but the pores are in the submicron regime.

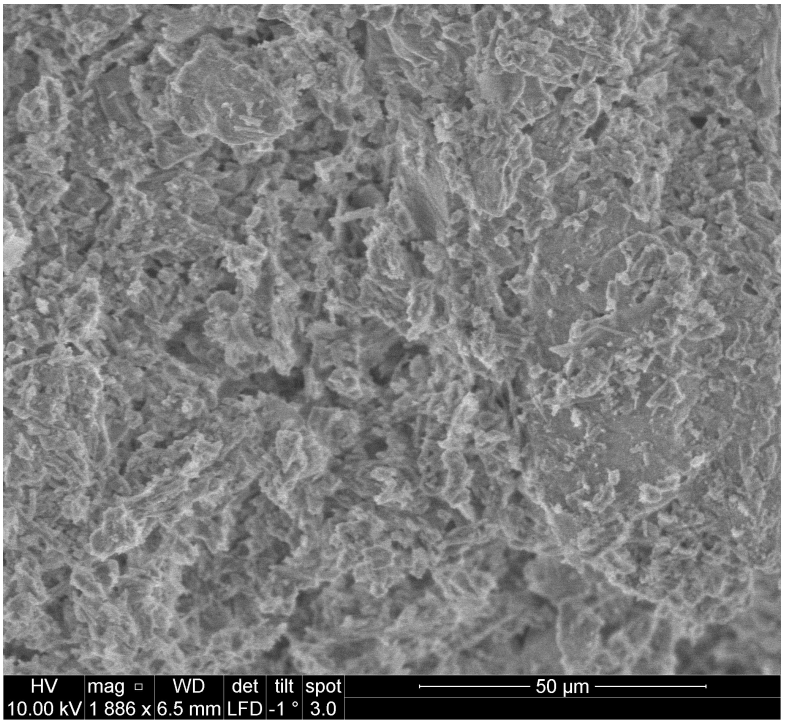

Figure C.5: Sintered gypsum is porous and the pores are in the order of 10µm, but the material is very brittle.

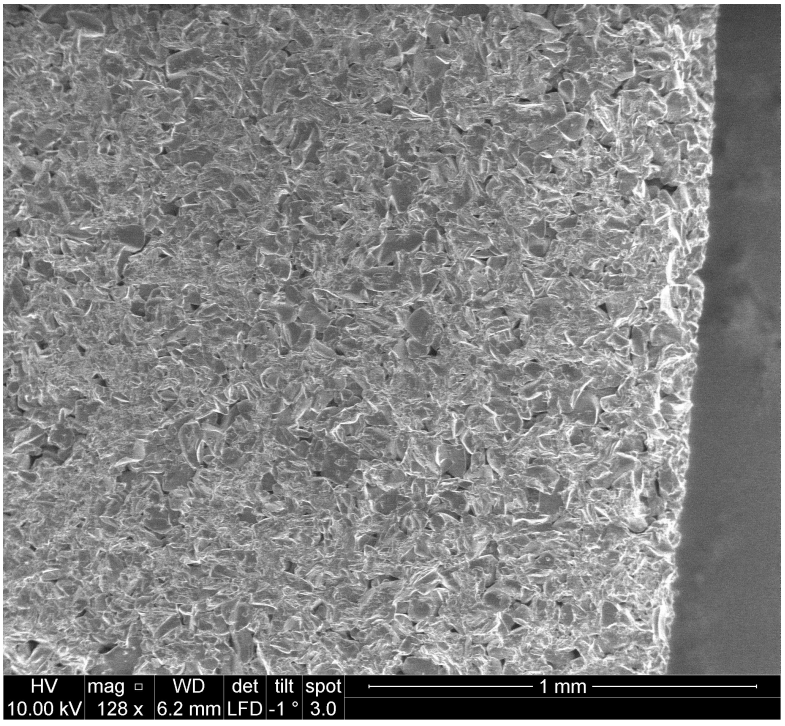

Figure C.6: P4 - porosity of 10-16 µm, Borosilicate Glass Frit 128x

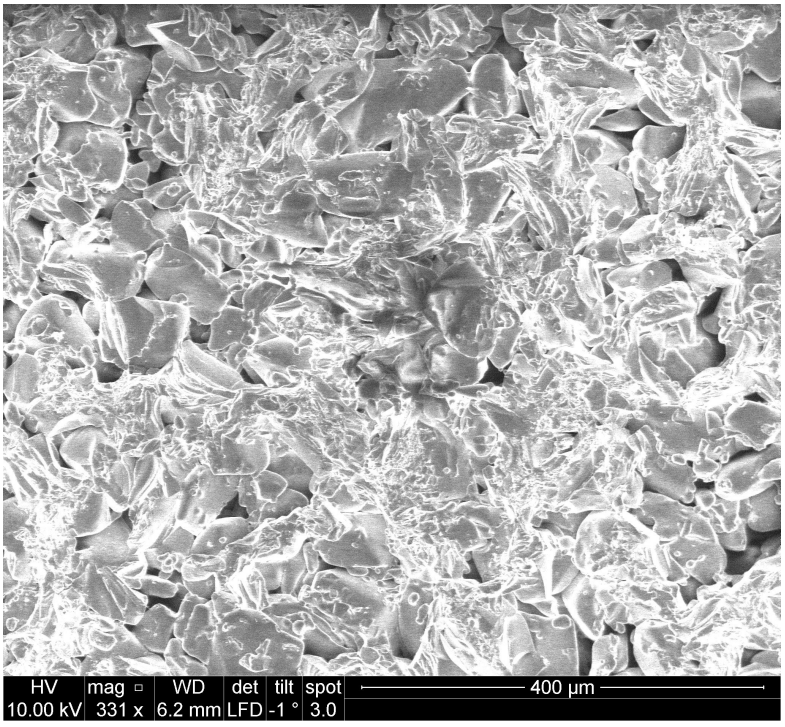

Figure C.7: P4 - porosity of 10-16 µm, Borosilicate Glass Frit 331x

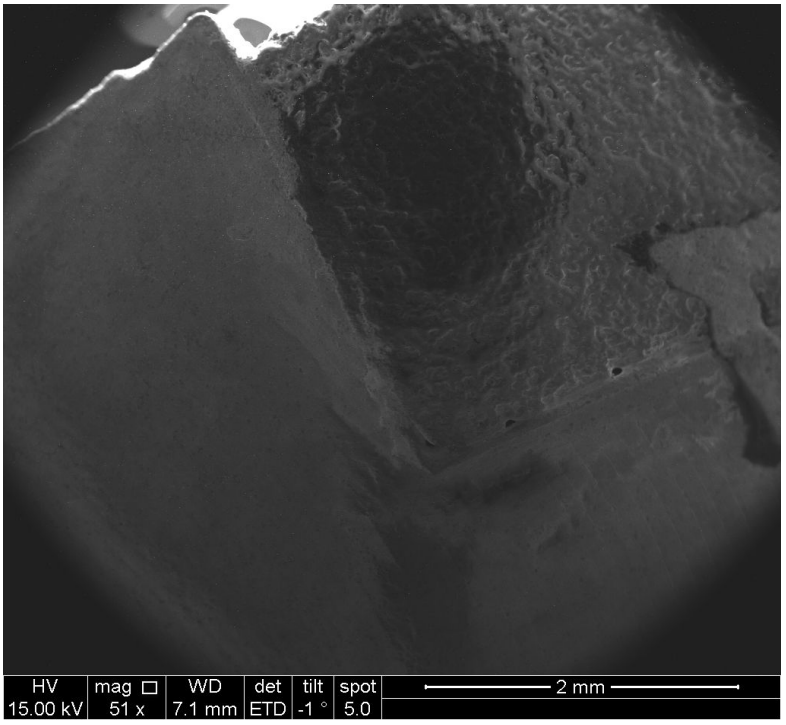

Figure C.8: Borosilicate glass frit co-fired with LTCC laminates well using cover glas, but is loosing its porosity

Appendix D

Dimensional Drawings

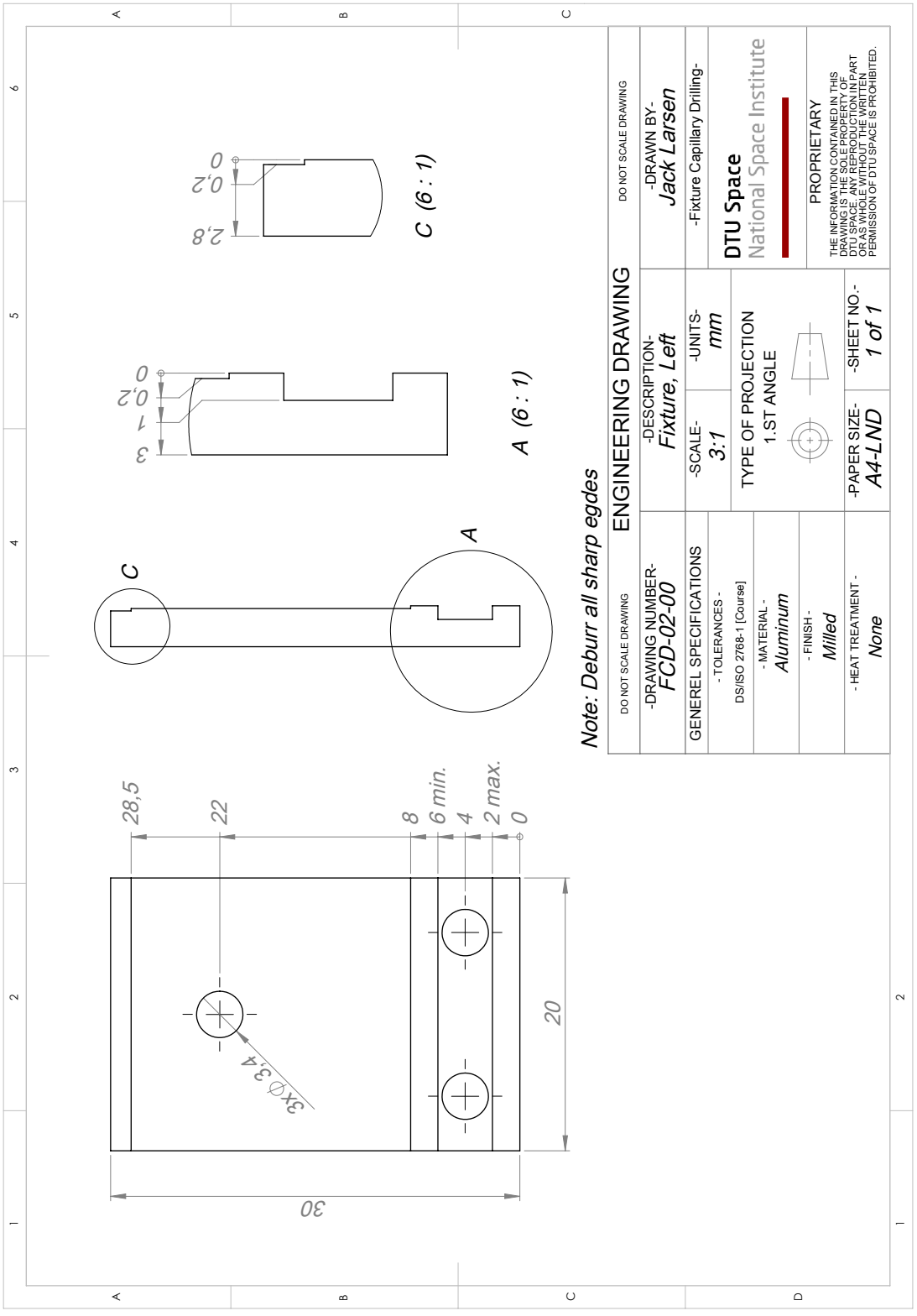

Figure D.1: Milling Tools: Fixture for capillary drilling, left

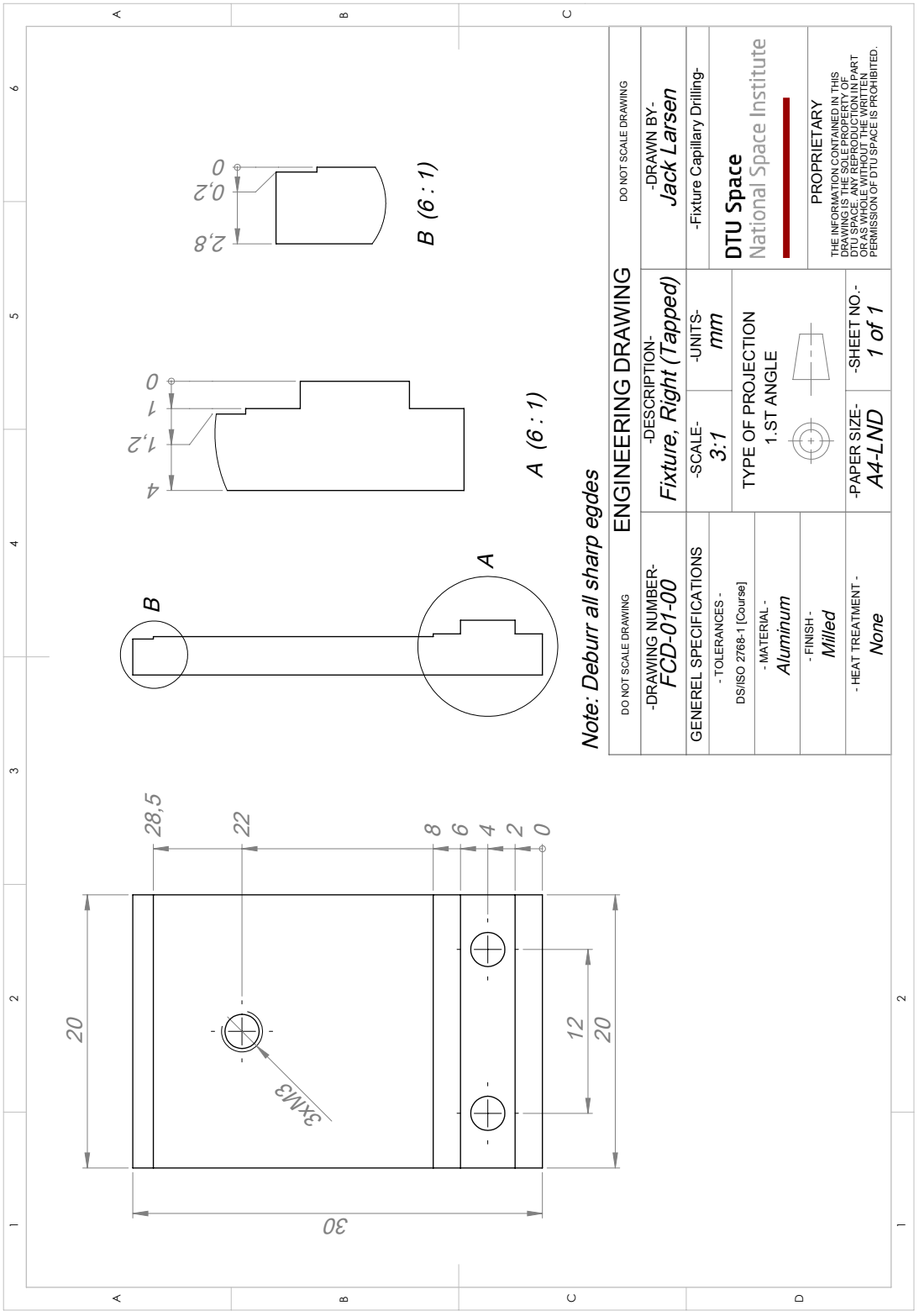

Figure D.2: Milling Tools: Fixture for capillary drilling, right (tapped)

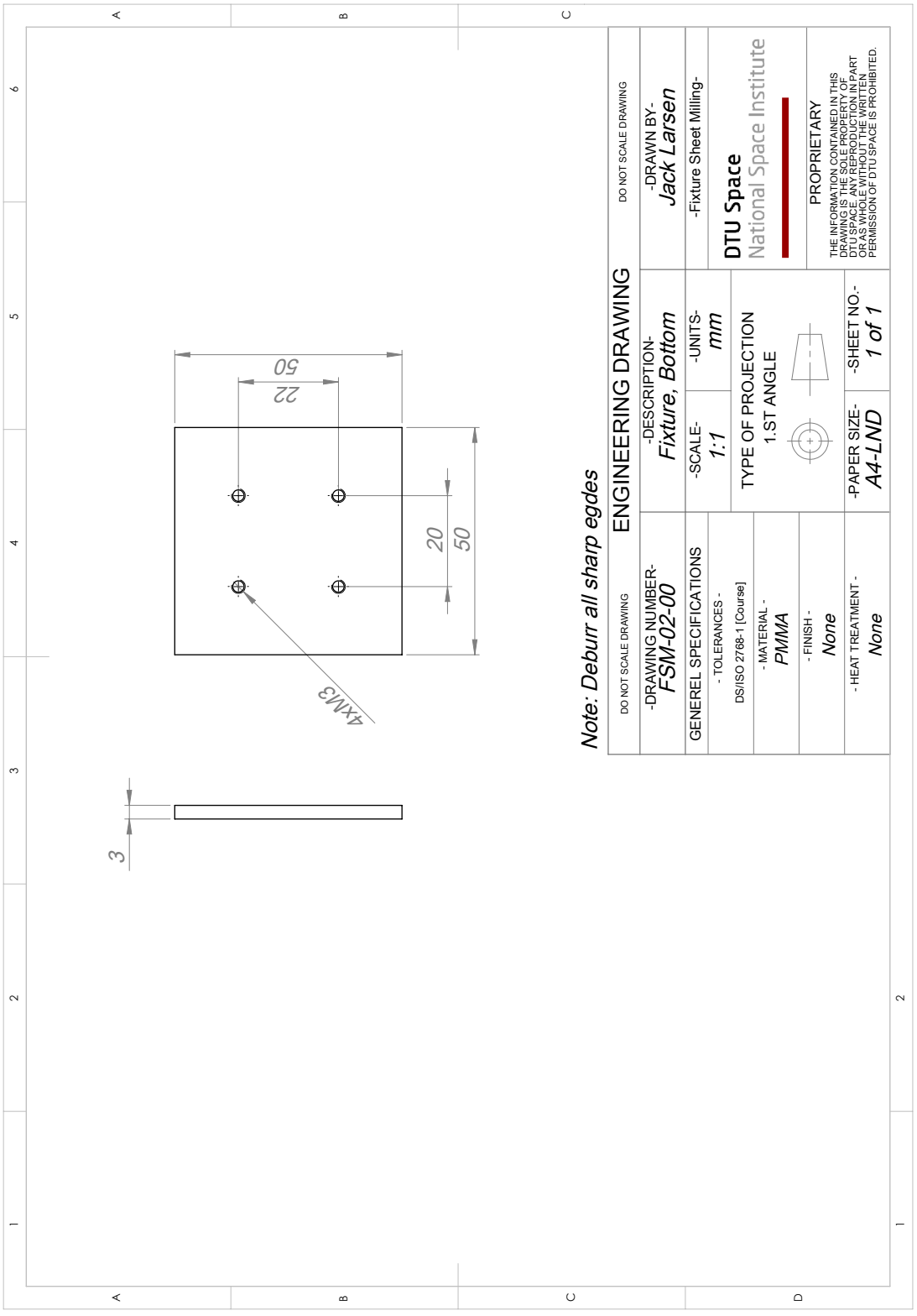

Figure D.3: Milling Tools: Fixture Sheet Milling, Bottom. Fixture used for milling the sheets for the heaters of design D13 and D14.

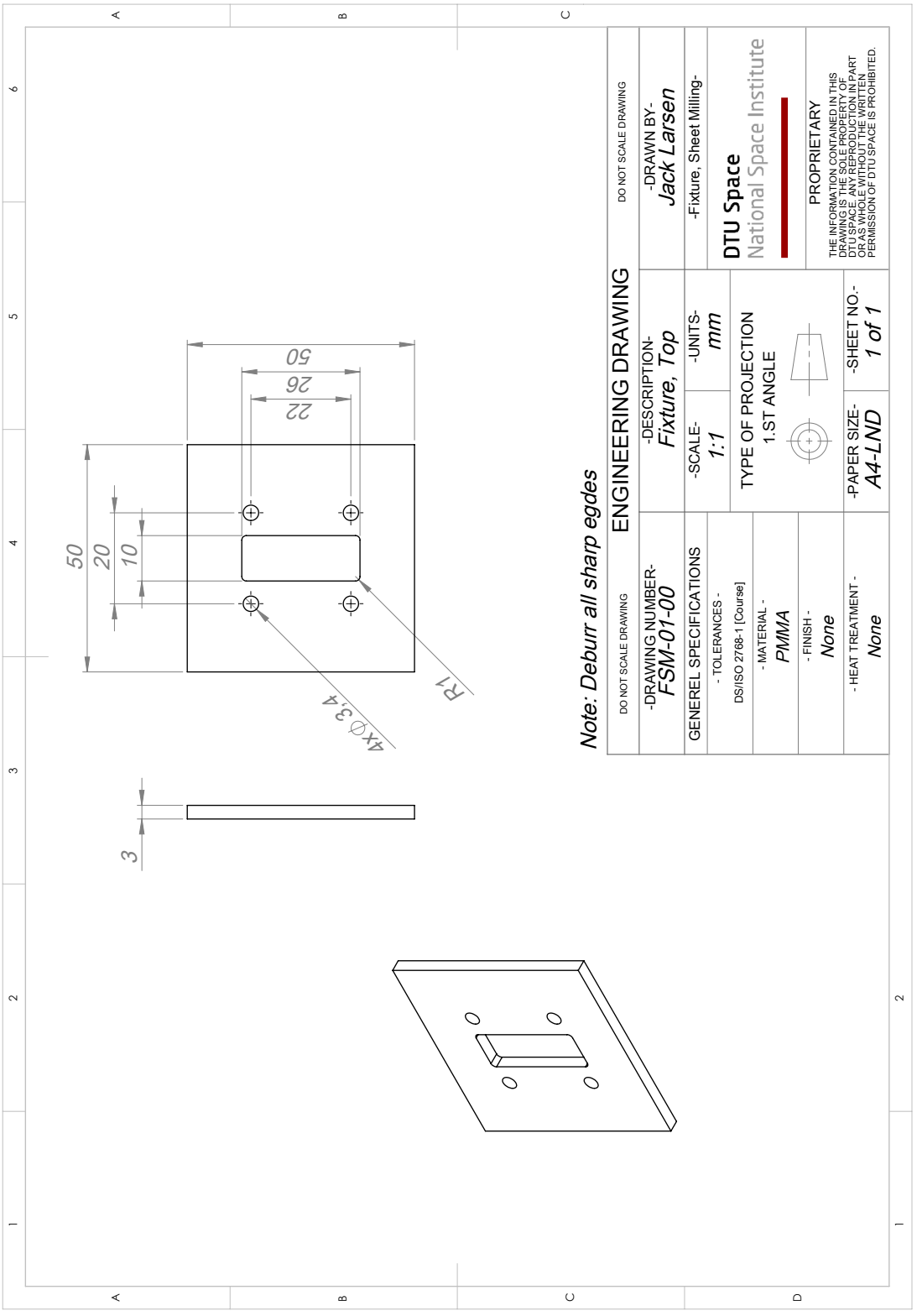

Figure D.4: Milling Tools: Fixture Sheet Milling, Top. Fixture used for milling the sheets for the heaters of design D13 and D14.

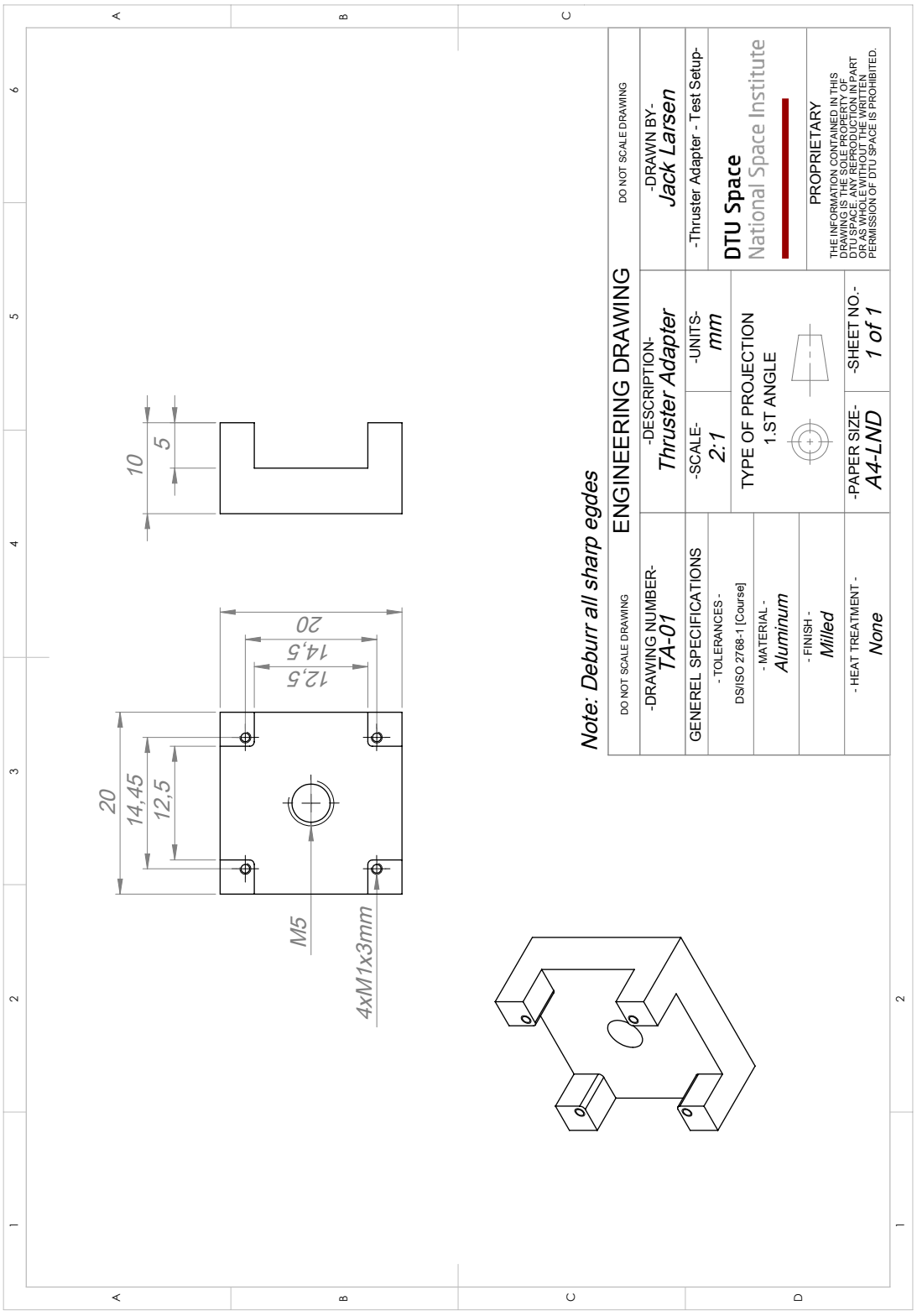

Figure D.5: Adapter used for mounting the thruster prototypes on the test bench.

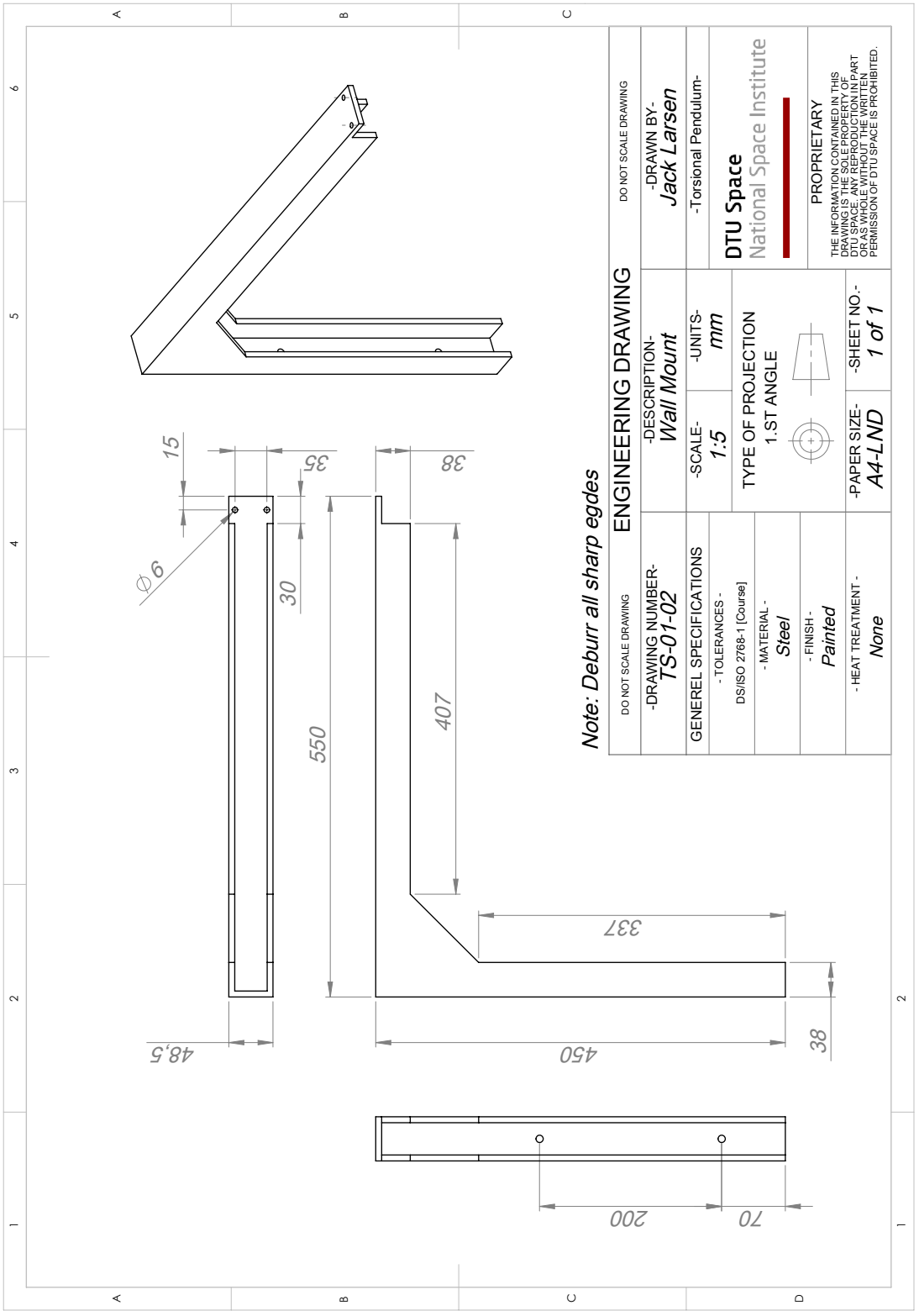

Figure D.6: Test Setup: Wall Mount

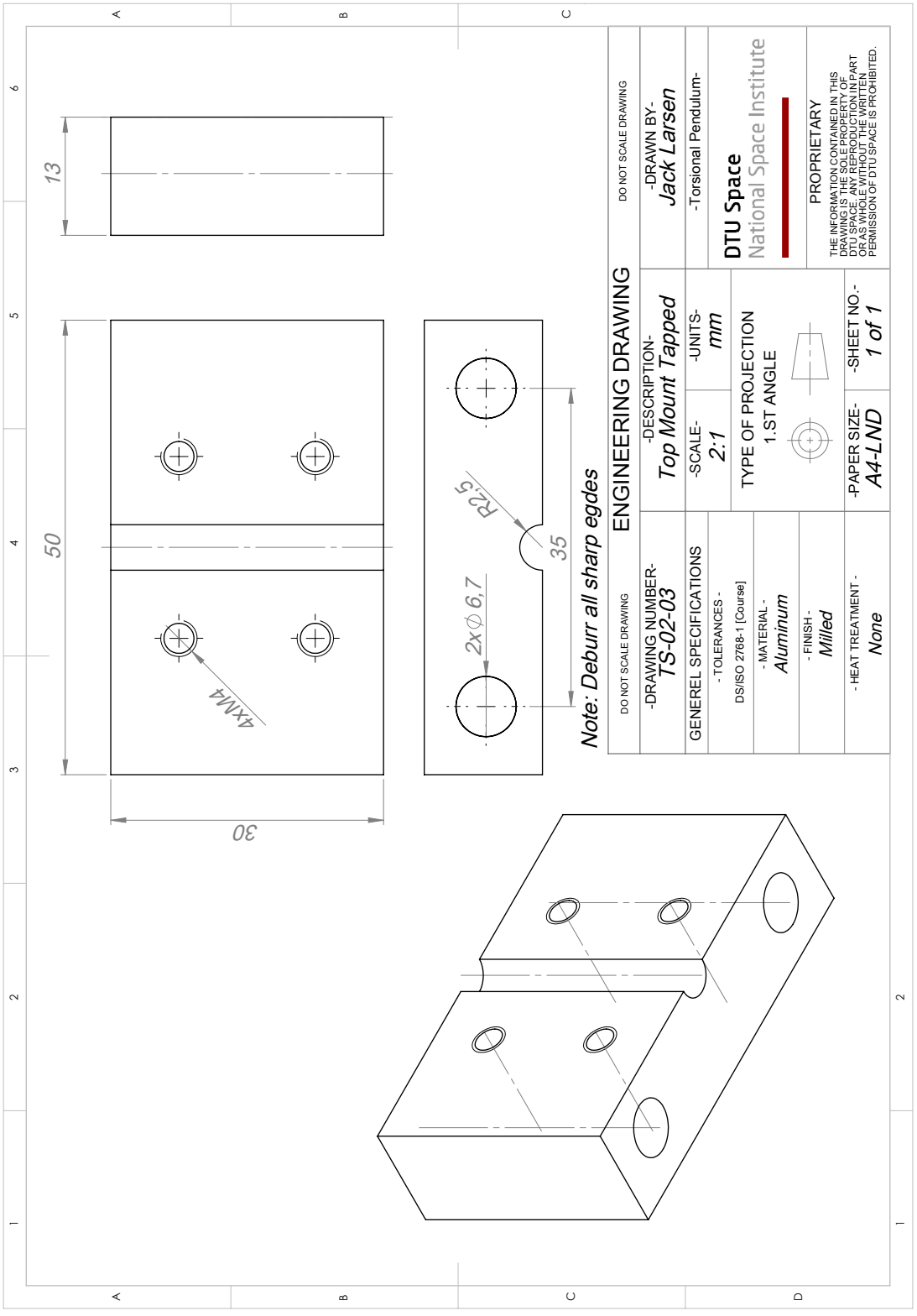

Figure D.7: Test Setup: Top mount fixing the glass wire.

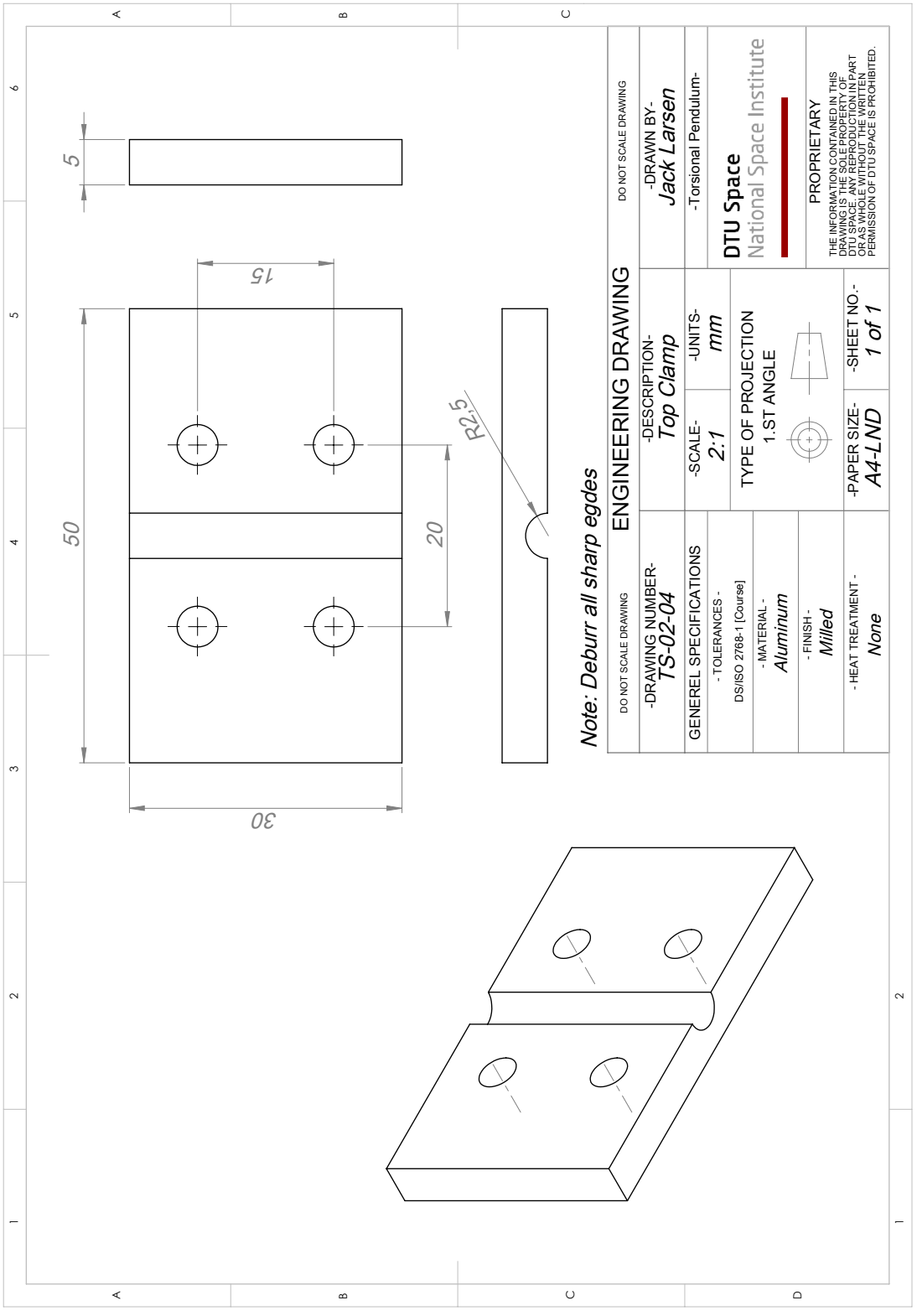

Figure D.8: Test Setup: Top clamp for fixing the glass wire.

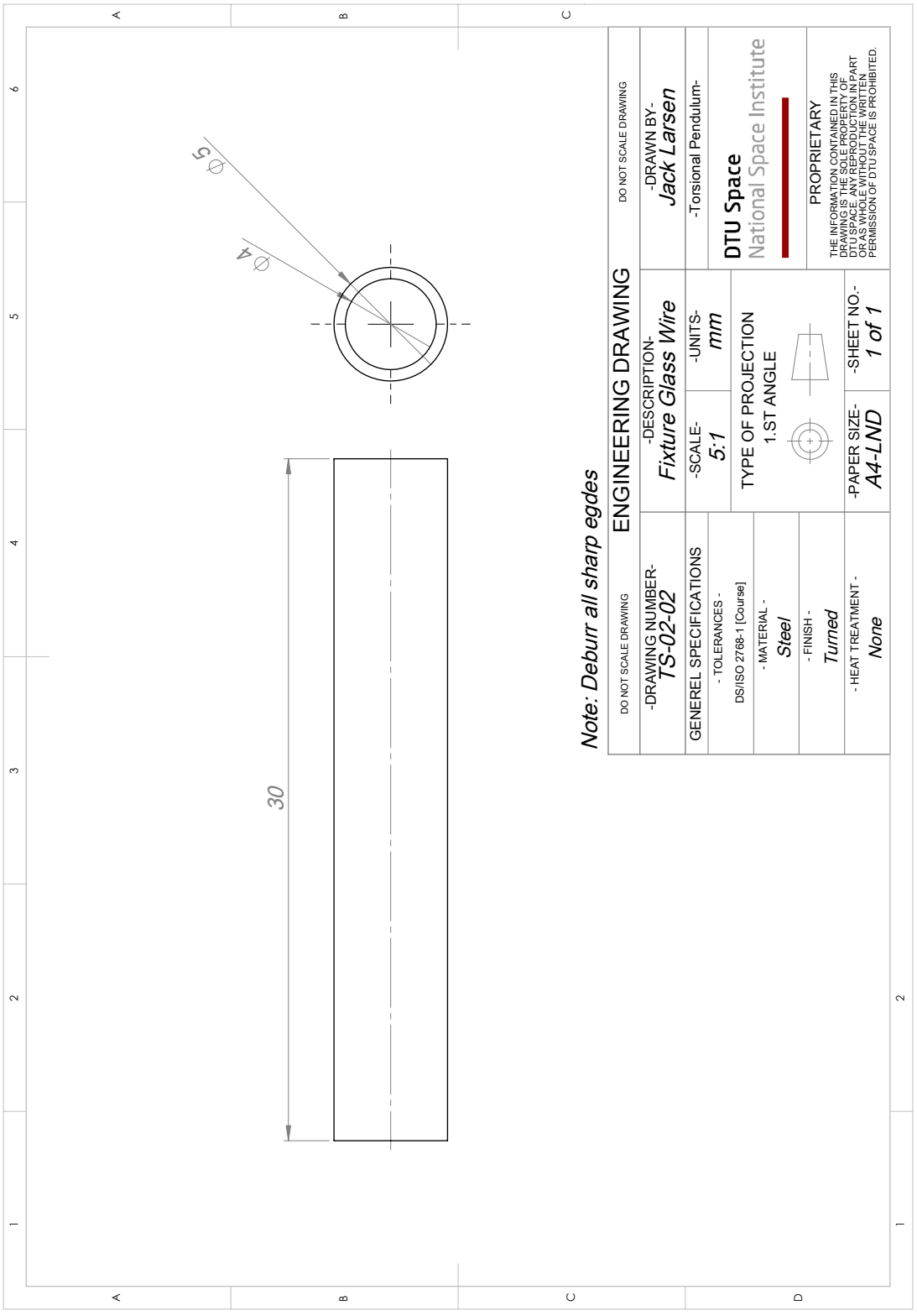

Figure D.9: Test Setup: Steel tube in which the glass wire is glued, to prevent clamping directly onto the glass wire.

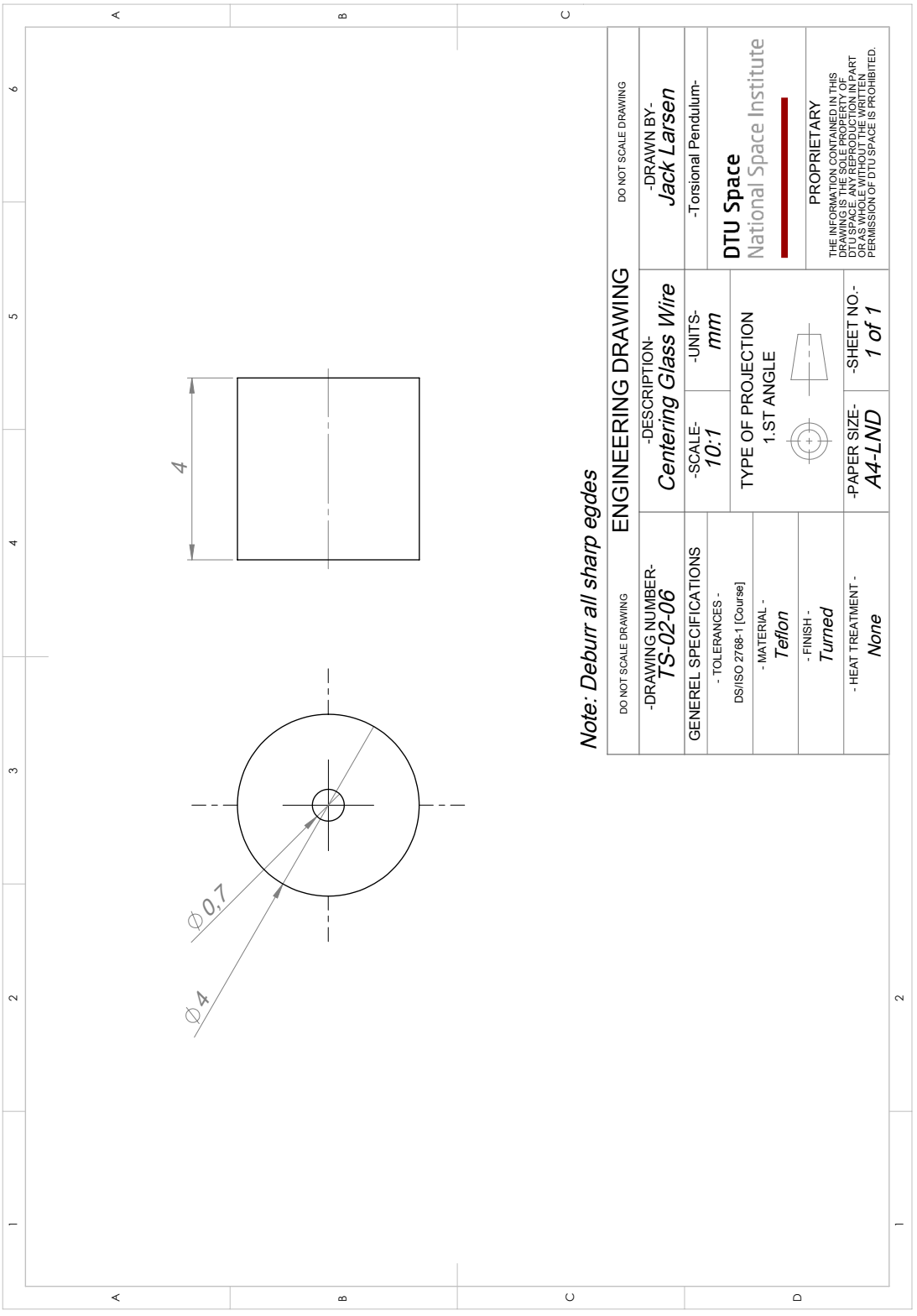

Figure D.10: Test Setup: Centering bushing for centering the glass wire while curring the epoxy glue fixing the wire to the steel tube.

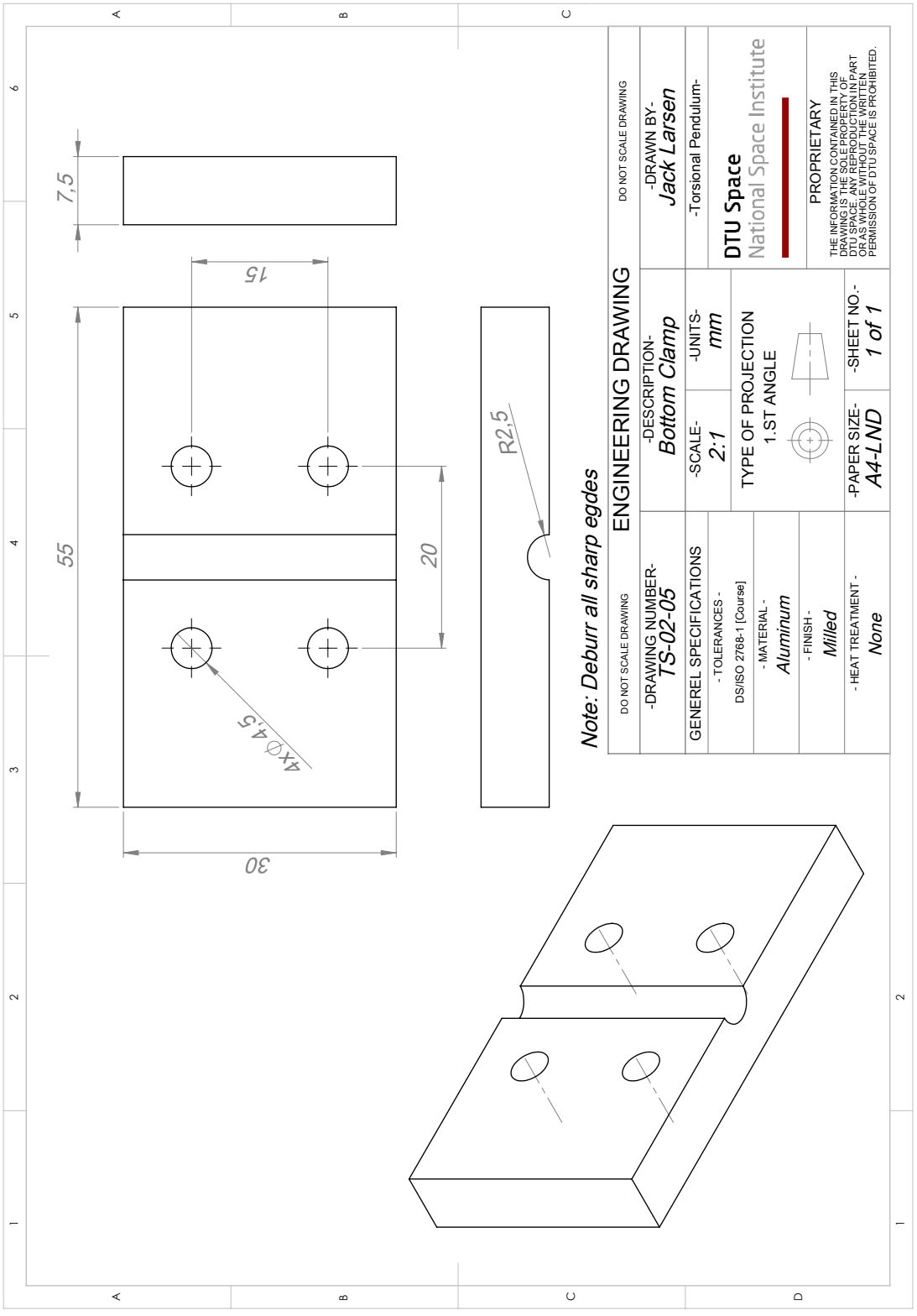

Figure D.11: Test Setup: Bottom clamp for fixing the glass wire.

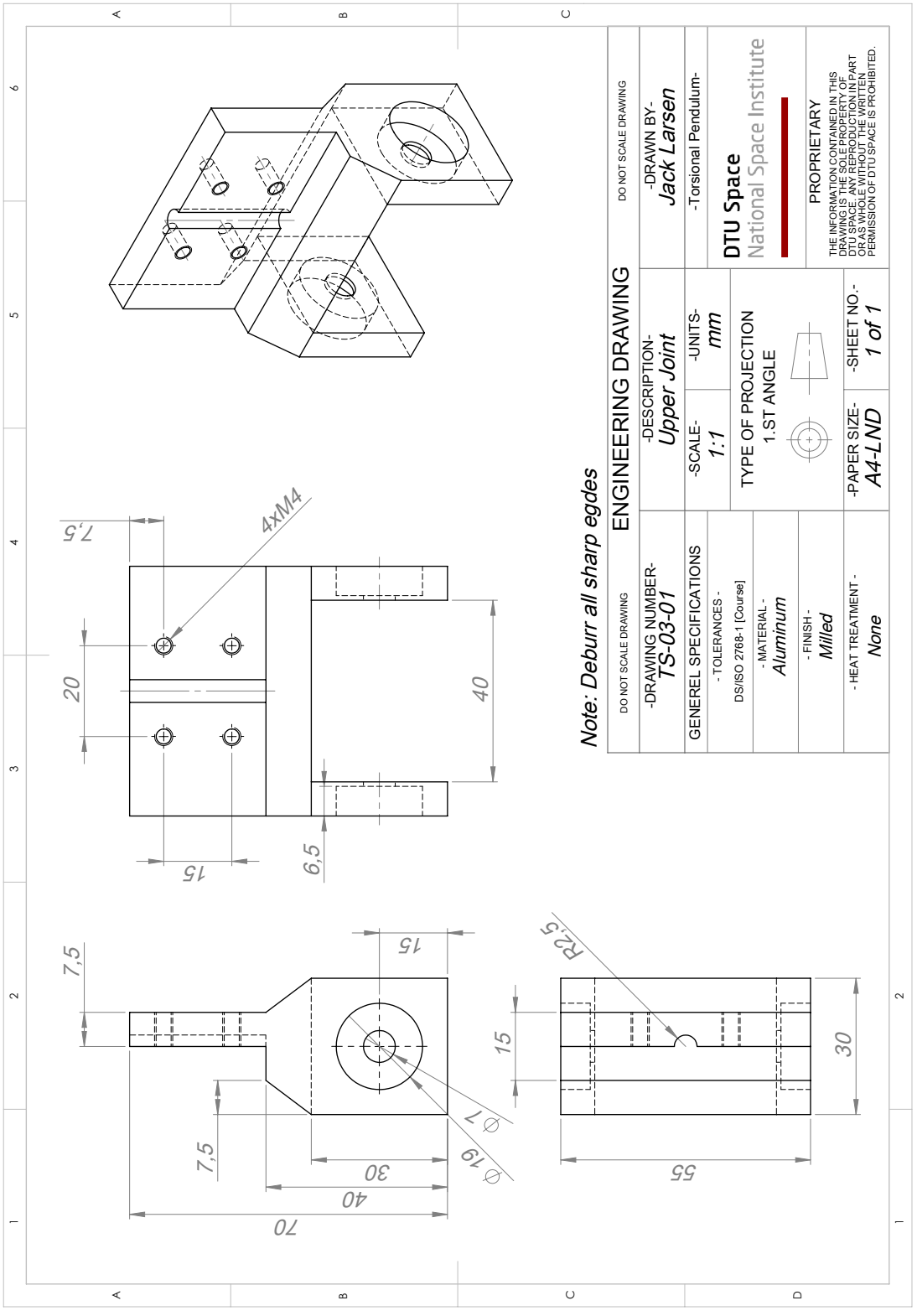

Figure D.12: Test Setup: Upper part of joint carrying the horizontal arm.

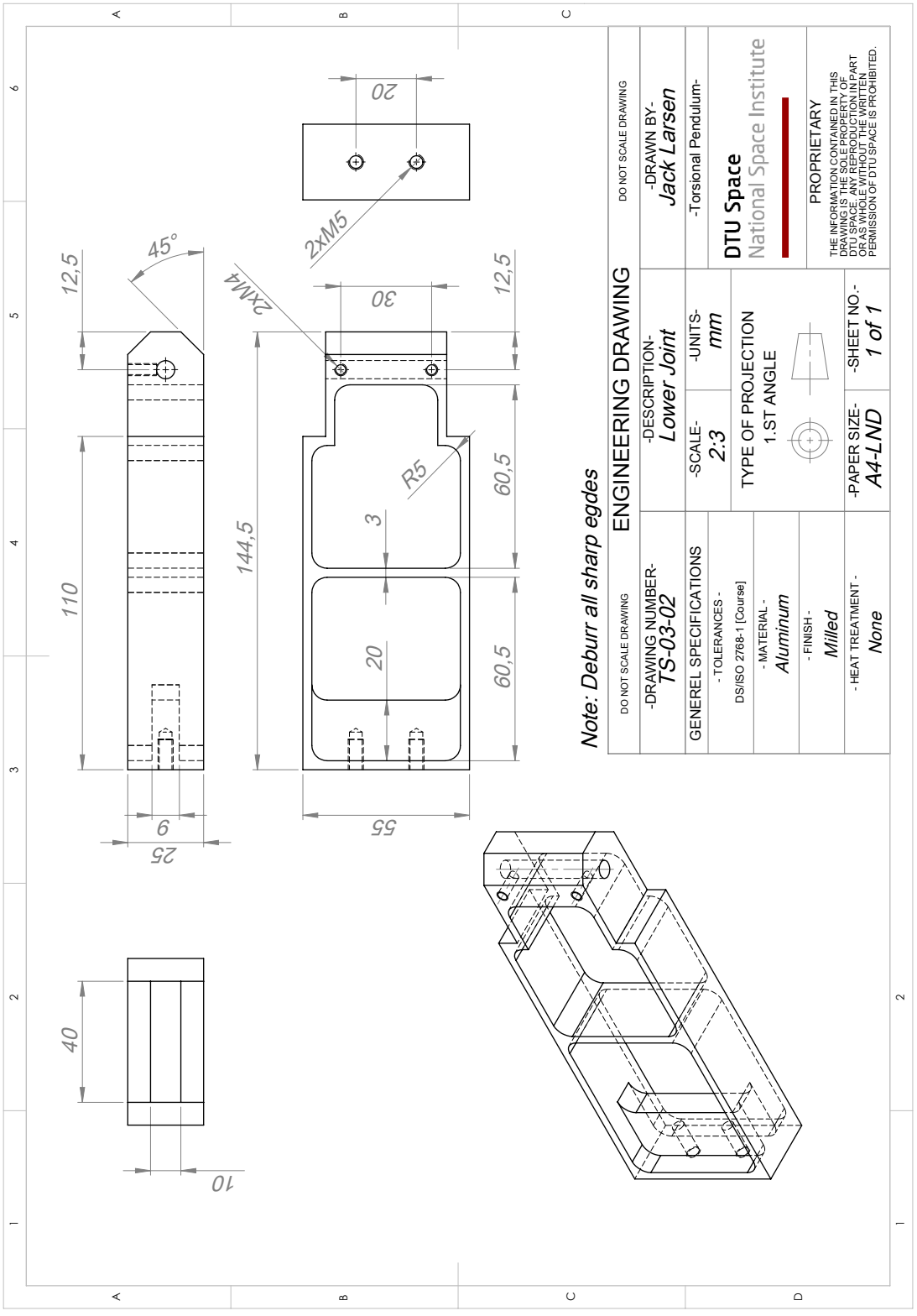

Figure D.13: Test Setup: Lower part of joint carrying the horizontal arm.

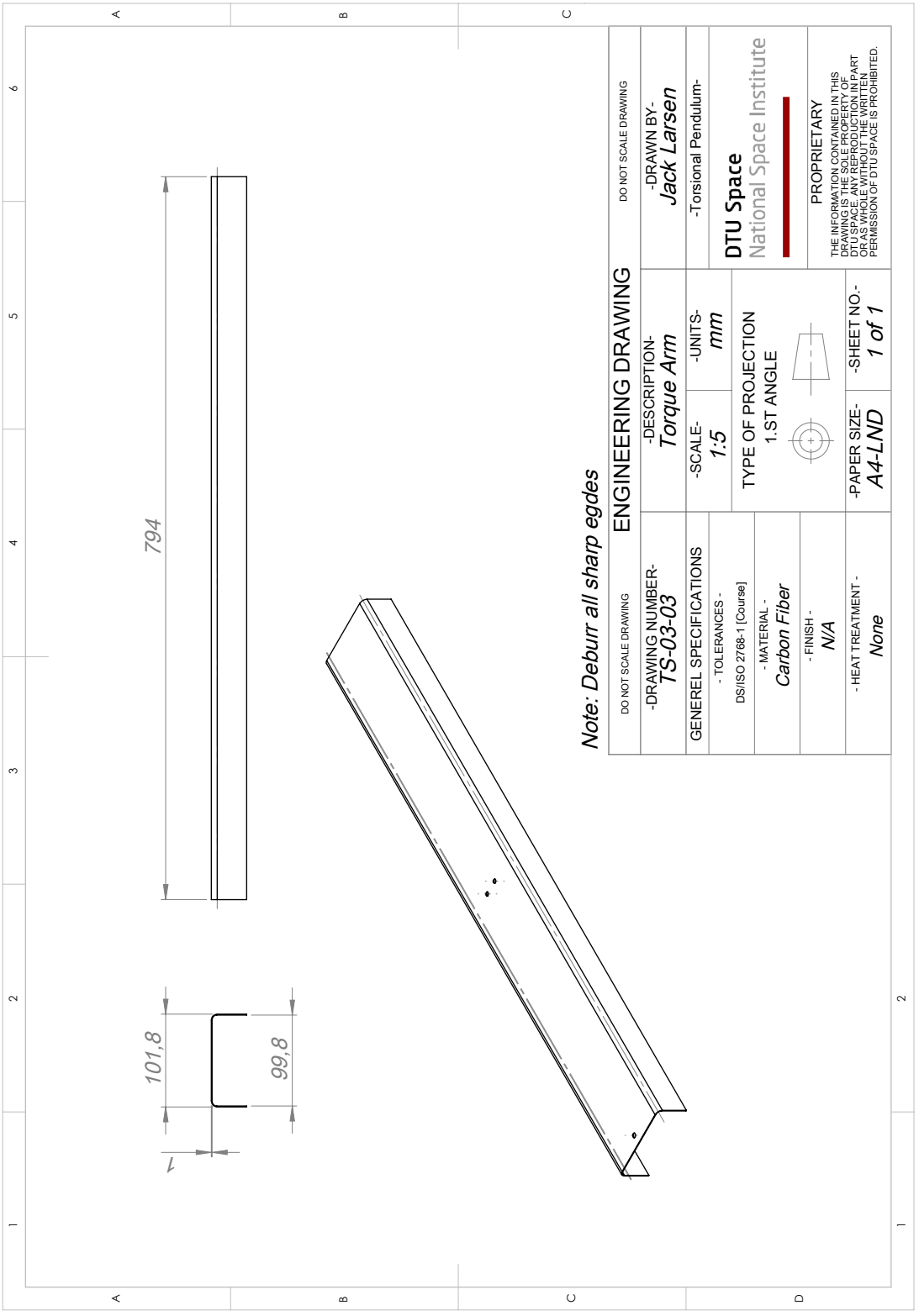

Figure D.14: Test Setup: Torque Arm

Test Setup: Horizontally oriented torque arm carrying the battery, receiver, power supply and thruster.